METASTABLE PYROXENES AND THEIR ROLE IN THE SUBDUCTION PROCESS

A DISSERTATION SUBMITTED TO THE GRADUATE DIVISION OF THE
UNIVERSITY OF HAWAIʻI AT MĀNOA IN PARTIAL FULFILLMENT
OF THE REQUIREMENTS FOR THE DEGREE OF

DOCTOR OF PHILOSOPHY

IN

GEOLOGY AND GEOPHYSICS

DECEMBER 2018

By

Yi Hu

Dissertation Committee:

Dr. Przemyslaw K. Dera, Chairperson
Dr. Bin Chen, Hawaii Institute of Geophysics and Planetology
Dr. Julia E. Hammer, Department of Geology and Geophysics
Dr. Eric B. Szarmes, Department of Physics
Dr. Craig R. Bina, Department of Earth and Planetary Sciences, Northwestern University

To my family

ACKNOWLEDGMENTS

I would like to express my sincere gratitude to my advisor Prof. Przemek Dera for his continuous support of my Ph.D study and research. I started my Ph.D without any experience in high pressure and X-ray experiments, Przemek guided me through all the experimental and data analysis details with great patience. He is an expert on X-ray diffraction and his immense knowledge helps me to overcome various difficulties in my research. He also allows me to explore freely the frontier of this field.

I would also like to thank all my committee members — Prof. Craig Bina for his insightful suggestions on slab dynamics which are of great help to my research, Prof. Bin Chen who helped me a lot in high pressure experiments, Prof. Julia Hammer who showed me the beauty of minerals, and Prof. Eric Szarmes for his wonderful optics class. I would like to thank Prof. Clint Conrad as well, who taught me a lot about geodynamics.

I want to send my thank to all my collaborators — Prof. Boris Kiefer, Dr. Kirill Zhuravlev, Dr. Anna Plonka and so on for their help in calculations and experiments.

I also gained a significant amount of help from my labmates, classmates and friends. I want to send my thank to Dr. Dongzhou Zhang, Dr. Jin Zhang, Dr. Jingui Xu for their help in experiments and insightful suggestions on data analysis. I want to thank my labmate and friend Xiaojing Lai who is a great roommate and labmate and is always willing to help me.

In the end, I want to give my thankfulness to my family and my friends who are always supporting me and encouraging me.

ABSTRACT

Pyroxene is an important group of minerals in the subducted slab and the upper mantle. In the upper mantle, where the temperature is high, pyroxene gradually dissolves into garnet and forms majoritic garnet at the base of the upper mantle and the transition zone. However, recent studies show that the pyroxene to garnet transition is very slow, especially in the cold subduction zones. Therefore, pyroxene is expected to be preserved metastable to the transition zone or even the top of the lower mantle in the cold subducted slabs. In this thesis, the high pressure behavior of two clinopyroxenes — hedenbergite and diopside are studied at high pressure conditions.

The compressional behavior of hedenbergite ($CaFeSi_2O_6$), end-member diopside and iron-bearing diopside are studied by single-crystal X-ray diffraction. The unit cell parameters and equation of state are reported and compared. At the upper mantle depths, eclogite with aluminous iron-bearing diopside is denser than eclogite with end-member diopside in the cold subducted slab conditions, and therefore provides larger slab pulling force. At the bottom of the transition zone and the top of the lower mantle, eclogite with aluminous iron-bearing diopside, though has higher density than that with end-member diopside, is still less dense than the surrounding mantle and could contribute to slab stagnation — a failure of the slab to descend into the lower mantle.

A new phase (γ-diopside) with Si in a rare five-fold coordination site is observed above 50 GPa. This result suggests that ^{V}Si may exist in the transition zone and the uppermost lower mantle in appreciable quantities and may have significant influences on buoyancy, wave velocity anomalies, deformation mechanisms, chemical reactivity of silicate rocks and seismicity within the slab. The γ-diopside is $\sim 6\%$ and $\sim 11\%$ lighter than $MgSiO_3$ akimotoite and $CaSiO_3$ + $MgSiO_3$ perovskite mixture, which would promote stagnation of the cold slab in the transition zone or the uppermost part of the lower mantle.

All studies suggests that metastable pyroxenes, even after phase transitions, are less dense than the surrounding mantle minerals in the transition zone or the top of the lower mantle, and can contribute to slab stagnation.

TABLE OF CONTENTS

LIST OF TABLES

LIST OF FIGURES

CHAPTER 1
INTRODUCTION

1.1 Subduction Zone

Subduction is a geological process that takes place at convergent boundaries of tectonic plates, where one plate thrusts beneath the other and is forced into the mantle. Oceanic plates, due to their high density always subduct; therefore, many subduction zones, such as the Japan Trench and the Kermadec-Tonga zone are located around the oceans. Subduction process is important because it causes and controls various dramatic geological phenomena and hazardous events to occur on the Earth's surface, such as volcano eruptions and earthquakes (figure 1.1). Subducted slabs also take part in the global scale mantle convection, which is the most import process that happens in the deep interior of the Earth.

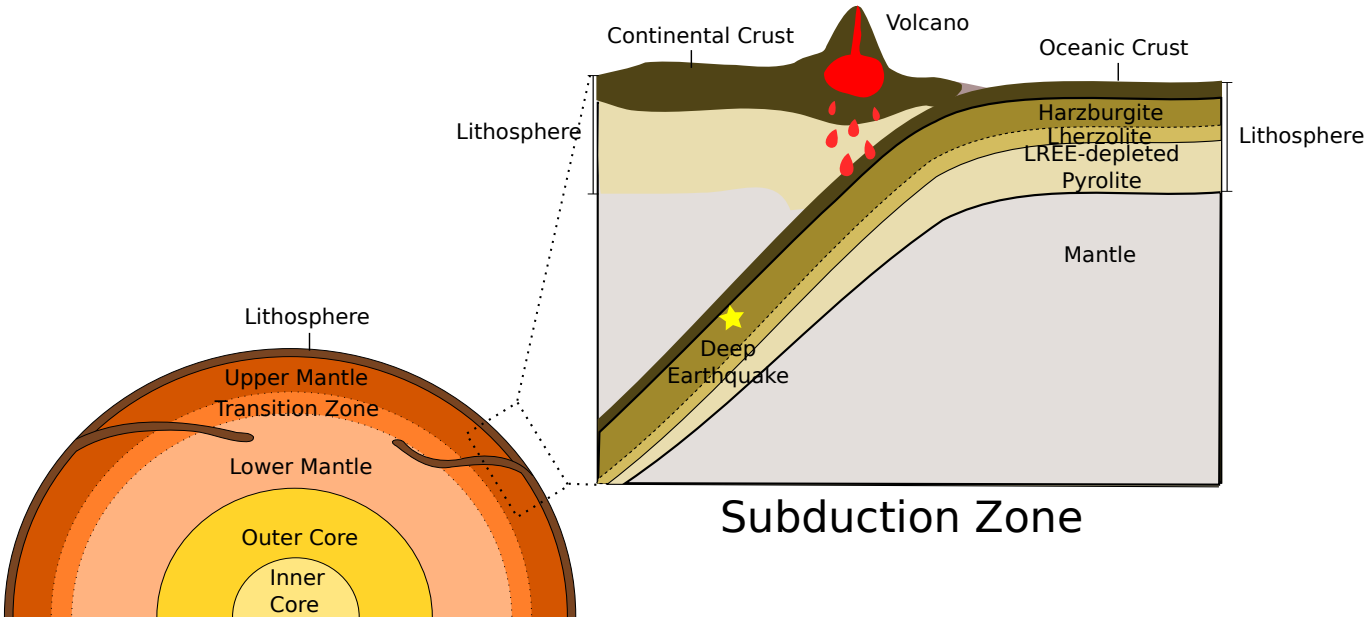

Figure 1.1: The layout of a typical subduction zone. Not drawn to scale.

There are many unsolved problems related to subduction zones. Which factors control slab stagnation at the transition zone is one such unanswered question. It has been observed that some slabs become flattened and stagnant between 400 and 1000 km and this phenomenon is believed to be affected by many factors such as mineralogy and petrology, density, rheological properties of the slab and the surrounding mantle [19]. Another mystery that is related to the subduction process is the triggering mechanism of the deep-focus earthquakes, which originate in the subducting slabs.

Shallow-focus earthquakes are the result of brittle fracture; however, this mechanism is unlikely to apply to deep-focus earthquakes, which originate at depths exceeding 300 km, due to the dominant plastic behavior of rocks at these greater depths. Many hypotheses have been proposed to explain the mechanism of deep-focus earthquakes, and one of them suggests involvement of crystalline mineral phases [20].

To obtain a better understanding of the subduction process and shed some light on the problems mentioned above, improved constrains on the structure and mineral composition of subducted slabs have to be established. Due to the limitations of direct sampling of mantle rocks, most of the knowledge of the slab structure and composition is obtained from geodynamic modeling by combining geophysical observations and information about properties and behavior of minerals at high pressure and high temperature conditions [21]. This thesis discusses the phases and physical properties of several important minerals in the subducted slab at high pressure conditions.

1.2 The Petrological Model of the Subducted Slab and the Mantle

Table 1.1: Chemical composition of subducted slabs. [a] Minor amounts of Cr_2O_3 in harzburgite (0.58%) and pyrolite (0.45%) were omitted in formulation of calculated mineral assemblages. [b] $FeO^* = FeO + MnO + NiO + Fe_2O_3$. This table is modified after [1].

	Average MORB [22]	Primitive MORB [23]	Harzburgite[a] [23]	Pyrolite[a] [23]
SiO_2	50.8	49.7	43.9	45.0
Al_2O_3	15.4	16.4	1.4	4.4
FeO^*	10.6	8.0	7.9	8.0
MgO	7.5	10.1	45.8	38.8
CaO	11.6	13.1	1.0	3.4
Na_2O	2.7	2.0	—	0.4
TiO_2	1.4	0.7	—	—
$\frac{100\ MgO}{(MgO+FeO^*)}$ [b]	55.8	69.2	91.2	89.6

The mineralogy of the subducted slabs plays an important role in the subduction process. The subducted slab is a layered structure consisting a mid-ocean ridge basaltic (MORB) crust, harzburgite, lherzolite and depleted pyrolite as shown in figure 1.2. The chemical composition of MORB, harzburgite and pyrolite are shown in table 1.1. The MORB layer has higher Al, Ca and Na content and lower Mg-to-Fe ratio than the underlying harzburgite and pyrolite [1]. At the surface, MORB is composed of amphibole, chlorite, albite and epidote [24]. The harzburgite and lherzolite layers are mainly composed of olivine and pyroxene. There are ∼78% olivine and 22% orthopyroxene in the harzburgite layer. The lherzolite layer is composed of ∼65% olivine and 35% pyroxene. In the depleted pyrolite layer, there is ∼57% olivine and 43% pyroxene, plus garnet as shown in figure 1.2.

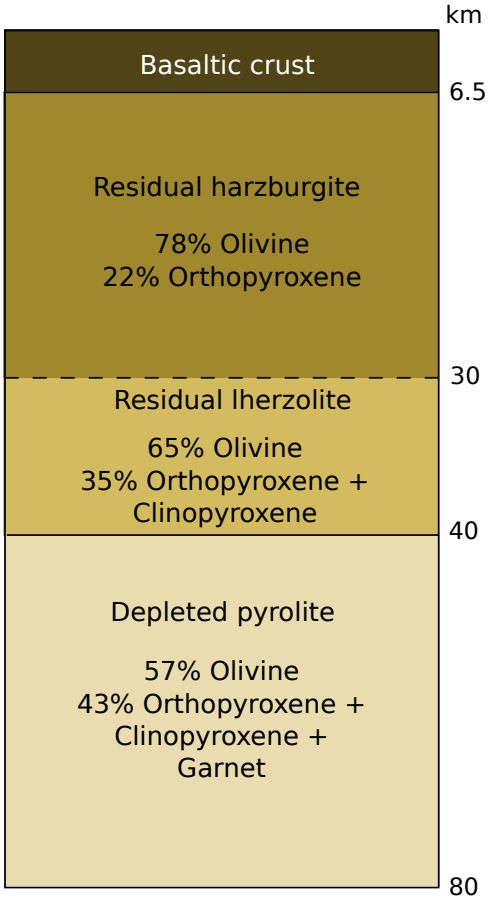

Figure 1.2: The mineral phases in a layered subducted slab. Not drawn to scale. This figure is modified after [1].

The phase transitions of minerals in the subducted slabs are still under debate. Considering only the stable phases, the minerals in the slab are expected to go through similar phase transitions as those in the normal mantle as shown in figure 1.3. The phase transitions of minerals in the normal mantle are well studied [25] and are discussed in detail below. The mantle is defined as the region between crust and the core and is devided into three layers — the upper mantle, the transition zone and the lower mantle as shown in figure 1.1. The upper mantle starts at the base of the crust around 7 to 35 km ($<$ 1 GPa, 1600 K) and ends at the 410 km discontinuity which corresponds to $\sim$13 GPa and 1700 K [26, 27]. At the base of the upper mantle, there is $\sim$ 55% olivine, 15% garnet and 30% clinopyroxene plus orthopyroxene [28, 27]. As depth increases, pyroxene gradually dissolves into garnet and forms majoritic garnet at the base of the upper mantle [25]. The olivine transforms to wadsleyite, which causes a discountinuity at 410 km that can be detected by seismic waves, and globally defines the lower boundary of the upper mantle [29]. Below the upper mantle is the transition zone which extends to the 660 km discountinuity ($\sim$ 24 GPa and 1800 K) [26, 27].

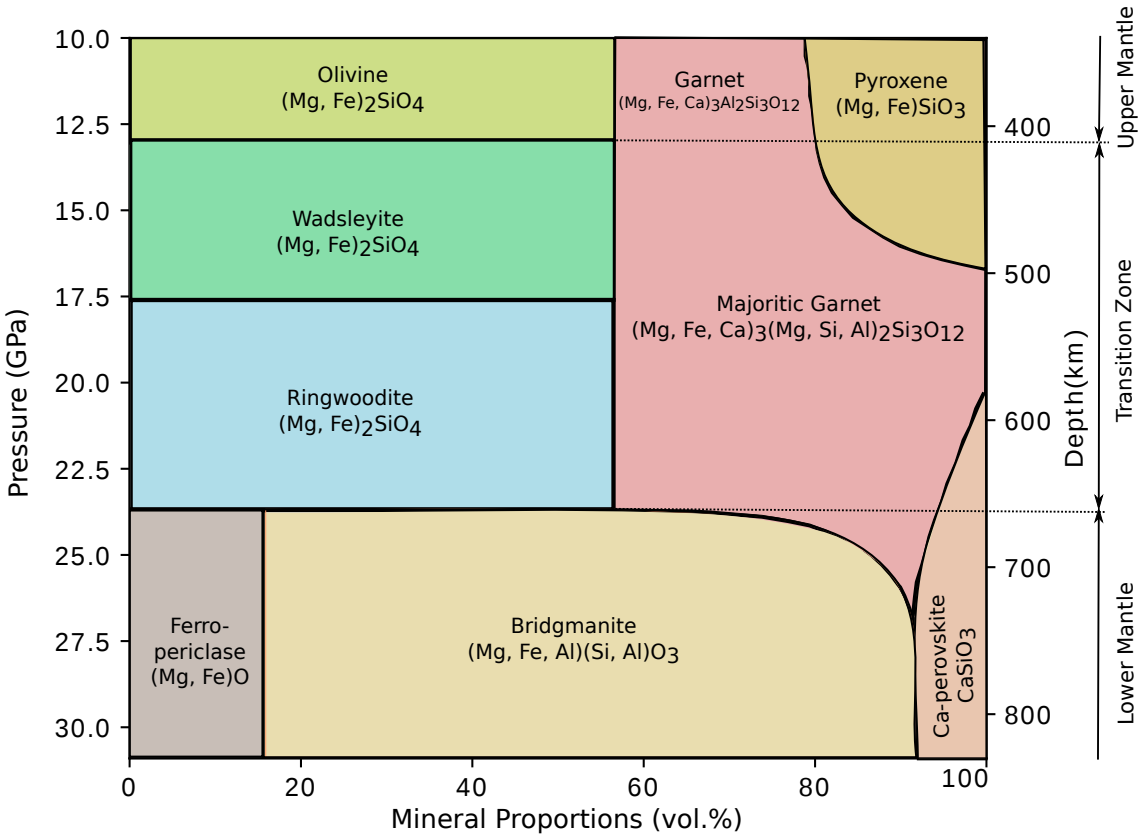

Figure 1.3: The mineral phases in the mantle. This figure is modified after [8].

In the transition zone, wadsleyite transforms to ringwoodite at ∼17 GPa and causes the 520 km discontinuity, which can be observed by seismic waves regionally [29]. In this region, pyroxene is almost fully dissoved into garnet and turns into marjoritic garnet [27]. Ringwoodite decomposes to ferropericlase and bridgmanite at 660 km depth and causes a global discountinuity, which defines the upper boundary of the lower mantle [28, 29]. In this region, majoritic garnet transforms to bridgmanite [27].

According to the stable phase diagram, similar phase transitions are expected in the subducted slab. As the crust subducts, at ∼2.5 GPa (70 km), MORB transform to eclogite, which contains ∼30% garnet and 70% pyroxene[1, 24, 30]. Eclogite is a dense rock and provides the driving force for the slab to subduct in the upper mantle [31]. Further, MORB transforms to garnetite, which is composed of majoritic garnet and stishovite, at the depth of the upper mantle and the transition zone [32]. Olivine in the subducted slabs should also go through the olivine-wadsleyite-ringwoodite transitions.

However, recent studies show that the transition from pyroxene to garnet is very slow [33, 34, 35, 36]. Especially at the conditions of the cold subducted slabs, such as the Tonga, where the

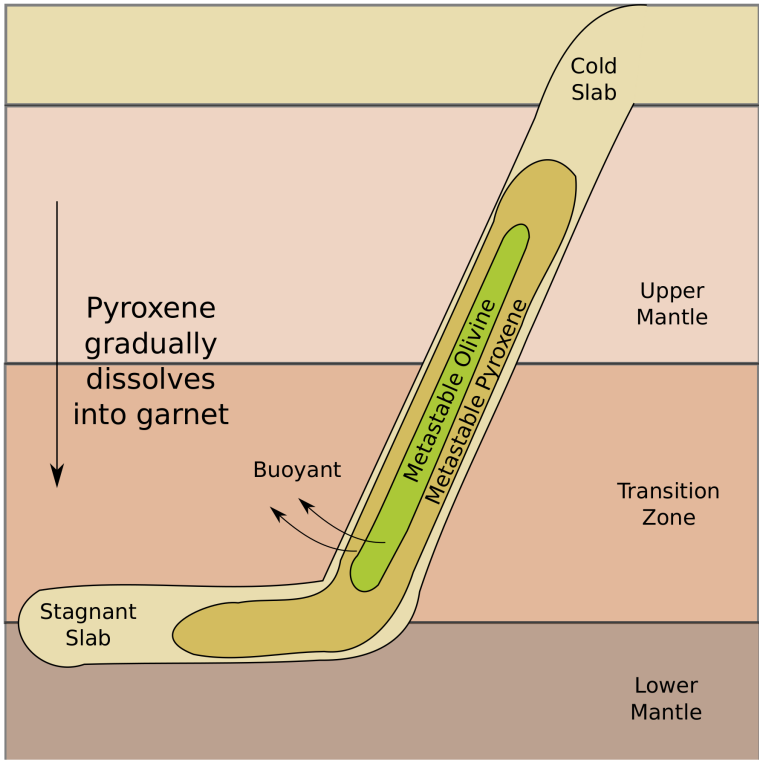

Figure 1.4: The regions of metastable minerals in the stagnant slab. This figure is modified after [9].

lowest temerature can be below 1300°K, or even as low as 800 °K, at the bottom of the lower mantle [37]. It takes about 10-15 Myr for the subducting slab to pass through the transition zone. According to the kinetic experimental results obtained at 1000°C and 18 GPa, only about 35% of the pyroxene has dissolved into garnet after 12.5 Myr. Therefore, it is unlikely that subducted oceanic crust can reach a state of thermodynamic equilibrium. At these conditions, it is possible that pyroxene can be preserved to the bottom of the transition zone and the top of the lower mantle as shown in figure 1.4 [33, 9]. The metastable pyroxenes are less dense than the surrounding mantle, even at cold conditions, and therefore cause the slab to be neutrally buoyant at the transition zone [33, 9, 37]. This conclusion agrees well with the observation that stagnant slabs are dominant in cold subduction zones [37].

The possible preservation of metastable pyroxenes to the transition zone or even the lower mantle and its metastable polymorphic phase transitions are believed to affect slab dynamics in three ways: (1) Pyroxene and its metastable high pressure polymorphs are less dense than garnet and presence of metastable pyroxene metastable in the slab can increase the slab buoyancy, causing slab stagnation at the transition zone (1.4) [36, 33, 9, 37]. (2) Phase transition in the slab may induce grain size reduction which could lead to weakening of the slab that lead to slab stagnation [38, 35].

(3) The heat released or absorbed during the phase transition affects the thermal environment of the slab which can shifts the phase transformation to different depths depending on the Clapeyron slope of the phase transition [39].
In this thesis, the high pressure behavior of pyroxene and its role in the subduction process are studied.

1.3 The Pyroxene Mineral Group

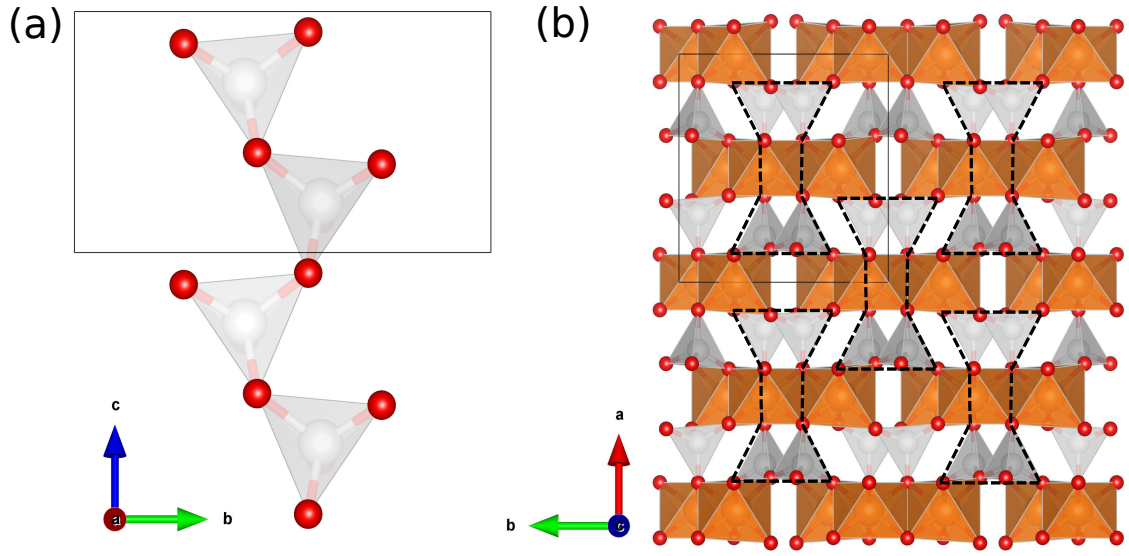

Figure 1.5: The crystal structure of pyroxene ($C2/c$ $MgSiO_3$). Red atom, oxygen; grey atom, silicon; orange atom, magnesium. (a) The Si-O chain along the c axis. (b) The pyroxene structure at the a-b plane.

The pyroxene structure, with the chemical formula of $M2M1T_2O_6$, belongs to the inosilicate family and consists of alternating layers of edge-sharing SiO_4 tetrahedral chains (figure1.5a) and layers of octahedrally coordinated cations (figure 1.5b). The SiO_4 tetrahedral chains with M1 sites in between can be simplistically represented by I-beams (figure 1.5b), and pyroxene structures can be viewed as stacking of I-beams separated by M2 sites. The ability of the tetrahedra along the silicate chains to rotate with respect to one another allows the structure to accommodate cations with different ionic radii and charges, leading to a wide range of possible compositions [40]. The octahedral layers contain two types of cation sites; the smaller M1 site with more regular coordination geometry, typically occupied by Mg^{2+} or Fe^{2+}, and the larger M2 site, which often features coordination numbers higher than 6. There are three main stacking polymorph types differing in symmetry — $C2/c$ or $P2_1/c$ for clino-pyroxene (cPx), $Pbca$ for ortho-pyroxene (oPx) and Pbcn for

Proto-pyroxene (pPx). Within each of these three main types, further symmetry distortions are possible by changing the silicate chain kinking angle and substitutional ordering of cations[40]. The most important pyroxenes/pyroxenoids include end-member compositions of $Mg_2Si_2O_6$ (enstatite, En), $Fe_2Si_2O_6$ (ferrosilite, Fs) and $Ca_2Si_2O_6$ (wollastonite, Wo) as shown in figure1.6. The compositions with Ca/(Mg, Fe) exceeding 1.00 crystallize in a pyroxene-related pyroxenoid structure, whereas the compositions belonging to the quadrilateral $CaMgSi_2O_6$ (diopside, Di), $CaFeSi_2O_6$ (hedenbergite, Hed) are proper pyroxenes. At ambient conditions, Ca content above Ca/(Mg, Fe) 0.05 favors the $C2/c$ cPx stacking arrangement, whereas the Ca-poor pyroxenes found on the surface typically crystallize in $Pbca$ orthopyroxene structure, though $P2_1/c$ is believed to be the stable phase of Ca-poor pyroxenes at ambient condition[40].

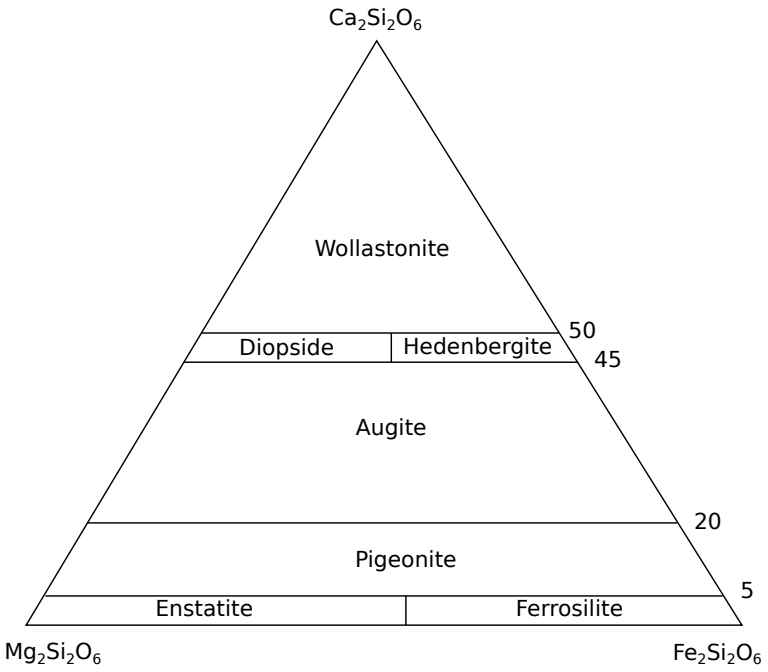

Figure 1.6: Ternary composition phase diagram with En-Fs-Hed-Di principal quadrilateral.

1.4 High-pressure Techniques

1.4.1 Diamond Anvil Cell

The interior of the Earth is under high-pressure (up to ∼360 GPa) and high-temperature (up to ∼ 6000 K) conditions [41]. To study the behavior of mateirals in the interior of the Earth, special devices are required to simulate the high-pressure and high-temperature conditions. Currently, there are three major approaches to generate high pressure. The first approach is the shock compression. This method generates a large-amplitute and supersonic compressional wave (shock wave) to

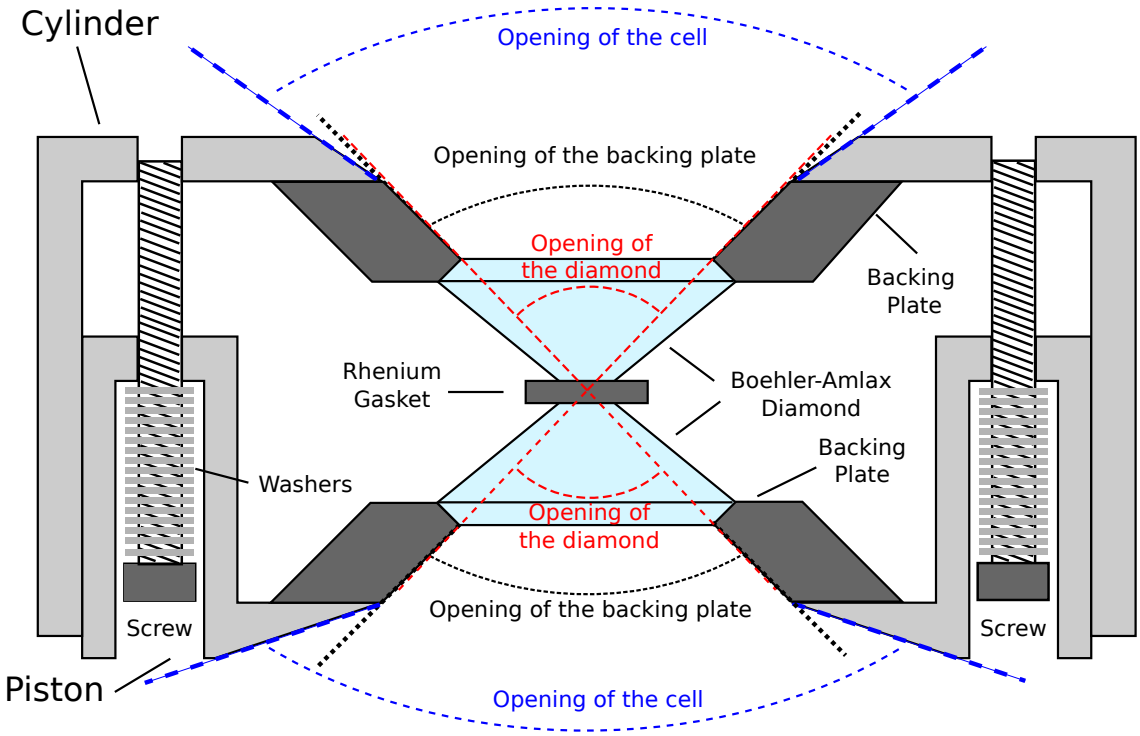

Figure 1.7: The diamond anvil cell.

compress samples to high pressure within a short period (nanosecond to microsecond). The shock wave can be generated by either accelerating projectiles and impact the target samples (e.g., [42]) or using high-power laser (e.g., [43]). This method can compress the samples to extremely high pressures ($\sim$ 1000 GPa) ([43, 44, 45, 46]). However, this method is limited by its short compression duration (nanosecond to microsecond). During such short compression time, huge amount of energy is ejected to the sample, raising the temperature of the sample. Such short time duration also makes many types of measurement that requires long exposure time difficult. Meanwhile, not enough time is given to the sample to dissipate the heat to reach thermal equilibrium with the environment. Shock experiments requires large and expensive devices that is not accessible to most people. Therefore, static compression methods, as discussed below, are more commonly used.

The second type of high pressure generation apparatus is the large volume press [47]. In this method, a $\sim$ 0.1 mm^3 size sample is placed in the center of a press, which hundreds to thousands tons of static force exerted to generate high pressure [47]. The size of samples used in this method is usually larger compared to other methods, so it is often used in sample synthesis. However, due to its large sample chamber size, the pressure that large volume press can reach is limited to $\sim$ 65 GPa with WC anvils [48].

The third device for high pressure generation is the diamond anvil cell [49]. This method, due

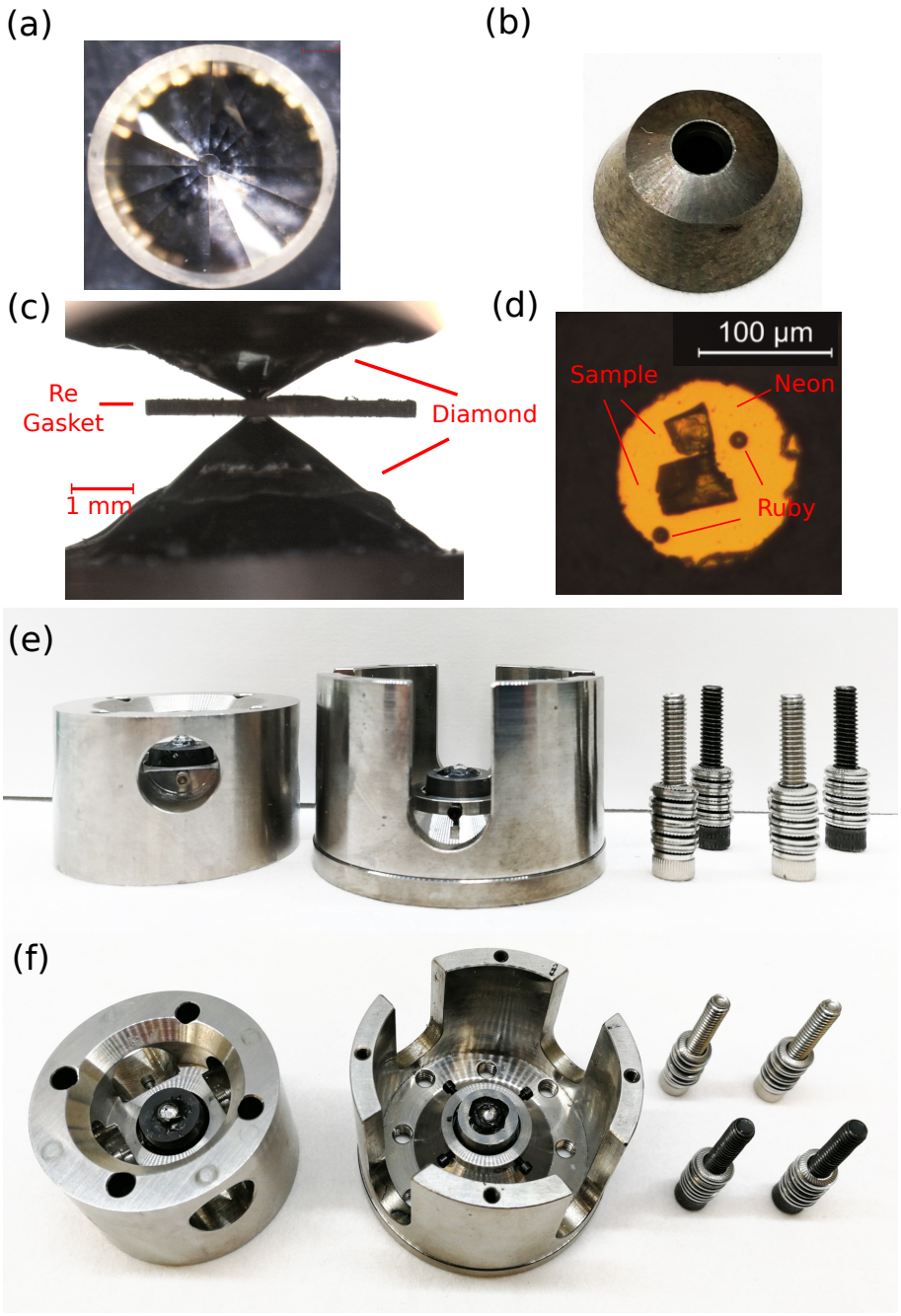

Figure 1.8: The diamond anvil cell and their components. (a) Diamond (diameter = 3.3 mm) with a cutlet diameter of 300 μm. (b) WC backing plate with a diameter of 3.3 mm for the inner hole. (c) The side view of a closed diamond anvil cell with a Re gasket. (d) Sample chamber viewed through the diamonds. (e) The side view of a diamond anvil cell. The length of the screws (cap not included) is 1 inch; (f) The top view of a diamond anvil cell.

to its many advantages, is used in this thesis and is described in detail below. The diamond anvil cell (DAC) is in principle a piston-cylinder or a plate-opposing device, which uses diamonds, one of the hardest material on the Earth, as anvils to generate high pressure. There are many different types of diamond anvil cell, but the basic components and the principles are similar. Figure 1.7 and figure 1.8(e)(f) show the piston-cylinder type diamond anvil cell (BX-90). Two diamonds with tips cut flat (called the "culet") (figure 1.8(a)) are mounted on backing plates (figure 1.8(b)) and are placed on each side of the piston-cylinder device. The backing plates are usually made of hard materials such as tungsten carbide (WC) and cubic boron-nitride (cBN). Between the two diamonds is a metal gasket (usually made of Rhenium) with a hole in the center, within which samples are placed. Figure 1.8(c) shows a closed diamond anvil cell and figure 1.8(d) shows the sample chamber looking through the diamond. Pressure $P = F/A$ is the force (F) devided by the contacting area (A). To increase pressure, either the force should be increased or the contacting area should be decreased. The screws with washers in the piston-cylinder device are used to increase the force. The diamond tips are cut to ~ 60 — 500 μm to decrease the contacting area. To keep a quasi-hydrostatic environment, gas pressure-transmitting medium such as neon or helium is usually loaded into the sample chamber [50].

Diamond anvil cell has many advantages comparing to shock compression and large volume press: (1) Diamond is one of the hardest materials on the Earth and can hold several hundred GPa pressures [51]. (2) Diamond anvil cell generates static and (quasi-)hydrostatic pressure. (3) Diamond is trasparent to a wide range of electromagenic radiations including X-ray, which allows the application of various techniques, such as Raman spectroscopy and X-ray diffraction, to the samples in situ. In situ measurements are important because many high-pressure and high-temperature phases cannot be preserved to ambient conditions. (4) Diamond anvil cell is a small device and can be easily transported to different locations, which faciliates the usages of synchrotron radiation sources. However, the samples used in the diamond anvil cell are very small (about micrometers in size), which makes some measurements difficult. Therefore, strong X-ray radiation sources, such as synchrotron radiation sources, are used (discussed in the next section).

BX-90 cell is the type of diamond anvil cell that used mostly in this thesis as shown in figure 1.7 and figure 1.8(e)(f) [52]. This cell consists a piston and a cylinder that matches exactly with each other, providing high mechanical stability for the diamonds. This cell is characterized by its wide symmetrical axial opening of 90 °, which is crucial for single crystal X-ray diffraction experiments. Bohler-Almax diamonds are usually used together with this type of cell to make the maximum usage of its wide opening angle. The Bohler-Amlax diamond anvil (BA diamond) is a specially designed conical type diamond used to achieve big opening (figure 1.7 and figure 1.8(a)) [53]. The aperture of diamonds is determined by the height to base diameter ratio as shown in figure 1.7. The BA diamond has a circular bottom cone which increases the diamter, and therefore increases the aperture. A typical BA diamond achieves an opening of 70° — 75° . In order to mount the

diamond on cell, a backing plate with a matching cone should be used [53] (figure 1.7 and figure 1.8(b)).

The diamond anvil cell consists of two opposite anvils and therefore provides higher stress along the loading direction. However, in most high-pressure experiments, (quasi-)hydrostatic environment is desired. In order to achieve (quasi-)hyrdrostatic environment, pressure-transmitting medium is always used. Different pressure-transmitting medium is used for different purpose. Light noble gas, such as He and Ne, is one of the most commonly used pressure-transmitting medium, thanks to the gas-loading system at the beamline [50]. There are many advantages of using noble gas as the pressure-transmitting medium: (1) It is chemically inert and therefore does not react with most samples. (2) Inert gas crystallizes at high pressure and is soft, even after crystallization [54], providing (quasi-)hydrostatic environment. (3) Inert gas is optically transparent. (4) Light noble gas is a weak X-ray scatterer.

Neon and helium are two types of most commonly used noble gas pressure-transmitting medium. Neon crystalizes at 4.8 GPa at ambient temperature [55]. Experiments show that neon becomes nonhydrostatic at $\sim$ 15 GPa. Helium provides better hydrostatic environment than neon and other pressure-transmittin medium [55]. However, helium diffuses easiliy into diamonds, making the diamonds more vulnerable to cracks.

1.4.2 Pressure Determination

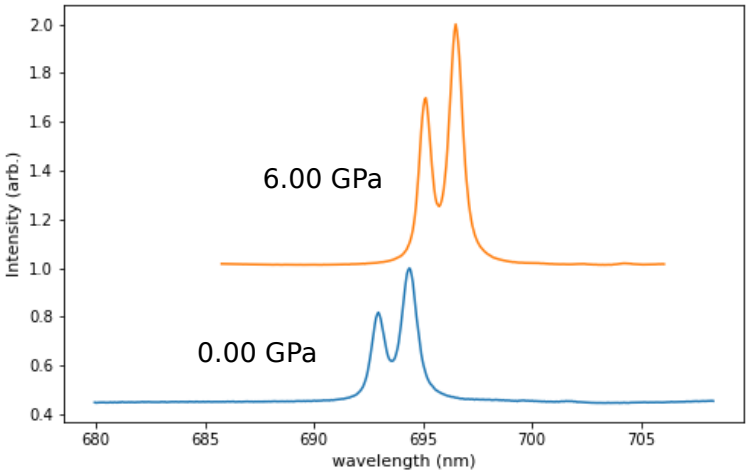

Figure 1.9: The ruby spectrum at 0.00 and 6.00 GPa.

Sample chamber of the diamond anvil cell is very small (few hundred μm in diameter, few μm in thickness) as shown in figure 1.8(d). Therefore, mechanical pressure gauges cannot be used to determine pressure in DAC. Instead, the pressure inside the sample chamber is measured by optical spectroscopy or X-ray diffraction methods.

Ruby fluorescence method is one common optical spectroscopy method to determine the pressure inside the sample chamber [49]. Ruby is a pink to blood-red colored gemstone-quality variety of corundum (α-Al_2O_3). Corumdum is colorless, and the red color of ruby is from partial substitution of Cr^{3+} for Al^3+ at the octahedral site in the structure. Cr^{3+} is a transition metal ion and causes the fluorescence phenomenon of the ruby crystal. After absorption of light, the d-electrons of Cr are excited from the ground $^4A_2$ state to the $^4T_1$ state, which then decays into an excited ^2E state. The high pressure experiments make use of the emission photon related to the ^2E to $^4A_2$ transition. This transition is dominated by two sharp bands located at $\sim$ 692.8 nm (R2) and 694.2 nm (R1) at ambient condition [56, 57]. The shift of ruby fluorescence peak R1 with pressure is well-studied [58, 59] and is expressed by the following equation:

$$P = A/B[1 + (\delta\lambda/\lambda_0)^B] - 1 \tag{1.1}$$

Mao et al. gives A = 19.04 Mbar and B = 7.665 [58]. Figure 1.9 shows the fluorescence spectrum of ruby at ambient condition and high pressure. The fluorescence peaks at high pressure shift to higher wavelength compared to that at ambient condition.

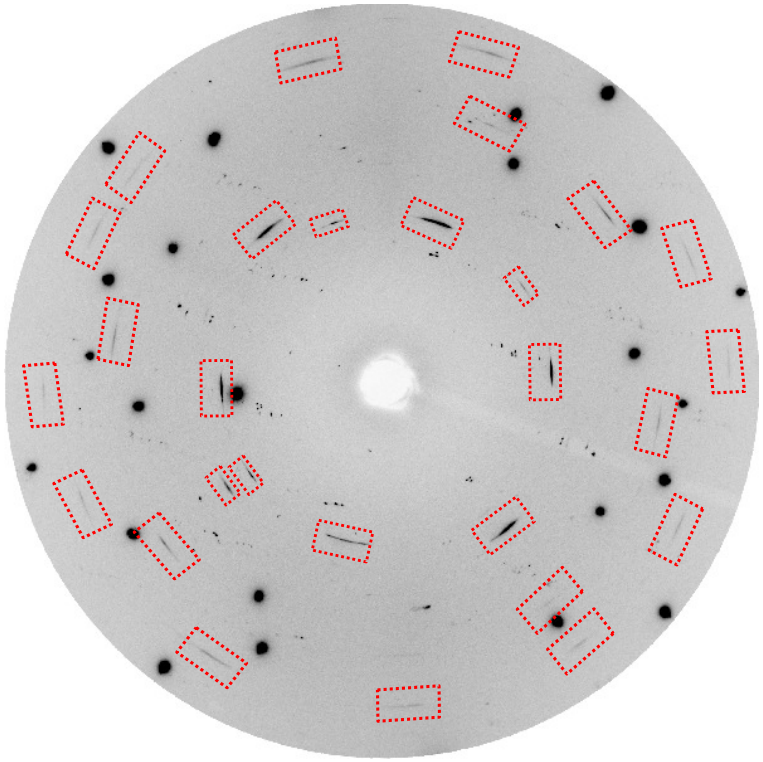

Figure 1.10: The diffraction peaks of neon (inside the red boxes) at 33.8(3) GPa.

At high pressure, ruby spectrum becomes broad, which makes the pressure determination dif-

ficult. Besides ruby fluorescence, well-defined equation of state of pressure medium (e.g., Neon) or pressurecalibration samples (e.g., Pt and Au) can also be used to determine pressure inside the sample chamber. Neon transforms to a face-centered cubic crystal at 4.8 GPa and 298 K [55], and the diffraction of neon crystal can be collected during X-ray diffraction measurements as shown in figure 1.10. In DAC, neon usually first crysalizes in single-crystal form and then becomes more and more powder-like. The equation of state (EoS) of neon has been well-studied to 208 GPa [60], and is described by Mie-Grunesen-Debye formalism.

1.5 X-ray Diffraction

1.5.1 The Physics of X-ray Diffraction

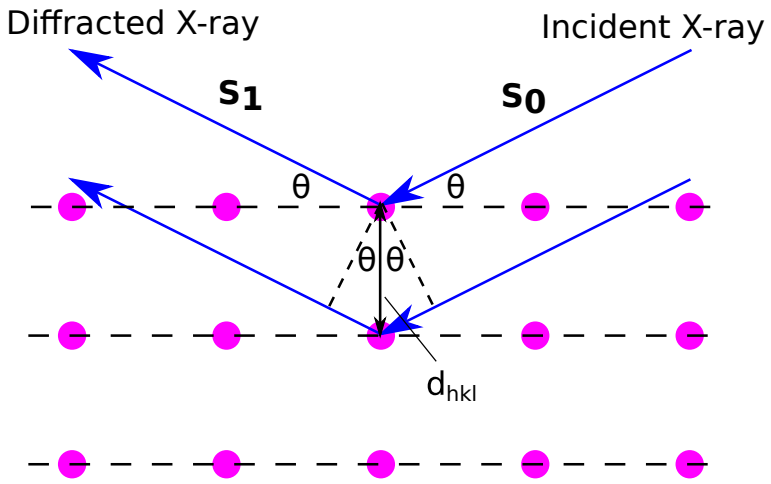

Figure 1.11: Bragg's law. The magenta dots represent unit cells in a crystal.

X-ray diffraction is a powerful method for obtaining structural information of crystals. X-rays are electromagnetic radiations, like visible light, but of much shorter wavelength. The wavelength of X-rays is between that of ultraviolet light and gamma rays, and is $\sim$ between 0.01 to 10 nm. The diffraction of X-rays by matter results from the combination of two different process: (1) scattering by the individual atoms with several electrons, and (2) interference between the waves scattered by each atom [61]. The diffraction pattern is related to the type of atoms inside the matter and also the spatial arrangement of the atoms. By interpreting the resultant diffraction pattern, the structure of the matter can be obtained.

The interference between unit cells in the crystal determines the positions of diffraction peaks, and is described by the famous Bragg's law [61]

$$n\lambda = 2d_{hkl}sin(\theta_{hkl}) \tag{1.2}$$

where λ is the wavelength of the incoming beam, n is an integer number, d_{hkl} is the spacing between hkl planes and θ_{hkl} is the diffraction angle associated with a specific hkl as illustrated in figure 1.11. This equation shows the conditions when a diffraction peak can be observed. The difference between the incident and the diffracted X-ray vector ($\mathbf{S_1} - \mathbf{S_0}$) is $2d_{hkl}sin(\theta_{hkl})$, and the diffraction condition satisfies when $\mathbf{S_1} - \mathbf{S_0}$ equals to $n\lambda$. From this equation, two important conclusions for experiment design can be drawn: (1) For each d_{hkl}, the diffraction peaks (Bragg peaks) can only be observed at certain angles (Bragg angles). (2) If the position of the Bragg peaks are known, the unit cell parameters can be solved from the d-spacings (d_{hkl}).

The intensity of the Bragg peaks also convey important information. The intensity I_{obs} of the diffraction peak is propotional to square of the structure factor $F(\mathbf{r}^*_{hkl})$ of the unit cell, which is described by

$$F(\mathbf{r}^*_{hkl}) = \sum_{j=1}^{N} f_j(\frac{1}{2d_{hkl}})exp[2\pi i(\mathbf{r}^*_{hkl}\cdot\mathbf{r}_{xyz})] \tag{1.3}$$

where $\mathbf{r}^*$=$h\cdot\mathbf{a}^* + k\cdot\mathbf{b}^* + l\cdot\mathbf{c}^*$ is the vector in the reciprocal space, $\mathbf{r}$=$x\cdot\mathbf{a} + y\cdot\mathbf{b} + z\cdot\mathbf{c}$ is the vector of an atom in the real space. N is the number of atoms in the unit cell, $f_i(\frac{1}{2d_{hkl}})$ is the atomic scattering factor of atom i at $d_{hkl} = \frac{1}{|\mathbf{r}^*_{hkl}|}$ [61, 62]. With this equation, the atomic positions can be solved from peak intensitites.

1.5.2 Single-crystal X-ray Diffraction

In general, based on the type of sample, there are two types of X-ray diffraction (XRD) techniques — powder XRD and single-crystal XRD. As can be infered from the name, powder X-ray diffraction uses powder crystalline samples. Crystals have different orientations in powder samples, which produces ring-like diffraction pattern, instead of spotty patterns as observed in single crystal X-ray diffration experiments. Besides, a new type of X-ray diffraction technique — multi-grain X-ray diffraction, which aims to fill the gap between powder and single-crystal XRD is playing an important role in high pressure research [63].

Powder XRD is one of the most widely used characterization technique in high pressure research. Compared with single-crystal XRD, it has many advantages: (1) The measurement time is shorter. (2) It is easier to set up. (3) It is easier for quick identification of known phases. (4) It does not require high quality single-crystal samples, which can be hard especially after some treatment such as laser heating. (5) With the convenience list above, it can be used to obtain important information such as unit cell parameters. However, powder XRD has many limitations. The peaks in powder diffraction are often broad and overlapped, which makes it difficult for indexing of low-symmetric structures, solving atomic positions and solving new crystal structures.

Thanks to the development of advanced synchrotron infrastructures [50], large aperture diamond anvil cell techniques [53], and data processing softwares [64] for high pressure research, single-crystal XRD becomes routine in high pressure research. The development of single-crystal XRD

at high pressure makes the determination of unknown crystal structures possible at high pressure [65, 66, 12]. Single-crystal diffraction is the main technique used in this thesis. The physics and the procedures of single-crystal diffraction is discussed below.

In general, data processing of single-crystal XRD can be divided into the following steps:

(1) Harvesting Bragg peaks;

(2) Indexing of the Bragg peaks;

(3) Solving the cystal structure;

(4) Refining the crystal structure.

Firstly, The Bragg peaks are extracted from 2D images collected different angles using spot detecting algorithms and fit with Gaussian or pseudo-Voigt functions [64]. The positions of the peaks in 3D space are used to determine the unit cell parameters (step 2). The intensities, together with the indexing results, are used for solving (step 3) and refining (step 4) the position of each atom in the unit cell. If the structure is known, step 3 can be skipped. With the peak positions known, the unit cell parameters can be determined by searching for lattice in the reciprocal space. The orientation of crystals and the hkl-index of each peak can also be obtained [67].

One big advantage of single-crystal XRD over powder XRD is the ability to solve crystal structure, which, however, is not trivial because of the famous phase problem. As discussed above, the observed intensity I_{obs} of a given diffraction peak is proportional to $|F(\mathbf{r}^*_{hkl})|^2$. However, the X-ray detectors can only measure the amplitude but not the phase of the X-ray waves. Therefore, the phase information which is crucial for structure determination is missing in the experiments. To overcome the phase problem, several methods such as probabilistic methods (e.g. direct methods [68]) and Fourier methods (e.g. Patterson methods [69]), are used.

After the structure is solved, refinement should be done to obtain a more precise structure. The goal of structural refinement is to minimize the difference between $|F_{obs}|^2$ and $|F_{calc}|^2$, where $|F_{obs}|^2$ is converted from I_{obs} obtained from experiments and $|F_{calc}|^2$ is calculated from the trial model. Below are three commonly used metrics to determine the quality of structural refinement:

$$R1 = \frac{\sum ||F_{obs}| - |F_{calc}||}{\sum |F_{obs}|} \tag{1.4}$$

$$wR2 = [\frac{\sum w(|F_{obs}|^2 - |F_{calc}|^2)^2}{\sum w(|F_{obs}|^2)^2}]^{1/2} \tag{1.5}$$

$$GooF = [\frac{\sum w(|F_{obs}|^2 - |F_{calc}|^2)^2}{N_R - N_P}]^{1/2} \tag{1.6}$$

In these equations, $|F_{obs}|$ and $|F_{calc}|$ are observed and calculated structural factors. w is the weight for each peak used in the fitting. N_R is the number of symmetrically independent diffraction peaks used in the fitting and N_P is the number of parameters refined. Usually, for a good refinement, $R1$ is below 10%, $wR2$ is below 20% and $GooF$ is near but slightly greater than 1.0 [70].

1.5.3 The X-ray Diffraction at the Synchrotron

High pressure single-crystal XRD is more difficult than ambient condition XRD, mainly due to the following reasons: (1) The aperture of the diamond anvil cell limits the reciprocal space that can be probed by experiments; (2) Samples are placed between two diamonds which absorb X-rays; (3) There is a metal gasket surrounding the sample, which could contribute undesired signals. To solve these problems, synchrotron radiations are often used in high pressure XRD research.
Synchrotron radiations are generated by accelerated electrons and has the following advantages over a conventional X-ray tube: (1) It is more than a billion times brighter; (2) It can be focused to nanometer size; (3) It provides broader spectrum and higher energy. The single-crystal XRD experiments in this thesis have been performed at synchrotron radiation sources, such as the Advanced Photon Source at Argonne National Laboratory. The experimental setup in synchrotron radiation sources is discussed below. In a synchrotron radiation source, electrons are generated by a hot electron gun.

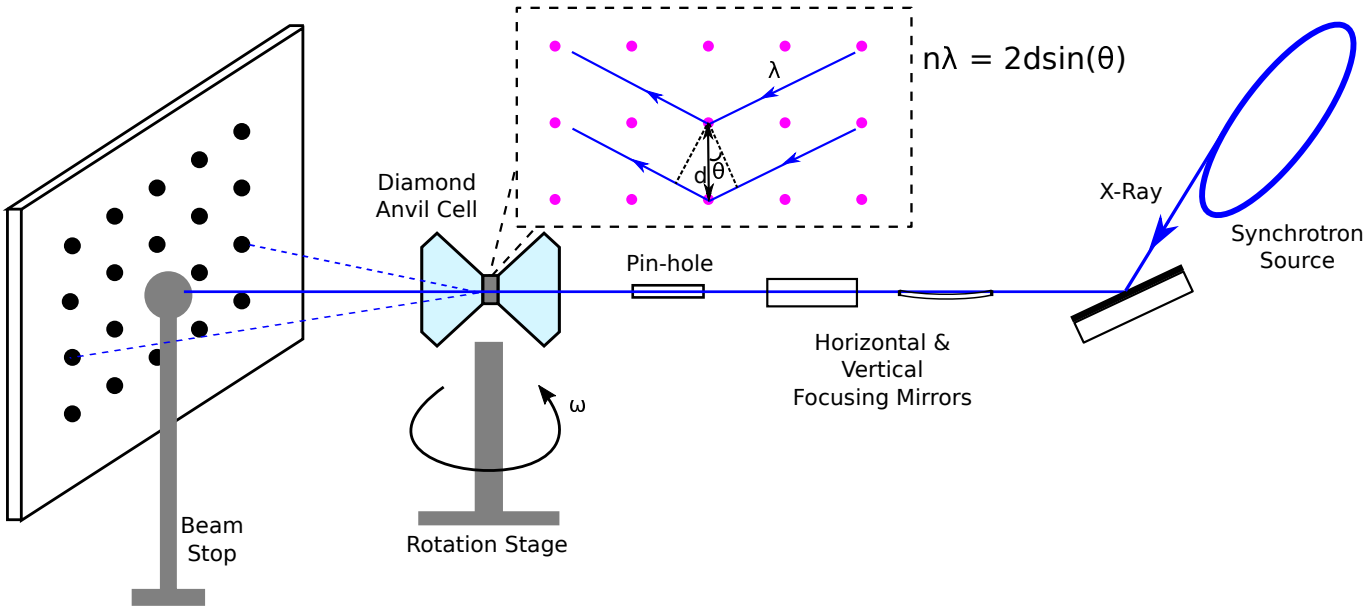

Figure 1.12: The experimental setup of 13IDD at the Advanced Photon Source.

The electrons travel through a linear accelerator and then a circular booster ring to get accelerated. After that, the electrons are ejected to the storage ring, where they go through a series of bending magnets and undulators. In this process, the traveling directions of electrons change and result in radiation of X-rays. The radiated X-rays are then directed to different experimental hutches. Different experimental hutches have different techniques and therefore have different X-ray optics to make advantage of different properties of the X-rays. For monochromatic X-ray diffraction experiments, the X-rays are usually directed through a monochromator and two focusing mirrors as shown in figure 1.12. The sample, diamond anvil cell, is placed on a rotation stage, the rotation

center of which is alligned with the X-ray beam. A charge-coupled device (CCD) detector is placed at the downstream position to collect diffraction peaks.

1.6 Scope of the thesis

This thesis studies the high-pressure behavior, including the equation of state and phase transitions, of clinopyroxene. The main technique used in this thesis is synchrotron single-crystal X-ray diffraction.

In chapter 2, the high pressure equation of state of the Fe-, Ca- rich clinopyroxene, hedenbergite ($CaFeSi_2O_6$), was studied to $\sim$ 33 GPa by single-crystal X-ray diffraction and Raman spectroscopy. The unit cell parameters and equation of state of this mineral is reported. The compression mechanism, the structural distortion and the Raman vibrational modes are also studied.

The high pressure behavior of diopside is studied in chapter 3 and chapter 4. Chapter 3 focuses on the high pressure equation of state of diopside. The equation of state of an end-member and an aluminous iron-bearing diopside ($CaFeSi_2O_6$) was studied to 50 GPa by single-crystal X-ray diffraction and density functional theories. The equation of state of both samples are studied and compared with other clinopyroxenes. The effect of Al^{3+} and Fe^{2+} on volume and bulk modulus are examined in clinopyroxene. The role of alumious iron-bearig diopside in the slab subduction and stagnation process is studied.

Chapter 4 focuses on phase transitions of diopside at high pressure. An new phase with rare penta-coordinated Si is observed. This observation suggests a possibility that this phase be preserved to the cold subducted slab. The effect of five-coordinated Si on chemical reactivity, elastic and plastic deformation, density of the subducted slab and its buoyancy relative to the surrounding mantle is studied.

CHAPTER 2
COMPRESSIONAL BEHAVIOR OF HEDENBERGITE UP TO 33 GPA

This chapter has been published as Hu, Y., Dera, P., and Zhuravlev, K. (2015). Single-crystal diffraction and Raman spectroscopy of hedenbergite up to 33 GPa. Physics and Chemistry of Minerals, 42(7), 595-608.

2.1 Abstract

Pyroxenes are important minerals in Earth's upper mantle and subducting plate. Here, we report results of high-pressure single-crystal X-ray diffraction and Raman spectroscopy experiments conducted on natural Ca, Fe pyroxene hedenbergite up to $\sim$ 33 GPa in diamond anvil cell. Unit cell parameters a, b, c, β, V, as well as bond lengths of hedenbergite are reported within the studied pressure range. Cell parameters exhibit continuous decrease on compression. Axial compressibilities of a, b and c are calculated to be 1.7(2), 4.9(5), 2.13(9) $\times$ 10^{-3} GPa^{-1}, respectively. Bulk modulus and its pressure derivative are determined to be 131(4) GPa and 3.8(3). Compression mechanism is dominated by polyhedral and bond compression trends typical of clinopyroxenes. In general, shorter bonds show lower compressibility and SiO_4, the smallest polyhedra, show the lowest compressibility. Angle and elongation distortions are reported for the three types of polyhedra at high pressure. 11 vibrational modes are observed with Raman spectroscopy up to $\sim$ 33 GPa. All observed, mode frequencies increase as pressure increases.

2.2 Introduction

Pyroxenes are important minerals in the deep Earth. In the bulk mantle, according to pyrolitic compositional model, the top upper mantle is composed of $\sim$ 65% olivine, $\sim$ 20% pyroxene and 15% garnet by volume [25, 71]. As pressure and temperature increase, pyroxenes gradually dissolve into garnet and form majorite garnet at the base of the upper mantle [72]. Pyroxenes are also abundant in subducting slabs. The oceanic lithosphere constitutes of basaltic crust (fine grained basalt and coarse grained gabbro), harzburgite, lherzolite and light-rare-earth-element (LREE)-depleted pyrolite. There are $\sim$ 22% and $\sim$ 35% pyroxenes in harzburgite and lherzolite, respectivly [1]. As the slab subducts into mantle, the top basaltic crustal layer undergoes eclogitic metamorphism during which plagioclase and some of the clinopyroxenes are consumed to produce grnet [1]. However, recent high pressure studies show that the dissolution of pyroxene into garnet is kinetically suppressed at temperatures below geotherm (<1000°C) thus they may be preserved to much higher pressure in the cool subduct slab [36, 33, 34]. Recently, many anomalous seismic velocity structures

have been observed by different seismic methods and are interpreted as metastable olivine wedge in cold suducting slabs [73, 74, 75]. It is possible that metastable pyroxenes exist in the cold slabs and even in broader ranges than metastable olivine, due to the higher temperatures defining their etastabilty limits [9].

Pyroxenes, with a general formula M2M1(Si, Al)$_2$O$_6$, belong to the inosilicate family, with crystal structures consisting of alternating layers of tetrahedral chains and layers of octahedrally coordinated cations. The ability of the tetrahedra along the silicate chains to rotate with respect to one another allows the structure to accommodate cations with different ionic radii and charges, leading to a wide range of possible compositions [40]. Recent single-crystal X-ray diffraction studies on pyroxenes (enstatite, diopside, ferrosillite) reported a number of new high-pressure phases under ambient temperature [76, 65, 66]. Hedenbergite is an important Ca, Fe end-member of clinopyroxenes family, and constraining its behavior and physical properties can be useful for modeling the behavior of clinopyroxenes solid solutions. Hedenbergite can be found in chondries [77] and skarn, a calcium-bearingrock [78]. Hedenbergite has been the subject of several high pressure studies. Its structure was determined up to $\sim$ 10 GPa by single-crystal diffraction and no discontinuous behavior was observed [3]. On the other hand, high-pressure nuclear forward scattering (synchrotron Mössbauer) studies up to 68 GPa reported discontinuities at 53 GPa ad 68 GPa [3, 79]. High temperature and high pressure phase transformation of hedenbergite were studied up to 40 GPa and $\sim$ 1200°C and decomposition to multiple phases was also observed [80, 81].

Single crystal diffraction is a powerful tool for resolving variations in the crystal structure. The bond length changes inside the crystal can be useful for predicting crystal behavior at high pressure and calculating element partitioning, as well as thermodynamic properties [82, 83, 84, 85]. Here, we determined the compressibility, structure and vibrational properties of natural hedenbergite by synchrotron single-crystal X-ray diffraction and Raman spectroscopy up to $\sim$33 GPa in diamond anvil cell. Compressibilities and pressure evolution of bond lengths and polyhedral distortion are determined and discussed.

2.3 Methods

In this study, we used a sample of natural hedenbergite from the University of Arizona RRUFF collection #R070236, with composition $Ca_{1.00}(Fe_{0.67}Mn_{0.16}Mg_{0.17})Si_2O_6$, determined by means of electron microprobe analysis. The ambient unit cell parameters, determined by single-crystal X-ray diffraction at the University of Arizona, are a = 9.834(6) $\AA$, b = 9.023(5) $\AA$, c = 5.237(2) $\AA$, β = 104.70(3) ° and V0 = 449.5(6) $\AA^3$. For comparison, the sample used by [3] was a synthetic $CaFeSi_2O_6$ hedenbergite.

A large approximately 1 mm^3 specimen of hedenbergite was crushed into smaller pieces in a mortar under methanol. One small platelet-shaped crystal with approximate size 0.025 × 0.025 × 0.005 mm was loaded into a diamond anvil cell (DAC). The sample crystal was oriented with [1 1 0]

direction along the DAC axis.

Diamond anvils with 0.250 mm culet size and Re gasket preindented to a thickness of ∼0.042 mm were used. We utilized a combination of cubic boron nitride cBN(upstream) and tungsten carbide WC (downstream) backing plates. The angular access to the sample through the WC seat was ±13°; however, two additional rotation ranges, from -30° to -20° and from 20° to 30°, could be accessed thanks to the low X-ray absorption coefficient of the cBN seat. In the remaining two rotation ranges, from -20° to -13° and from 13° to 20°, strong powder diffraction signal caused by the transmitted beam touching the WC seat cone contaminated the diffraction images and this data were not used for further analysis. The gasket hole with initial diameter of ∼0.160 mm was filled with Ne pressure medium, using the GSECARS/COMPRES gas loading apparatus [50]. Two small ruby spheres were placed in the sample chamber together with the sample crystal for pressure calibration. Pressure was calculated from the shift of the R1 ruby fluorescence line [58]. The diffraction experiments were carried out at the GSECARS facility at APS, Argonne National Laboratory, in experimental station 13IDD. Monochromatic beam with incident energy of 37 keV was focused by a pair of KirkpatrickBaez mirrors to a spot of 0.003 by 0.005 mm. Diffraction images were collected using a MAR165 charge-coupled device(CCD) detector, placed at a sample-to-detector distance of approximately 200 mm. During the exposure, the sample was rotated about the vertical axis of the instrument (ω) in the three accessible rotation ranges, with a typical exposure time of 0.5 s/°. Diffraction images were collected at three different detector positions, differing by a translation of 70 mm perpendicular to the incident beam. The detector geometry parameters at each detector position were calibrated with a CeO_2 NIST diffraction standard. In addition to the full-rotation exposures, a step scan with 1° rotation steps was performed at each pressure. The sample was compressed in approximately 5 GPa steps, with full data collection at each step. The pressure range covered was 0.0001-29.9(1) GPa.

Diffraction images were analyzed using the GSE_ADA/RSV software package [64]. Integrated peak intensities were corrected for Lorenz, polarization, DAC absorption and sample displacement effects using the methods implemented in GSE_ADA [64]. Because of high incident energy, negligible sample thickness and low X-ray absorption coefficient of the sample at 37 keV, the sample absorption effect was ignored. Corrected peak intensities were used for least-squares structure refinement with SHELXL [86], which started from the C2/c ambient pressure structure model of [40]. Because of the limited number of unique observations, anisotropic atomic displacement parameters (ADPs) were used only for the non-oxygen atoms, whereas oxygen atoms were modeled with isotropic ADPs. According to the microprobe analysis, the M2 site was fully (within experimental uncertainty) occupied by Ca^{2+} and any attempts at refining the site occupancy factor (SOF) for this site resulted in convergence to SOF = 1; therefore, in the final refinement, this parameter was fixed to one. Occupancy model was also not refined for Si^{4+} and oxygen sites. For the M1 site, we assumed that Mn^{2+} and Fe^{2+}, having almost the same atomic number, are undistinguishable with X-rays and

treated both of these cations as Fe^{2+}. We modeled cation disorder at the M1 site assuming substitution of Fe^{2+}/Mn^{2+} with Mg^{2+} and constraining the sum of the two SOFs to one (no vacancy model). The SOF model of M1 site was only refined at the lowest pressure point and was fixed to be a constant at high pressures. The positions and ADPs of Fe^{2+} and Mg^{2+} were fixed to be the same. The substitution model for the M1 site at 1.9(1) GPa, based on refined SOFs for Mg^{2+} and Fe^{2+}/Mn^{2+}, is consistent with the microprobe results. Extinction parameter was also refined. Details of the crystal structure refinements, final fractional atomic coordinates and ADPs, as well as selected bond lengths and angles at the six pressures studied, are presented in tables 2.1, 2.2 and 2.3. VESTA was used to calculate polyhedral volume.

Raman spectra were collected at GSECARS offline system at the Advanced Phonon Source, Argonne National Laboratory. Raman scattering was excited with 514 nm green laser. The laser was focused on the sample by a 10× objective to a spot of few micrometers. Raman spectra were collected with a Horiba HR460 spectrometer equipped with 1800 lines/mm grating. A 30 μm spatial filter was used. The Roper Scientific LN/CCD-1340/100-EB/1 liquid nitrogen cooled CCD was used as detector.

2.4 Results

2.4.1 Axial compressibilities of hedenbergite

Unit cell parameters of hedenbergite up to 29.9(1) GPa are listed in table2.4. Normalized unit cell parameters of this study along with [87] are shown in figure 2.1. Our low-pressure results show good agreement with the previous study. No discontinuity in the pressure dependence of any of the parameters is found up to 29.9(1) GPa.

Axial compressibility β_{l0} is defined as

$$\beta_{l0} = \frac{1}{3K_{l0}} = -(\frac{1}{l}\frac{\partial l}{\partial P})_T \tag{2.1}$$

where K_{l0} is the linearized modulus at ambient pressure, l is axis length and P and T represent pressure and temperature, respectively. K_{l0} is obtained by weighted least-squares fit of the second-order linearized Birch-Murnaghan (BM2) equation of state as shown below [88]:

$$P(l) = \frac{3K_{l0}}{2}[(\frac{l_0}{l})^7 - (\frac{l_0}{l})^5] \tag{2.2}$$

The three crystallographic axes a, b and c of hedenbergite exhibit different compressibilities. The results of linearized second-order Birch-Murnaghan equation of state fitting are shown as solid lines in figure 2.1. Axial compressibility of a, b and c are calculated to be 1.7(2), 4.9(5), 2.13(9) $\times 10^{-3}$ GPa^{-1} by BM2. β in figure 2.1 is fit with third-order polynomial fitting.

2.4.2 Equation of state of hedenbergite

The bulk modulus K_{T0} and its pressure derivative K_{T0}' can be determined with a weighted nonlinear least-squares fitting of third-order Birch-Murnaghan equation of state(BM3):

$$P(V) = \frac{3K_{T0}}{2}[(\frac{V_0}{V})^{7/3} - (\frac{V_0}{V})^{5/3}]1 + \frac{3}{4}(K'_{T0} - 4)[(\frac{V_0}{V})^{2/3} - 1] \tag{2.3}$$

where P is pressure and V and V_0 represent the volume at high pressure and ambient pressure, respectively [88]. The bulk modulus K_{T0} and K_{T0}' are determined to be 131(4) GPa and 3.8(3) in this study, as shown in table 2.5. Considering the trade-off between K_{T0} and K_{T0}', the confidence ellipses (with a confidence level of ± 68.3%) of this study and previous study are shown in figure 2.2. Previous study has a smaller bulk modulus K_{T0} and a wider range of K_{T0}'. Second-order Birch-Murnaghan equation of state (BM2) is also obtained with K = 128.3(5) GPa.
Figure 2.3 shows the $f_E - F_E$ plot, depicting a relationship between Eulerian strain f_E and Birch normalized stress F_E; thus, K_{T0} and K_{T0}' can also be determined from a weighted linear least-squares fitting [88].

$$F_E = K_{T0}[1 + 1.5f_E(K'_{T0} - 4)] \tag{2.4}$$

where

$$f_E = [(V/V_0)^{-2/3} - 1]/2 \tag{2.5}$$

and

$$F_E = P/[3f_E(1 + 2f_E)^{5/2}] \tag{2.6}$$

In Eqs. 3.2-3.4, P is pressure and V and V_0 represent the volume at high and ambient pressures, respectively. K_{T0} = 128(2) GPa and K_{T0}' = 4.0(2) are determined using weighted linear least-squares fitting and are in good agreement with the results of BM3 fitting discussed above.

2.4.3 Polyhedral compression in hedenbergite

Figures 2.4, 2.5 and table 2.6 report the bond lengths and polyhedron volumes of SiO_4 tetrahedron, FeO_6 octahedron and CaO_8 polyhedron. The three polyhedra show anisotropic compressibility, usually shorter bond lengths show lower compressibility and smaller polyhedra show lower compressibility. It is interesting to notice that there are crossovers in bond lengths for all three polyhedra; however, they do not seem to cause any discontinuous changes in the compression mechanism.

SiO_4 tetrahedron

SiO_4 tetrahedron has the smallest volume of ∼2.1 $\AA^3$ and shows the lowest volume compression of 2.0(1) × 10^{-3} GPa^{-1} between 1.9(1) GPa and 29.9(1) GPa, as shown in table 2.6 and figure 2.5.

Four unique pairs of bond lengths along with the average bond length are shown in figure 2.4(a) and table 2.6. The average Si-O bond length decreases continuously with a lowest compressibility of 1.07(8) $\times$ 10^{-3} GPa^{-1} among the three polyhedra, while individual bond behavior shows minor irregularities. Si#0-O(3)#2 is the longest bond between 0 GPa and 5.9(1) GPa, while Si#0-O(3)#1 is the second longest bond. These two bonds show anomalous behavior at 12.7(1) GPa; however, we attribute this anomaly to possible experimental error and omit that pressure point in polynomial fittings shown in figure 2.4(a). A turnover is found in the two shorter Si-O bonds between 5.6(1) and 12.7(1) GPa.

M1 octahedron

Between 1.9(1) and 29.9(1) GPa, the volume of the M1 octahedron decreases from 12.48 to 10.72 $\mathring{A}^3$ and shows a compressibility of 5.2(2) $\times$ 10^{-3} GPa^{-1}, as listed in table 2.6 and figure 2.5. There are three different bond lengths in FeO_6 octahedron, and they show some anisotropy of compression behavior as shown in figure 2.4(b) and table 2.6. The shortest bond Fe(1)#0-O(1)#11 shows a medium compression. Fe(1)#0-O(1)#14 is the longest bond at low pressure and shows the largest compressibility, while the second longest bond, Fe(1)#0-O(1)#4, displays the smallest compression among the three bonds, thus leading to a crossover of the two bonds somewhere between 5.9(1) and 12.7(1) GPa. This crossover was also observed by [3]. The average bond displays a compressibility of 3.7(1) $\times$ 10^{-3} GPa^{-1} which is medium among the three polyhedra.

M2 polyhedron

As shown in table 2.6 and figure 2.5, the larger polyhedral site, CaO_8, has a volume of 25.58 $\mathring{A}^3$ at 1.9(1) GPa and 21.96 $\mathring{A}^3$ at 29.9(1) GPa and is characterized by an average compressibility of 5.1(7) $\times$ 10^{-3} GPa^{-1} from 1.9(1) to 29.9(1) GPa. Four unique bond lengths are shown in figure 2.4(c) and table 2.6. The longest bond Ca(2)#0-O(3)#6 shows the highest compressibility, while the second longest bond Ca(2)#0-O(3)#9 displays a second largest compressibility; therefore, a crossover is observed at $\sim$5.9(1) GPa. The shortest bond is Ca(2)#0-O(2)#6 and shows a smallest compression, while the second shortest bond Ca(2)#0-O(2)#3 has a second smallest compression, with a turnover of these two bond lengths at $\sim$5.5(1) GPa. The average bond length reveals a compressibility of 5.2(6) $\times$ 10^{-3} GPa^{-1} which is the highest among the three polyhedra.

Raman spectroscopy

Raman spectroscopy experiments were conducted on the same hedenbergite sample up to $\sim$33 GPa. The Raman spectra of hedenbergite at 2.0(1), 17.4(1) and 32.8(1) GPa are shown in figure 2.6(a). The peaks are fit with a Gaussian function and labeled ν1 - ν13 (figure 2.6(b)). Our results show a good agreement with previous ambient study (table 7) by [89] and the data from University of

Arizona RRUFF collection database. In our experiment, 13 Raman modes were observed between 200 and 1200 cm^{-1}. Group theory analysis predicts 20 Raman active modes [90]. The reason why there are less observed modes in our experiments may be that some modes are too weak to be detected by our spectrometer or the spatial resolution is not sufficient to distinguish peaks that are very close to each other. Due to cation substitution in the M1 site, broadening of the M-O bend/stretch modes are expected [91, 89].

2.5 Discussion

2.5.1 Compression mechanism

Hedenbergite belongs to chain silicates, with single chains of SiO_4 tetrahedron along the c axis, sandwiched by FeO_6 octahedron and CaO_8 polyhedron sheets, oriented in b-c plane. The SiO_4 tetrahedron, FeO_6 octahedron and CaO_8 polyhedron constitute about 38% volume of the unit cell. These polyhedra are compressed by ∼15% between 1.7(1) and 29.9(1) GPa.

In this study, the axial compressibilities of a, b and c are calculated to be 1.7(2), 4.9(5), 2.13(9) $\times 10^{-3}$ GPa^{-1}. [3] adopted a different compressibility fitting algorithm, which causes an apparent discrepancy in values. Recalculating the axial compressibility of [3] with our method yields 2.3(9), 4(1) and 2.9(5) $\times 10^{-3}$ GPa^{-1} for a, b and c axis, respectively. Our results show similar pattern in the ratio of 1:2.83:1.22, as compared to 1:1.77:1.28 determined by the previous authors. In general, b shows the highest compressibility and c axis is more compressible than a. Brillouin scattering determined the elastic moduli C_{11}, C_{22} and C_{33} to be 222(6), 176(5) and 249(5) GPa [92], which correlates well with our axial compressibility ratios. However, our results show that b axis is more compressible than indicated by the previous data. Diopside is a Ca, Mg end-member pyroxene, which is related to hedenbergite by substituting Fe^{2+} with Mg^{2+}. We calculated the compressibility of diopside [3] with our method and obtained 3(1), 4(1) and 3.0(5) $\times 10^{-3}$ GPa^{-1} for a, b and c axes. Similar to hedenbergite, also in diopside, the b axis has the highest compressibility. However, in contrast to hedenbergite, where c axis is more compressible than a, a and c have almost equal axial compressibility in diopside. The decrease in compressibility of c axis in diopside may be caused by the lower compressibility of MgO_6 compared to FeO_6 along the chain [3]. Different pressure range of data can also contribute to the discrepancy between our data and [3]'s.

Figure 2.2 presents the confidence ellipses of this study and [3]'s data calculated by our method. We obtained K_{T0} = 131(4) GPa and K_{T0}' = 3.8(3) for this study and K_{T0} = 118(3) GPa and K_{T0}' = 4.2(7) for [3]'s. Our results show higher bulk modulus K_{T0} but lower K_{T0}'. The discrepancy between these two data is likely due to the trade-off between K_{T0} and K_{T0}', but could also be related to the compositional differences and different pressure ranges. For the diopside data [3], the bulk modulus and its pressure derivative calculated with our method are K_{T0} = 108.3(3) GPa and K_{T0}' = 5.4(6). Comparing hedenbergite and diopside, the latter has lower bulk modulus, which

was also noted by [3].
The geometry of the SiO_4 tetrahedral chain and pressure evolution of the O3-O3-O3 angle are shown in figure 2.8 and table 2.6. The angle O3-O3-O3 (θ in figure 2.8(a)) is defined by the O3 atoms which form the two longest bonds with Si as shown by the red and magenta bonds in figures 2.8(b) and (c) (color of the bonds is consistent with figure 2.4(a)). The O3-O3-O3 angle is 163.7(2)° at 1.9(1) GPa and decreases, in general, as pressure increases which contributes to the axial compression along with the bond length decrease. The O3-O3-O3 angle remains almost unchanged from 5.9(1) to 12.7(1) GPa and even increases from 18.0(1) to 24.5(1) GPa; therefore, the decrease in Si-O3 bond lengths contributes mostly to the c axis compression in these pressure ranges.

2.5.2 Polyhedral distortion in hedenbergite

The polyhedral distortion can be described by angle variance and mean quadratic elongation parameters proposed by [93]. The angle variance of the three polyhedra is shown in Fig. 8a. Angle variance is defined as $\sigma^2 = \sum_{i=1}^{n}[(\theta_i - \theta_0)^2/(n-1)]$, where θ_i is the ith angle, θ_0 is the angle of ideal polyhedron of the same volume and n is the number of bonds. SiO_4 tetrahedron shows a medium angle variance of ∼30 and remains almost constant as pressure changes. FeO_6 octahedron shows the smallest angle variance of ∼14 at low pressure and starts to increase somewhere between 12.7(1) and 18.0(1) GPa and reaches ∼33 at 29.9(1) GPa. The CaO_8 polyhedron is already quite distorted at ambient conditions and has the largest angle variance of ∼150; however, the distortion decreases linearly with pressure. It is interesting to notice that the drop in angle variance somewhere between 18.0(1) to 24.5(1) GPa can be the main factor that contributes to the decrease in CaO_8 polyhedral compressibility starting from 18.0(1) GPa.
Mean quadratic elongation is defined as $< \lambda >= \sum_{i=1}^{n}[(l_i/l_0)^2/n]$ where l_0 is the center-to-vertex distance of a regular polyhedron of the same volume, l_i is the i^{th} center-to-vertex distance and n is the number of bonds. In figure 2.7(b), both SiO_4 and FeO_6 show a mean quadratic elongation >1. The mean quadratic elongation of SiO_4 remains almost constant as pressure changes, just like in the case of the angle variance. However, the quadratic elongation of FeO_6 starts to increase somewhere between 12.7(1) and 18.0(1) GPa, which indicates an increase in distortion. CaO_8 has a mean quadratic elongation <1, which decreases gradually as pressure increases, also indicating increasing distortion.

2.5.3 Raman mode variation with pressure

Modes are assigned by comparing our results with previous ambient pressure data [89]. Four modes(ν1 - ν6) are assigned to M-O stretch or O-M-O bend (M = Ca^{2+} , Fe^{2+}, Mg^{2+}, Mn^{2+}), three modes (ν7 - ν9) are assigned to O-Si-O bend, and four modes (ν10 - ν13) are assigned to Si-O stretch. Two additional modes (ν1, ν2) are reported by [89], but not in this study. The reason for

this may be that these peaks are too weak or the difference in chemical composition and ordering causes them to be obscured. Our study also observed three modes $\nu 2$, $\nu 6$ and $\nu 9$ that were not reported previously. These peaks are very weak at low pressure and as pressure increases, they start to diverge, as shown in figure 2.6. Such phenomenon was also observed by [91]. The reason for the divergence of the two peaks may be the anisotropic compression making the crystal distorted, thus enhancing the difference between two peaks. In general, frequency increases as pressure increases, since compression generally strengthens bond, thus increasing the force constants. It is interesting to notice some discontinuities as frequencies increase. These phenomena are related to the discontinuous change in bond length and angles in the structure.

2.6 Conclusions

We reported results of high-pressure single-crystal X-ray diffraction and Raman spectroscopy experiments conducted on natural Ca, Fe end-member pyroxene (hedenbergite) up to ∼33 GPa in diamond anvil cell. Unit cell parameters exhibit continuous decrease on compression. Axial compressibilities of hedenbergite up to ∼30 GPa are calculated to be 1.7(2), 4.9(5) and 2.13(9) $\times$ 10^{-3} GPa^{-1}, respectively, and show a highest compressibility of b and lowest compressibility of a. Our data show similar results in compressibilities with previous studies. Diopside shows a highest compressibility of b but almost equal compressibilities of a and c. The difference between hedenbergite and diopside may be caused by the different compressibilities of FeO_6 and MgO_6 polyhedra. Bulk modulus and its pressure derivate for hedenbergite are calculated to be 131(4) GPa and 3.8(3), respectively, by fitting third-order Birch-Murnaghan equation of state. The bulk modulus of hedenbergite is higher than that of diopside (108.3(3) GPa), but its pressure derivative is lower than that of diopside(5.4(6)).
Bond lengths are also discussed in this study. Generally, longer bonds show higher compressibilities except for some of the Si-O bonds. SiO_4, the smallest polyhedron, shows the lowest compressibility. Angle and elongation distortions are observed in three polyhedra at high pressure. Thirteen vibrational modes are observed with Raman spectroscopy up to ∼33 GPa. In general, mode frequencies increase as pressure increase.

2.7 Acknowledgements

The project was supported by the National Science Foundation Division of Earth Sciences Geophysics Grant No.1344942. Portions of this work were performed at GeoSoilEnviroCARS(Sector 13), Advanced Photon Source (APS), and Argonne National Laboratory. GeoSoilEnviroCARS is supported by the National Science Foundation—Earth Sciences (EAR-1128799) and Department of Energy—Geosciences (DE-FG02-94ER14466). Use of the Advanced Photon Source was supported by the US Department of Energy, Office of Science, Office of Basic Energy Sciences, under Con-

tract No. DE-AC02-06CH11357. We would also like to thank Carnegie-DOE Alliance Center for support through Academic Partner subcontract to PD and Prof. R. T. Downs at the University of Arizona for kindly providing the samples from RRUFF collections. We would like to thank the two reviewers, Diego Gatta and Jennifer Kung for helpful comments.

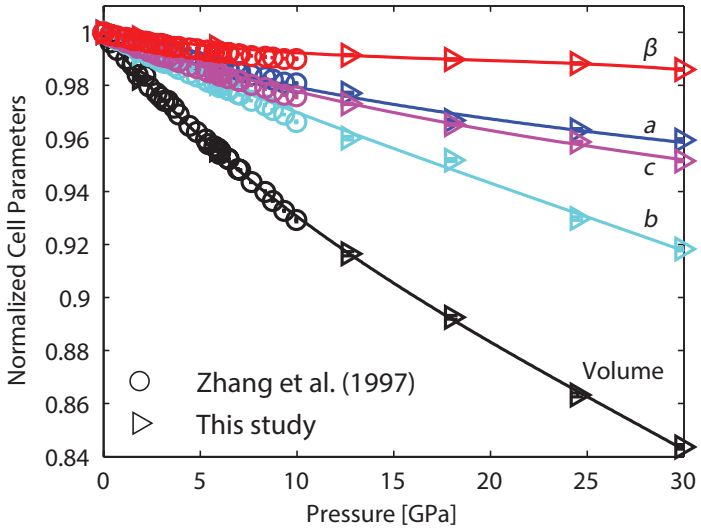

Figure 2.1: Pressure dependence of normalized unit cell parameters $\frac{a}{a_0}$, $\frac{b}{b_0}$, $\frac{c}{c_0}$, $\frac{\beta}{\beta_0}$, $\frac{V}{V_0}$. Circles are data reported by [3]. Triangles represent results of this study. Error bars are smaller than the symbol size.

Table 2.6: Selected bond lengths($\mathring{A}$), angles (°), average bondlength and polyhedral volume(Å^3) of hedenbergite up to 29.9(1) GPa. Symmetry transformations used to generate equivalent atoms are given below: #0 x, y, z; #1 x, y, z1; #2 x, y, z1/2; #3 x + 1/2, y + 1/2, z + 1; #4 x, y + 1, z; #5 x + 1/2, y1/2, z; #6 x1/2, y + 1/2, z1/2; #7 x, y, z + 1/2; #8 x + 1/2, y + 1/2, z + 3/2; #9 x1/2, y + 1/2, z1; #10 x1/2, y + 1/2, z; #11 x + 1/2, y + 1/2, z + 1/2; #12 x, y + 1, z + 1/2; #13 x, y + 1, z; #14 x, y + 1, z + 1/2; #15 x, y + 2, z + 1; #16 x, y + 2, z; #17 x, y + 1, z + 1; #18 x, y1, z; #19 x, y, z + 1; #20 x, y, z + 1/2; #21 x + 1/2, y1/2, z + 1

Pressure(GPa)	1.9(1)	5.9(1)	12.7(1)	18.0(1)	24.5(1)	29.9(1)
SiO_4 tetrahedron						
Si#0-O(1)#0	1.599(6)	1.58(1)	1.56(1)	1.55(1)	1.555(6)	1.54(1)
Si#0-O(2)#0	1.575(6)	1.57(1)	1.59(1)	1.57(1)	1.556(7)	1.57(1)
Si#0-O(3)#1	1.669(4)	1.676(8)	1.699(8)	1.654(8)	1.645(6)	1.638(7)
Si#0-O(3)#2	1.691(5)	1.677(9)	1.629(9)	1.685(9)	1.671(6)	1.664(9)
Mean Si-O length	1.634(5)	1.63(1)	1.62(1)	1.61(1)	1.607(6)	1.60(1)
O(1)#0-Si#0-O(3)#1	110.5(2)	110.9(4)	111.6(4)	111.9(5)	110.8(3)	110.5(5)

O(1)#0-Si#0-O(3)#2	110.4(3)	111.2(5)	112.6(5)	112.4(5)	113.1(3)	112.9(5)
O(2)#0-Si#0-O(1)#0	117.9(3)	117.1(5)	115.2(6)	115.2(6)	115.4(4)	115.1(6)
O(2)#0-Si#0-O(3)#1	109.9(3)	109.9(5)	110.0(4)	110.1(5)	111.3(3)	111.9(4)
O(2)#0-Si#0-O(3)#2	103.5(3)	103.8(4)	104.4(5)	104.8(5)	104.1(3)	104.5(5)
O(3)#1-Si#0-O(3)#2	103.5(2)	102.8(3)	102.1(3)	101.2(4)	101.0(2)	100.8(3)
Volume	2.2168	2.1857	2.1593	2.1423	2.1065	2.0910
σ_2	28.7800	27.8075	25.3124	27.8421	30.6758	29.9833
$< \lambda >$	1.0070	1.0069	1.0068	1.0071	1.0078	1.0076
FeO_6 octahedron						
Fe(1)#0-O(2)#10	2.076(6)	2.06(1)	2.02(1)	2.00(1)	1.982(6)	1.970(9)
Fe(1)#0-O(2)#11	2.076(6)	2.06(1)	2.02(1)	2.00(1)	1.982(6)	1.970(9)
Fe(1)#0-O(1)#12	2.120(4)	2.116(8)	2.120(8)	2.090(8)	2.060(5)	2.06(1)
Fe(1)#0-O(1)#4	2.120(4)	2.116(8)	2.120(8)	2.090(8)	2.060(5)	2.06(1)
Fe(1)#0-O(1)#13	2.140(6)	2.13(1)	2.09(1)	2.07(1)	2.036(7)	2.01(1)
Fe(1)#0-O(1)#14	2.140(6)	2.13(1)	2.09(1)	2.07(1)	2.036(7)	2.01(1)
Mean Fe-O length	2.112(5)	2.10(1)	2.08(1)	2.06(1)	2.026(6)	2.01(1)
O(1)#12-Fe(1)#0-O(1)#13	92.2(2)	92.4(4)	92.3(4)	92.7(4)	93.1(3)	92.5(4)
O(1)#12-Fe(1)#0-O(1)#14	87.0(2)	88.1(4)	89.6(4)	89.1(4)	88.8(2)	88.8(4)
O(1)#13-Fe(1)#0-O(1)#14	80.7(3)	80.5(6)	80.8(6)	80.2(6)	81.8(4)	82.1(5)
O(1)#4-Fe(1)#0-O(1)#13	87.0(2)	88.1(4)	89.6(4)	89.1(4)	88.8(2)	88.8(4)
O(1)#4-Fe(1)#0-O(1)#14	92.2(2)	92.4(4)	92.3(4)	92.7(4)	93.1(3)	92.5(4)
O(2)#10-Fe(1)#0-O(1)#12	92.3(2)	91.7(3)	91.1(4)	91.0(3)	90.9(2)	90.9(3)
O(2)#10-Fe(1)#0-O(1)#14	93.6(2)	93.3(4)	91.5(4)	90.8(4)	88.2(3)	86.1(4)
O(2)#10-Fe(1)#0-O(1)#4	88.5(2)	87.9(4)	87.3(4)	87.4(4)	87.5(2)	88.1(4)
O(2)#10-Fe(1)#0-O(2)#11	92.4(3)	93.2(6)	96.3(6)	98.5(6)	102.0(4)	106.0(6)
O(2)#11-Fe(1)#0-O(1)#12	88.5(2)	87.9(4)	87.3(4)	87.4(4)	87.5(2)	88.1(4)
O(2)#11-Fe(1)#0-O(1)#13	93.6(2)	93.3(4)	91.5(4)	90.8(4)	88.2(3)	86.1(4)
O(2)#11-Fe(1)#0-O(1)#4	92.3(2)	91.7(3)	91.1(4)	91.0(3)	90.9(2)	90.9(3)
Volume	12.4836	12.2891	11.8387	11.4816	10.9788	10.7204
σ_2	14.6060	14.0974	14.3422	18.2916	23.1345	33.8212
$< \lambda >$	1.0044	1.0042	1.0047	1.0057	1.0069	1.0100
CaO_8 polyhedron						
Ca(2)#0-O(1)#0	2.352(7)	2.33(1)	2.29(1)	2.27(1)	2.254(7)	2.24(1)
Ca(2)#0-O(1)#7	2.352(7)	2.33(1)	2.29(1)	2.27(1)	2.254(7)	2.24(1)
Ca(2)#0-O(2)#3	2.333(4)	2.316(7)	2.304(8)	2.299(8)	2.291(5)	2.283(9)
Ca(2)#0-O(2)#6	2.333(4)	2.316(7)	2.304(8)	2.299(8)	2.291(5)	2.283(9)
Ca(2)#0-O(3)#3	2.675(6)	2.592(9)	2.499(8)	2.460(9)	2.430(6)	2.400(8)

Ca(2)#0-O(3)#6	2.675(6)	2.592(9)	2.499(8)	2.460(9)	2.430(6)	2.400(8)
Ca(2)#0-O(3)#8	2.605(6)	2.588(9)	2.545(9)	2.515(9)	2.455(7)	2.45(1)
Ca(2)#0-O(3)#9	2.605(6)	2.588(9)	2.545(9)	2.515(9)	2.455(7)	2.45(1)
Mean Ca-O length	2.491(6)	2.456(9)	2.408(9)	2.387(9)	2.358(6)	2.344(9)
O(3)#8-Ca(2)#0-O(3)#3	59.98(9)	60.8(2)	61.8(2)	62.5(2)	63.2(1)	63.3(2)
O(3)#9-Ca(2)#0-O(3)#6	59.98(9)	60.8(2)	61.8(2)	62.5(2)	63.2(1)	63.3(2)
O(2)#3-Ca(2)#0-O(3)#8	62.3(2)	62.5(4)	63.0(3)	64.6(3)	64.8(2)	65.4(3)
O(2)#6-Ca(2)#0-O(3)#9	62.3(2)	62.5(4)	63.0(3)	64.6(3)	64.8(2)	65.4(3)
O(3)#8-Ca(2)#0-O(3)#6	67.1(2)	67.0(3)	66.8(3)	67.1(3)	68.1(2)	69.1(3)
O(3)#9-Ca(2)#0-O(3)#3	67.1(2)	67.0(3)	66.8(3)	67.1(3)	68.1(2)	69.1(3)
O(1)#0-Ca(2)#0-O(1)#7	72.2(3)	72.4(5)	72.7(6)	71.9(5)	72.5(3)	72.1(5)
O(2)#3-Ca(2)#0-O(1)#7	80.5(2)	80.4(3)	80.1(3)	79.4(3)	78.7(2)	78.8(4)
O(2)#6-Ca(2)#0-O(1)#0	80.5(2)	80.4(3)	80.1(3)	79.4(3)	78.7(2)	78.8(4)
O(2)#3-Ca(2)#0-O(1)#0	81.9(2)	80.6(3)	78.1(3)	77.2(3)	76.2(2)	74.3(4)
O(2)#6-Ca(2)#0-O(1)#7	81.9(2)	80.6(3)	78.1(3)	77.2(3)	76.2(2)	74.3(4)
O(3)#8-Ca(2)#0-O(3)#9	82.5(2)	83.1(4)	84.7(4)	83.1(4)	84.8(3)	85.4(4)
O(2)#3-Ca(2)#0-O(3)#6	85.2(2)	86.3(3)	88.4(3)	88.3(3)	89.3(2)	91.1(3)
O(2)#6-Ca(2)#0-O(3)#3	85.2(2)	86.3(3)	88.4(3)	88.3(3)	89.3(2)	91.1(3)
O(1)#7-Ca(2)#0-O(3)#6	90.9(2)	90.6(3)	90.4(3)	89.6(3)	88.5(2)	88.0(3)
O(1)#0-Ca(2)#0-O(3)#3	90.9(2)	90.6(3)	90.4(3)	89.6(3)	88.5(2)	88.0(3)
Volume	25.5778	24.5878	23.2452	22.8337	22.1611	21.8551
σ_2	149.5173	147.1162	148.4800	132.6054	129.4928	133.7569
$< \lambda >$	0.9567	0.9537	0.9515	0.9462	0.9393	0.9350
O3-O3-O3	163.7(2)	161.9(4)	161.7(4)	158.4(4)	159.4(3)	158.1(4)

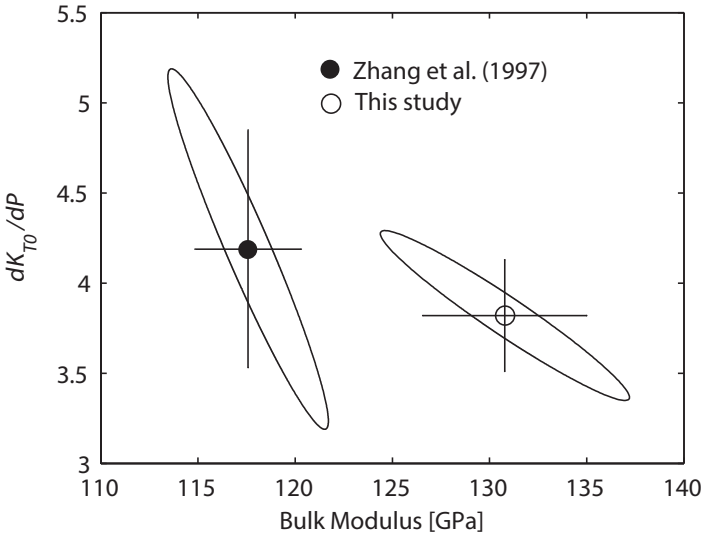

Figure 2.2: Confidence ellipses in K_{T0} and K_{T0}' for the fit of the third-order BirchMurnaghan equation of state to the hedenbergite P-V data. Data with the filled circles are from this study yielding $V_0 = 449.2(5)$ $\AA^3$, $K_{T0} = 131(4)$ GPa and $K_{T0}' = 3.8(3)$. Data with the open circles represent [3] giving $V_0 = 449.8(1)$ $\AA^3$, $K_{T0} = 118(3)$ GPa and $K_{T0}' = 4.2(7)$.

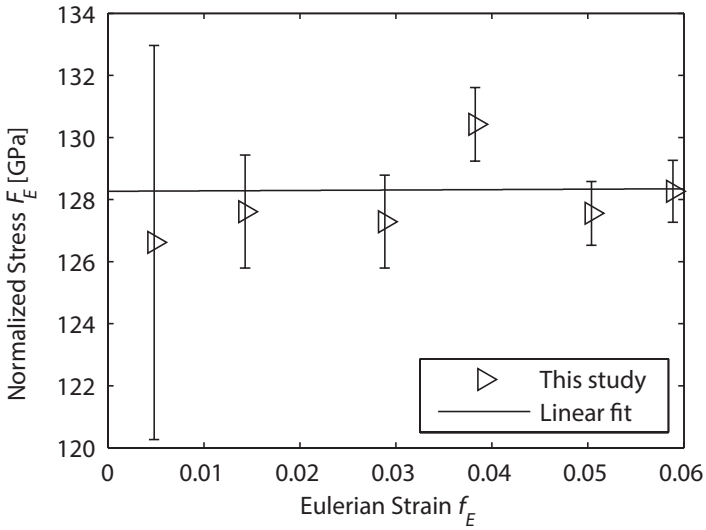

Figure 2.3: Birch's normalized stress F_E versus the Eulerian strain f_E. Triangles represent the data from this study. Bulk modulus K and its pressure derivative calculated from linear fit of this study are $K_{T0} = 128(2)$ GPa and $K_{T0}' = 4.0(2)$.

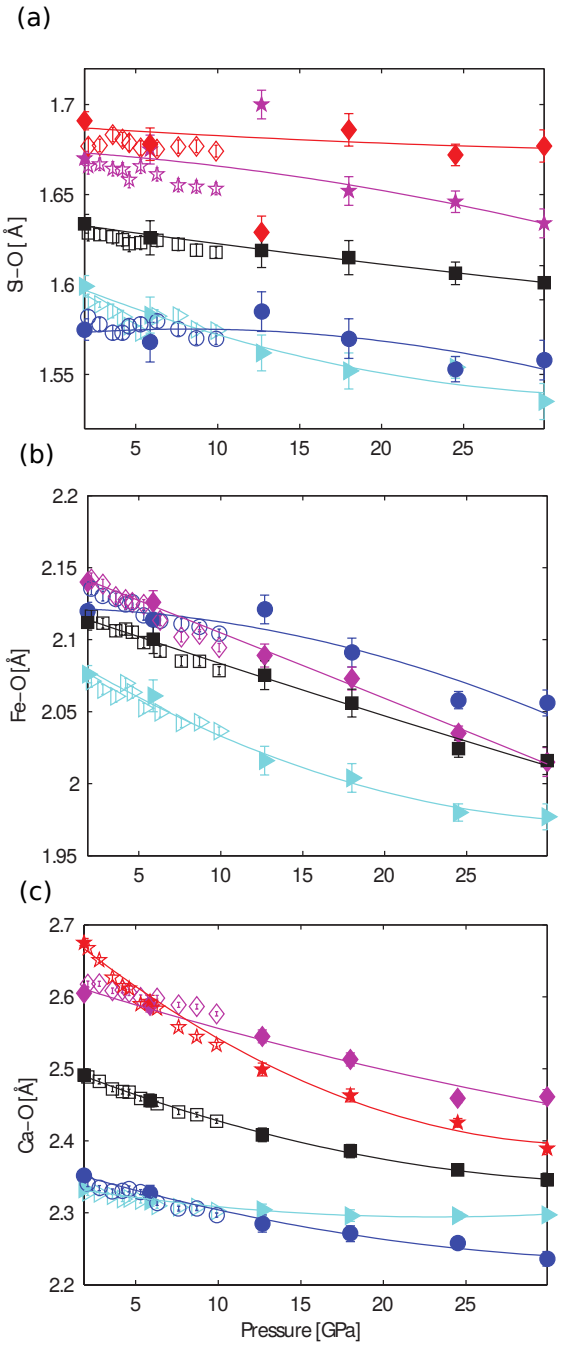

Figure 2.4: Bond lengths of hedenbergite. Data with filled markers are from this study, and those with open markers are from [3]. (a) SiO bond lengths of hedenbergite. There are four different SiO bond lengths, Si#0-O(3)#2, Si#0-O(3)#1, Si#0-O(2)#0 and Si#0-O(1)#0, which are represented by *diamonds*, *pentagrams*, *right−pointing triangles* and *circles*, respectively. The average Si-O bond lengths are marked with *squares*. The 12.7(1) GPa data points were excluded when doing second-order polynomial fitting for Si#0-O(3)#2 and Si#0-O(3)#1. (b) Fe-O bond lengths of hedenbergite. Six bonds with three different bond lengths are reported here. Fe(1)#0-O(1)#14 and Fe(1)#0-O(1)#13 have the same length and are represented by *diamonds*. Fe(1)#0-O(2)#4 and Fe(1)#0-O(2)#12 have the same bond length and are represented by *circles*. *Triangle* markers stand for Fe(1)#0-O(2)#11 and Fe(1)#0-O(2)#10, while the average bond lengths are represented by *squares*. (c) Ca-O bond lengths are reported. Ca(2)#0-O(3)#6 and Ca(2)#0-O(3)#3 are represented by *pentagrams*, and Ca(2)#0-O(3)#9 and Ca(2)#0-O(3)#8 are marked with *diamonds*. Data with *circles* are Ca(2)#0-O(1)#0 and Ca(2)#0-O(1)#7, while those of Ca(2)#0-O(1)#3 and Ca(2)#0-O(1)#6 are marked with *triangles*. Average values are represented by squares.

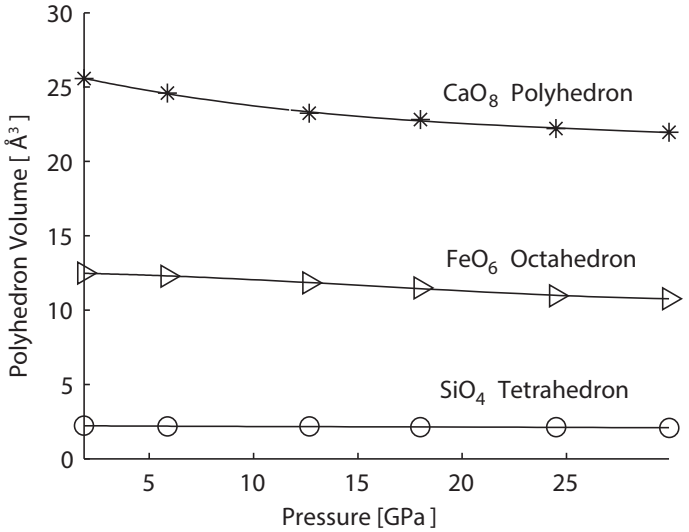

Figure 2.5: Pressure dependences of SiO_4 (*circle*), FeO_6 (*triangle*) and CaO_8 (*asterisk*) polyhedral volumes in hedenbergite.

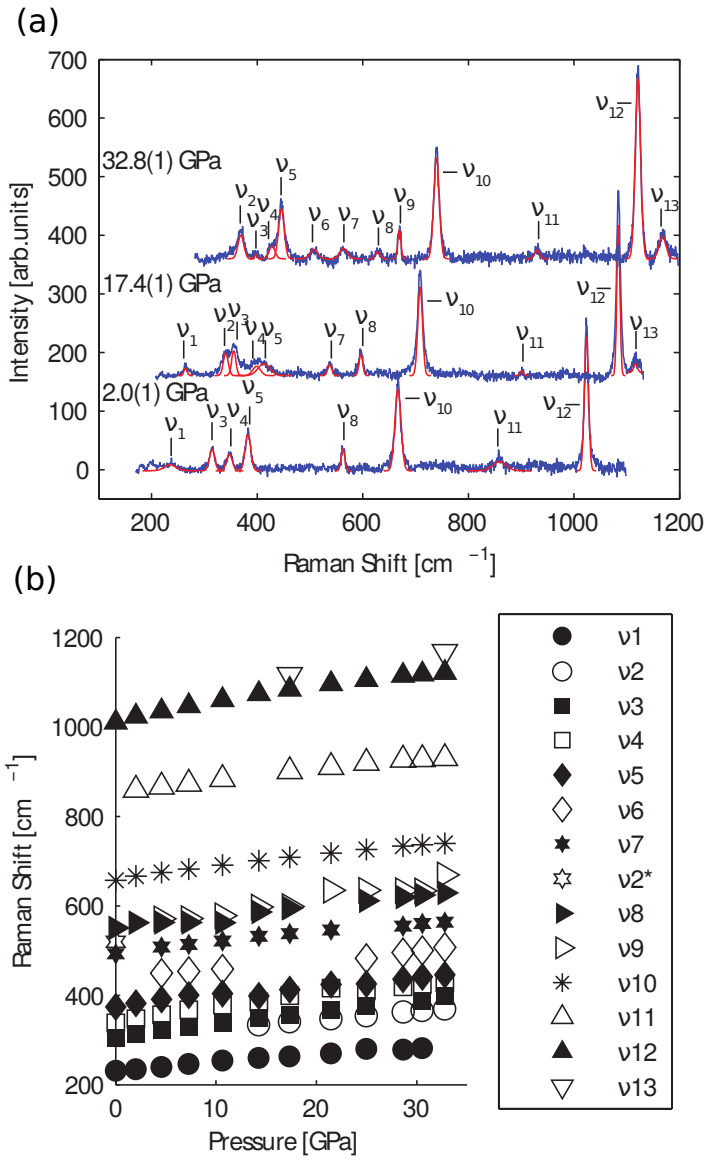

Figure 2.6: (a) Raman spectra of hedenbergite at 2.0(1), 17.4(1) and 32.8(1) GPa. (b) Raman peak positions of hedenbergite up to ∼33 GPa.

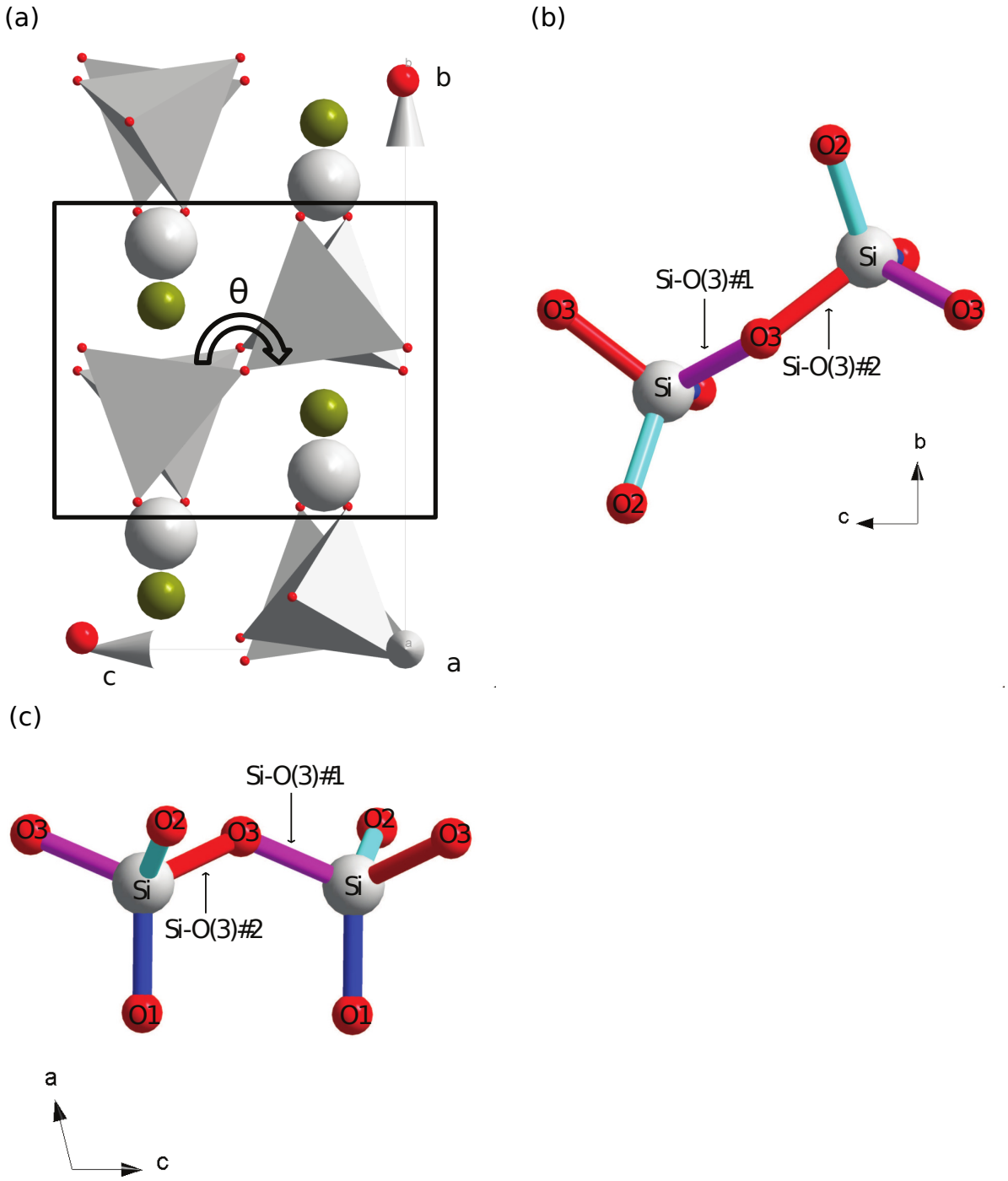

Figure 2.7: (a) Polyhedral illustrations of the SiO_4 tetrahedral chain, θ is O3-O3-O3 angle. (b) Illustration of bonds in SiO_4 tetrahedron viewed along a axis. (c) Illustration of bonds in SiO_4 tetrahedron viewed along b axis. Colors of the bonds are consistent with figure 2.4(a).

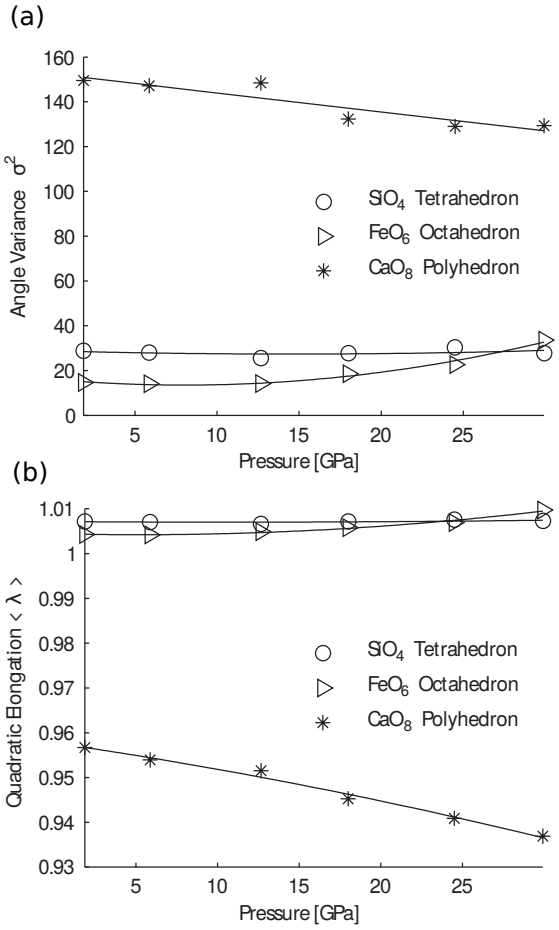

Figure 2.8: Angle variance (a) and quadratic elongation (b) of SiO_4 (*circle*), FeO_6 (*triangle*) and CaO_8 (*asterisk*) in hedenbergite up to 29.9(1) GPa

Table 2.1: Refinement results of hedenbergite up to 29.9(1) GPa

Pressure(GPa)	1.9(1)	5.9(1)	12.7(1)	18.0(1)	24.5(1)	29.9(1)
Wavelength(Å)			0.3033			
θ range for data collection	1.34-17.39	1.35-13.70	1.37-16.84	1.38-14.97	1.40-17.03	1.41-16.86
No. of reflections collected	480	326	296	329	423	336
No. of independent reflections	206	145	148	157	178	146
No. parameters refined	35	34	34	34	34	34
Limiting indices	-14≤h≤14 -12≤k≤10 -6≤l≤6	-13≤h≤10 -10≤k≤8 -5≤l≤6	-11≤h≤14 -11≤k≤6 -5≤l≤6	-11≤h≤12 -10≤k≤10 -5≤l≤5	-14≤h≤14 -10≤k≤10 -5≤l≤5	-13≤h≤14 -10≤k≤8 -5≤l≤5
R_{int}	0.0857	0.1301	0.134	0.103	0.0767	0.1005
Final R_1 and wR_2 (reflections I>2$\sigma(I)$)	0.0509, 0.1019	0.0663, 0.1320	0.0663, 0.1317	0.0682, 0.1548	0.0587, 0.1232	0.063, 0.1354
Final R_1 and wR_2 (all reflections)	0.0526, 0.1023	0.0674, 0.1334	0.0663, 0.1318	0.0688, 0.1550	0.0590, 0.1243	0.0659, 0.1357
Goodness of fit	1.089	1.193	1.092	1.041	1.177	1.056
$\Delta\rho_{max}$, $\Delta\rho_{min}$ (eÅ^{-3})	0.706, 0.869	0.828, 0.902	0.760, 1.051	1.125, 1.192	0.873, 0.942	0.800, 0.578
SOF of Fe			81.90%			
SOF of Mg			18.10%			

Table 2.2: Structural parameters of hedenbergite as a function of pressure.

Pressure(GPa)	1.9(1)	5.9(1)	12.7(1)	18.0(1)	24.5(1)	29.9(1)
Si						
x	0.2873(2)	0.2874(3)	0.2878(3)	0.2868(4)	0.2868(2)	0.2853(4)
y	0.0937(2)	0.0945(4)	0.0946(5)	0.0969(5)	0.0984(3)	0.0991(4)
z	0.2318(3)	0.2313(5)	0.2326(5)	0.2327(5)	0.2341(4)	0.2356(7)
Ca(2)						
x	0	0	0	0	0	0
y	0.3022(3)	0.3045(5)	0.3069(5)	0.3090(5)	0.3111(4)	0.3121(5)
z	0.25	0.25	0.25	0.25	0.25	0.25
Fe(1)						
x	0	0	0	0	0	0
y	0.9078(2)	0.9090(4)	0.9108(4)	0.9102(4)	0.9110(3)	0.9104(4)
z	0.25	0.25	0.25	0.25	0.25	0.25
Mg(1)						
x	0	0	0	0	0	0
y	0.9078(2)	0.9090(4)	0.9108(4)	0.9102(4)	0.9110(3)	0.9104(4)
z	0.25	0.25	0.25	0.25	0.25	0.25
O(1)						
x	0.1185(6)	0.119(1)	0.120(1)	0.119(1)	0.1182(6)	0.118(1)
y	0.0899(7)	0.092(1)	0.095(1)	0.095(1)	0.0944(8)	0.093(1)
z	0.1503(8)	0.152(2)	0.156(2)	0.154(2)	0.150(1)	0.151(2)
O(2)						
x	0.3620(5)	0.3612(9)	0.3598(9)	0.357(1)	0.3548(6)	0.352(1)
y	0.2473(6)	0.249(1)	0.256(1)	0.258(1)	0.2624(9)	0.267(1)
z	0.3248(8)	0.328(1)	0.331(1)	0.333(1)	0.337(1)	0.343(2)
O(3)						
x	0.3511(5)	0.3526(8)	0.3549(8)	0.3563(9)	0.3565(6)	0.3552(8)
y	0.0209(7)	0.023(1)	0.024(1)	0.028(1)	0.0272(8)	0.029(1)
z	0.9916(7)	0.986(1)	0.978(2)	0.987(1)	0.989(1)	0.9878(2)

Table 2.3: Atomic displacement parameters($\mathring{A}^2$) of hedenbergite as a function of pressure.

Pressure(GPa)	U_{11}	U_{22}	U_{33}	U_{23}	U_{13}	U_{12}
1.9(1)						
Si	0.005(2)	0.006(2)	0.010(1)	0.000(1)	0.000(1)	0.000(1)
Ca(2)	0.009(2)	0.011(2)	0.013(1)	0	0.001(1)	0
Fe(1)	0.005(1)	0.008(2)	0.011(1)	0	0.000(1)	0
Mg(1)	0.005(1)	0.008(2)	0.011(1)	0	0.000(1)	0
5.9(1)						
Si	0.013(3)	0.001(4)	0.011(2)	0.000(1)	0.001(1)	0.002(1)
Ca(2)	0.017(3)	0.007(4)	0.013(2)	0	0.001(1)	0
Fe(1)	0.009(3)	0.009(3)	0.012(2)	0	0.001(1)	0
Mg(1)	0.009(3)	0.009(3)	0.012(2)	0	0.001(1)	0
12.7(1)						
Si	0.003(3)	0.009(4)	0.008(2)	0.001(1)	0.002(1)	0.000(1)
Ca(2)	0.018(3)	0.000(4)	0.009(2)	0	0.004(1)	0
Fe(1)	0.002(2)	0.005(3)	0.007(1)	0	0.001(1)	0
Mg(1)	0.002(2)	0.005(3)	0.007(1)	0	0.001(1)	0
18.0(1)						
Si	0.009(3)	0.002(4)	0.008(2)	0.000(1)	0.001(1)	0.001(1)
Ca(2)	0.012(3)	0.004(4)	0.012(2)	0	0.001(1)	0
Fe(1)	0.005(2)	0.006(3)	0.011(2)	0	0.000(1)	0
Mg(1)	0.005(2)	0.006(3)	0.011(2)	0	0.000(1)	0
24.5(1)						
Si	0.006(2)	0.005(3)	0.012(2)	0.001(1)	0.000(1)	0.001(1)
Ca(2)	0.008(2)	0.011(3)	0.012(2)	0	0.000(1)	0
Fe(1)	0.006(2)	0.010(3)	0.011(1)	0	0.001(1)	0
Mg(1)	0.006(2)	0.010(3)	0.011(1)	0	0.001(1)	0
29.9(1)						
Si	0.004(2)	0.016(4)	0.008(2)	0.001(1)	0.001(1)	0.001(1)
Ca(2)	0.009(3)	0.008(4)	0.014(2)	0	0.000(1)	0
Fe(1)	0.005(2)	0.013(3)	0.012(2)	0	0.002(1)	0
Mg(1)	0.005(2)	0.013(3)	0.012(2)	0	0.002(1)	0

Table 2.4: Unit cell parameters of hedenbergite. [a] Data from RRUFF R070236. Standard deviations in the last decimal digit are given in parentheses.

Pressure(GPa)	a(Å)	b(Å)	c(Å)	$\beta(^\circ)$	Volume($\mathring{A}^3$)	ρ(g/cm^3)
0.00[a]	9.834(6)	9.023(5)	5.237(2)	104.70(3)	449.5(6)	3.586(5)
1.9(1)	9.787(4)	8.953(5)	5.226(1)	104.64(2)	443.1(3)	3.638(2)
5.9(1)	9.706(3)	8.852(4)	5.176(1)	104.29(2)	430.9(2)	3.741(2)
12.7(1)	9.615(4)	8.665(6)	5.111(2)	103.96(3)	413.2(3)	3.901(3)
18.0(1)	9.515(5)	8.591(5)	5.069(2)	103.78(3)	402.4(3)	4.006(3)
24.5(1)	9.480(5)	8.392(6)	5.035(2)	103.63(3)	389.2(3)	4.141(3)
29.9(1)	9.442(5)	8.288(6)	4.997(2)	103.39(3)	380.4(4)	4.237(4)

Table 2.5: Bulk modulus (K_{T0}) and its pressure derivatives (K_{T0}') of hedenbergite. PC polycrystalline sample, SC single-crystal sample

Composition	K_{T0}(GPa)	K_{T0}'	P_{max}(GPa)	Method	Reference
$Ca_{1.00}(Fe_{.67}Mn_{.16}Mg_{.17})Si_2O_6$, SC	131(4)	3.8(3)	29.91	X-ray	This study
$CaFeSi_2O_6$, SC	120		0	Brillouin	[92]
$CaFeSi_2O_6$, PC	119(2)	4	3.7	X-ray	[94]
$CaFeSi_2O_6$, SC	117(1)	4.3(4)	10	X-ray	[3]

Table 2.7: Assignment and frequencies (cm^{-1}) of observed Raman modes up to 32.8(1) GPa with comparison of reference. Modes with * are not observed by this study. [a] The ambient pressure point data are from the University of Arizona RRUFF collection #R070236.

Assignment	[89]	0.0(1)[a] GPa	2.0(1) GPa	4.6(1) GPa	7.3(1) GPa	10.7(1) GPa	14.3(1) GPa	17.4(1) GPa	21.5(1) GPa	25.0(1) GPa	28.6(1) GPa	30.6(1) GPa	32.8(1) GPa	Mode
M-O	234	231.5	235.3	240.3	247.1	254.1	259.6	264.2	269.8	279.6	278.4	281.5	—	1
stretch	242	—	—	—	—	—	—	—	—	—	—	—	—	1*
/bend	—	—	—	—	—	—	334.6	340.5	347.9	354.7	363.5	365.9	369.0	2
	304	304.8	314.6	322.0	329.8	338.4	348.6	355.6	368.3	375.4	—	388.2	397.3	3
	333	338.6	347.5	356.6	367.4	378.3	384.8	398.8	416.2	409.9	419.0	424.3	428.3	4
	372	373.9	382.4	391.1	400.2	403.8	398.5	412.7	—	425.6	435.9	441.0	445.8	5
	—	—	—	449.3	453.3	458.7	—	—	—	—	—	—	507.6	6
O-Si-O	492	492.7	—	508.1	514.0	521.2	531.9	537.5	545.7	—	—	560.2	563.6	7
bend	521	519.7	—	—	—	—	—	—	—	—	—	—	—	2*
	547	550.6	562.5	562.6	562.6	562.1	586.2	596.4		611.4	619.6	624.1	628.8	8
	—	—	—	—	571.6	578.1	597.2		634.9	634.5	634.2	633.9	669.2	9
Si-O	659	657.1	666.6	674.5	682.4	691.0	701.1	708.7	717.7	725.9	733.8	736.6	739.7	10
stretch	855	—	859.1	866.5	872.6	883.1	—	901.0	910.0	919.3	926.5	927.7	930.1	11
	1012	1010.5	1023.6	1035.2	1047.3	1060.4	1074.2	1084.1	1096.1	1105.8	1115.0	1117.9	1121.2	12
	1027	—	—	—	—	—	—	1115.9	—	1145.6	—	—	1167.8	13

CHAPTER 3
COMPRESSIONAL BEHAVIOR OF END-MEMBER AND ALUMINOUS IRON-BEARING DIOPSIDE AT HIGH PRESSURE FROM SINGLE CRYSTAL X-RAY DIFFRACTION AND FIRST PRINCIPLES CALCULATIONS

This chapter will be published as Hu, Y., Kiefer, B., Plonka, A., Parise, J., Zhang, J. S., Manghnani, M., Sahu, B. N., and Dera, P. K. Compressional behavior of end-member and aluminous iron-bearing diopside at high pressure from single crystal X-ray diffraction and first principles calculations.

3.1 Abstract

Diopside ($CaMgSi_2O_6$) the Ca- and Mg-rich clinopyroxene is an important group of minerals in the Earth's upper mantle and subducted lithospheric plate. Here, we report the results of high-pressure single-crystal X-ray diffraction experiments conducted on a natural aluminous iron-bearing diopside and a natural, nearly end-member diopside, up to 50 GPa in diamond anvil cell. Density functional theory calculation results on end-member diopside are also reported. Unit cell parameters a, b, c, β, V, as well as bond lengths of diopside are reported and compared with other clinopyroxenes. Bulk modulus and its pressure derivative of the two diopside samples are determined using third-order Birch-Murnaghan equation of state. The density of the two diopside samples are calculated under cold subducting slab conditions and are compared with the seismic models. Along the cold slab geotherm, aluminous iron-bearing diopside has higher density than end-member diopside. In the upper mantle, eclogite with aluminous iron-bearing diopside is denser than eclogite with end-member diopside, and therefore provides larger slab pulling force. At the bottom of the transition zone and the top of the lower mantle, eclogite with aluminous iron-bearing diopside, though has higher density than that with end-member diopside, is still less dense than the surrounding mantle and could contribute to the slab stagnation.

3.2 Introduction

Diopside ($CaMgSi_2O_6$), the Ca- and Mg-rich clinopyroxene (cpx) is an important mineral in the Earth's upper mantle. In the pyrolite and piclogite upper mantle models, clinopyroxene constitutes about 15% and 35%, respectively, of the total minerals in the top portion of the upper mantle [25, 27, 71, 95, 96]. As depth increases, clinopyroxene gradually dissolves into garnet and forms majorite garnet at the depth of transition zone [72].

Diopside is also an important mineral in the subducting slab. Eclogite — a rock formed by high-pressure metamorphism of basalt or gabbro at subduction zones — is mainly composed of clinopyroxene (60-70 vol%) and garnet (20-30 vol%) [1, 30], though the proxene is typically enriched in Na and Al, and classified as omphacite. When temperature is sufficiently high (e.g. >1300 K), omphacite slowly dissolves into garnet at depths greater than 300 km, transforming eclogite into garnetite [1]. This transition is highly dependent on temperature profile of the subducting slab, which varies with the age of the sea floor. Recent studies show that at temperatures well below the mantle geotherm, pyroxene-garnet transformation is kinetically inhibited at the conditions of subducting slab, so that clinopyroxene may be well preserved down to the transition zone, or even the top of the lower mantle in the subducting slab [36, 34, 33].

Seismic studies show a large variety of subducting slab morphologies near the base of the mantle transition zone, between 400 and 800 km depth. Some subducted slabs sink into the lower mantle, for example, beneath the Central America, while others seem to flatten to form stagnant slab, for example, beneath the Izu-Bonon region [19, 97]. Another notable phenonemon is that hot (>1200 K) slabs are dominated by absence of stagnancy, while cold (<1200 K) slabs are dominated by stagnancy [37]. The perservation of metastable clinopyroxenes at the transition zone provides a good explaination to the cold stagnant slab phenomenon — cold environment perserves the metastable phases which are less dense than the surrounding stable phases, thus providing buoyancy force to the slab. As a consequance, the metastability and density of pyroxene below 1200 K play an important role in slab dynamics [98, 99, 33].

Pyroxenes are also found in various chondrite meteorites including ordinary and carbonaceous chondrites, as well as in the silicate inclusions in iron meteorites [100]. Enstatite chondrites is a group of meteorites that contains a high content of enstatite, the Mg end-member pyroxene. According to the condensation series theory, iron-free fosterite (Mg_2SiO_4) appears at 1370 K, consuming most of the Mg, and later it reacts with the vapor to form enstatite ($MgSiO_3$), consuming all the remaining gaseous Si [101]. Diopside ($CaMgSi_2O_6$), the Mg, Ca-endmember clinopyroxene, condensates at a higher temperature (1450 K). The major sink for Ca at high temperature is melilite, which later disappears by reaction to form diopside and spinel. Some studies report the observation of diopside in heavily shocked chondrites [100, 102], which suggests that it can survive to pressure beyond the established stable region. Therefore, the study of diopside at high pressure is also important to explain its behavior in the shock process.

Clinopyroxenes, with a general formula $M2M1(Si, Al)_2O_6$ and a $C2/c$ space group at ambient conditions, have crystal structures consisiting of alternating layers of tetrahedral chains and layers of octahedrally coordinated cations. The flexibility of the tedrahedra to rotate with respect to one another allows the structure to accommodate cations with different ionic radii, leading to a wide range of possible compositions [40]. In this structure, M2 is usually occupied by large cations such as Ca^{2+}, Na^{+}, Mn^{2+}, Fe^{2+}, Mg^{2+} and Li^{+}; M1 is usually occupied by smaller cations such as

Mn^{2+}, Fe^{2+}, Mg^{2+}, Fe^{3+}, Al^{3+}, and Ti^{4+}. The subducted oceanic crust is rich in Fe^{2+} and Al^{3+} [1]. The downgoing sediments carried by the crust also contain Fe- and Al-rich pelitic packages [103, 24]. Thus, it is possible that Fe^{2+} and Al^{3+} present in the subducted pyroxenes. The presence of Fe^{2+} and Al^{3+} in the system has been known to affect the density of the crystals. Hedenbergite($CaFeSi_2O_6$), the Ca- and Fe-endmember clinopyroxene, has ∼12% higher density than diopside [3], while Ca-Tschermak($CaAl_2SiO_6$), the Ca- and Al-endmember clinopyroxene, has ∼5% lower density than diopside [2].

Diopside has been the subject of several high-pressure studies. The equation of state of diopside has been well determined to ∼15 GPa [3, 104, 105, 106, 107] by single-crystal or powder X-ray diffraction. Diopside is thermodynamically stable to ∼17 GPa. Above 17 GPa and 1400°C, diopside decomposes into a mixture of product phases including Mg-rich $(Mg, Ca)SiO_3$ garnet and $CaSiO_3$-rich perovskite [108, 109]. Below 1400°C, diopside dissociates to Ca-perovskite, wadsleyite and stishovite [110, 111]. Above 20 GPa, between 1000°C and 1900°C, diopside is observed to break down to Mg-perovskite and Ca-perovskite [112, 113]. At ∼1300° and 32 GPa, a metastable cubic CM-perovskite $Ca(Mg, Fe, Al)Si_2O_6$ phase was observed [114]. However, at ambient temperature, where the diffusion is slow, diopside can be preserved to pressures well above its thermodynamically stable region. The structure of diopside was determined up to ∼55 GPa on an end-member and an aluminus Fe-bearing diopside. Two new high-pressure phases, one featuring 4- and 6-coordinated Si and one featuring rare 5- and 6-coordinated Si, were observed [76, 115]. In this study, we conducted high-pressure single-crystal X-ray diffraction experiments on end-member diopside and aluminus Fe-bearing diopside. We studied the equation of state of diopside and also the compositional effect.

3.3 Methods

Two samples were used in the experiments: (1) an nearly end-member diopside $Ca(Mg_{0.97}Fe_{0.03})(Al_{0.01}Si_{1.99})O_6$ (denoted as Di_Mg_{97} below) and (2) an aluminums Fe-bearing diopside $(Ca_{0.858}Fe^{2+}_{0.098}Na_{0.030}Mn_{0.006}K_{0.003})(Mg_{0.752}Fe^{2+}_{0.153}Al_{0.064}Fe^{3+}_{0.020}Ti_{0.011})(Si_{1.936}Al_{0.064})O_6$ (denoted as Di_Mg_{75} below). Di_Mg_{97} is the same sample used in [76] and Di_Mg_{75} the same sample used in [115], Di_Mg_{75} is a natural sample from the Harry Hess collection at Princeton University (designated as sample C' in [116]).

High pressure experiments were performed at the synchrotron beamline 13ID-D of the Advanced Photon Source at Argonne National Laboratory. One Di_Mg_{97} crystal was loaded into a symmetric piston-cylinder Princeton-type diamond anvil cell (DAC) with a total opening of 54°. Neon pressure medium was loaded using the GSECARS/COMPRES gas loading system [50]. One Di_Mg_{75} crystal was loaded in helium pressure medium into a diamond anvil cell equipped with conical diamond anvils, featuring 70° total X-ray opening.

Pressure of the Di_Mg_{75} and Di_Mg_{97} was determined using ruby fluorescence [58] and neon diffraction [60], respectively. Diffraction data were collected with a MAR165 Charge Coupled De-

vice (CCD) detector at incident energy of 37.7 keV, following the same procedure as described in [66]. Diffraction images were processed using ATREX software package [64], and the structure refinements were conducted using SHELXL [86]. The refinement details of the two phases are listed in table 3.1 and table 3.2. VESTA program was used for calculation of polyhedral geometry parameters [117]. SXD data were collected at each pressure point. The principal component analysis was done using the Scikit-learn package [118].

Density functional theory (DFT) calculations were performed using the Vienna Ab-initio Simulation Package (VASP) [119, 120], with the electronic exchange and correlation described using the local-density approximations(LDA) [121]. The Brillouin zone was sampled on a 2×2×4 Monkhorst-Pack grid and a plane-wave cutoff energy of 700 eV was used. The projector augmented wave method (PAW) was used in describing the interactions between atoms [122, 119]. The core region cut-off radii of the PAW potentials for Ca, Mg, Si, and O were 3.0 a_B, 2.0 a_B, 1.6 a_B, and 1.52 a_B, respectively (1 $a_B = 0.529\mathring{A}$). These computational settings are similiar to previous work on pyroxenes [123, 124]. The DFT calculations were performed in $C2/c$ space group and all athermal structural optimizations were performed at constant volume. All crystallographic degrees of freedom consistent with the crystal symmetry were relaxed simultaneously until deviatoric stresses were less than 0.05 GPa.

3.4 Results and Discussion

3.4.1 Equation of state

The volume changes with pressure of different clinopyroxenes up to 50 GPa are plotted in figure 3.1a and a detailed comparison with existing data up to 15 GPa is shown in figure 3.1b. The volumes of diopside determined in this study show a good agreement with those from literature in the low pressure regime [3, 104, 107, 105, 106]. The differences between Di_Mg_{75}, Di_Mg_{97} and $Di_{80}En_{20}$ become larger at high pressure as shown in figure 3.1a, which could be due to either a compositional, or non-hydrostatic effect. The ambient volumes of end-member diopside ($CaMgSi_2O_6$), hedenbergite($CaFeSi_2O_6$) and Ca-Tshermak($CaAlAlSiO_6$) are 438.82(11), 449.90(7) and 421.858(22) $\mathring{A}^3$, respectively [87, 2]. The volume of diopside is $\sim$ 2.5% smaller than hedenbergite, and is $\sim$ 4.0% larger than Ca-Tshermak, which indicates that iron increases the volume, while aluminum decreases the volume in Ca-rich clinopyroxenes.

The bulk modulus (K_{T0}) and its pressure derivative (K_{T0}') can be determined from a weighted nonlinear least-squares fitting of 3rd-order Birch-Murnaghan equation of state (BM3) (Eq. 3.1):

$$P(V) = \frac{3K_{T0}}{2}[(\frac{V_0}{V})^{7/3} - (\frac{V_0}{V})^{5/3}]1 + \frac{3}{4}(K'_{T0} - 4)[(\frac{V_0}{V})^{2/3} - 1] \tag{3.1}$$

where P is pressure, V and V_0 represent the volumes at high and ambient pressure [88], $\frac{1}{\sigma(V)^2}$ is used as the weighting factor ($\sigma(V)$ is the error of volume from the experiments) and V_0 is fixed, if constrained in ambient measurement. For Di_Mg_{97}, which has no experimental V_0 value, the ambient volume is estimated to be 439.57(68) $\AA^3$ by averaging the volume of several nearly end-member diopside samples (R040009.2, R060171.2, R060276.2 from RRUFF database and the diopside sample from [87]). The BM3 fitting results of Di_Mg_{97} yield K_{T0} = 124(3) GPa and K_{T0}' = 4.4(3). The BM3 fitting of DFT calculated volumes on end-member diopside yields K_{T0} = 128(4) GPa and K_{T0}' = 4.0(2), which shows a comparable bulk modulus with Di_Mg_{97}. The discrepancies between experimental and DFT results are mainly from the neglect of thermal vibrations in the calculations. The bulk modulus and its pressure derivative of Di_Mg_{75} determined from fitting BM3 are 113(1) GPa and 4.46(9), respectively. Based on those results, we conclude that Fe and Al in diopside structure decrease the bulk modulus.

Figure 3.2 shows the F_E-f_E plot of both diopside samples, depicting a relationship between Eulerian strain f_E (Eq. 3.3) and Birch normalized stress F_E (Eq. 3.4):

$$F_E = K_{T0}[1 + 1.5f_E(K'_{T0} - 4)] \tag{3.2}$$

where

$$f_E = [(V/V_0)^{-2/3} - 1]/2 \tag{3.3}$$

and

$$F_E = P/[3f_E(1 + 2f_E)^{5/2}] \tag{3.4}$$

The K_{T0} = 112(1) GPa and K_{T0}'=4.5(1) of Di_Mg_{75} obtrained from linear f_E-F_E fit are in good agreement with the values from direct BM3 fitting (K_{T0} = 113(1) and K_{T0}' = 4.46(9)). The K_{T0} and K_{T0}' of Di_Mg_{97} from f_E-F_E plot are determined to be 123(3) GPa and 4.5(3), and agree well with the values from BM3 fitting.

The K_{T0} and K_{T0}' ellipses of different kinds of clinopyroxenes (with a confidence level of $\pm$ 68.3%) are ploted together with Di_Mg_{75} and Di_Mg_{97} in figure 3.3. The K_{T0} and K_{T0}' of Di_Mg_{75} and Di_Mg_{97} determined from fitting BM3 are similar to the observations in [106, 105, 107], but are different from the values determined by [104, 87]. The discrepancy between the data is probably due to pressure calibration or K_{T0} and K_{T0}' trade-off. Hedenbergite shows larger K_{T0} than diopside [5] and aluminous iron-bearing diopside has smaller K_{T0} than nearly end-member diopside. This indicates Fe in diopside structure tends to increase bulk modulus and Al in diopside structure tends to decreases bulk modulus. However, the variation with changes in composition is weak, which is consistent with the observation in [92].

3.4.2 Structure comparison

The lattice parameters of both diopside samples along with Hed_Fe_{83} at different pressures are shown in figure 3.4 and are tabulated in tables 3.3 and 3.4. Clinopyroxenes can be described as layered structures. The Si-O tetrahedra chains extend along the c direction with M1 and M2 cations located between the chains. a axis points to the direction that is perpendicular to the layers and therefore the length of a axis is mainly controlled by composition. Both diopside samples have similar length in the a direction, which is ∼0.8% smaller than hedenbergite, and is caused by the small cation size of Mg^{2+} compared to Fe^{2+}. This effect can also be observed in the average M1-O bondlength and $M1O_6$ polyhedral volumes as shown in figure 3.5a and figure 3.5b. The average bondlength of M1-O in hedenbergite is larger than in diopside, and the polyhedral volume of $M1O_6$ in hedenbergite is also larger than in diopside. The b unit cell parameter of hedenbergite is ∼1.1% greater than that of diopside. The unit cell length along the c direction is controlled by O3-O3-O3 angle. The O3-O3-O3 angle is almost the same in diopside and hedenbergite, in the range of ∼165°-156°. The c lattice parameter of all diopside phases compared here are about the same. The β angles of diopside decrease significantly upon compression at relatively low pressure. The Mg-rich samples Di_Mg_{97} and $Di_{80}En_{20}$ show a fattening in β angle at ∼30 GPa. The β angle of diopside are ∼1.1% higher than that of hedenbergite. Similar analyses are also found in previous literature [3].

3.4.3 Compositional effect on unit cell volume

Density is an important property of minerals which is responsible for both the positive and negative buoyancy force of the slab [31], and therefore affects the slab dynamics. The unit cell volume of minerals with different compositions can be modeled through thermodynamic mixing [125]. However, the composition of natural diopside is very complicated and thermodynamic modeling can be challenging and require a lot of data. Therefore, we used statistical methods instead of physical model to analyze the compositional effect on density in this study. In order to build the relationship between composition and unit cell volume, data from the mineral database are analyzed together with data obtained in this study, as shown in table 3.5. In this table, columns 2 to 16 (15 columns in total) show the number of atoms of different elements in each crystallographic site multiplied by 100, and the last column shows the volume. The columns 2 to 16 are used as the input (old vectors) and are decomposed to 4 new principal vectors using principal component analysis (PCA), and then multi-dimensional linear regression is used to fit the four new vectors and the volume [126].

Principal component analysis is a method to find a low-dimensional representation of the data that has the maximum variation. Each of the new dimensions found by PCA is a linear combination of

the normalized old vectors. The i^{th} vector in the new space is represented by:

$$\mathbf{Z_i} = t_{1i}\mathbf{X_1} + t_{2i}\mathbf{X_2} + ... + t_{m_1 i}\mathbf{X_{m_1}}, 0 \leq i \leq m_2 \tag{3.5}$$

where $\mathbf{X} = \{\mathbf{X_1}^T; \mathbf{X_2}^T; ...; \mathbf{X_{m_1}}^T\}$ (the superscript T means transpose) is the normalized old vector which has dimension $n \times m_1$ (n is the sample size and m_1 is the dimension of the old space), and t_{ij} is the element of the transformation matrix $\mathbf{T}$. Therefore, equation 3.5 can be represented as:

$$\mathbf{Z} = \mathbf{X} \cdot \mathbf{T} \tag{3.6}$$

The matrix $\mathbf{T}$ which maximize the variation of the new vectors can be found via eigen decomposition. The transformation matrix $\mathbf{T}$ has dimension $m_1 \times m_2$ Here, We picked 38 clinopyroxene samples as listed in table 3.5. The transformation matrix is listed in appendix A.1. The four new principal vectors forming the $\mathbf{Z} = \{\mathbf{Z_1}^T; \mathbf{Z_2}^T; \mathbf{Z_3}^T; \mathbf{Z_4}^T\}$ with dimension $n \times m_2$) are shown in appendix A.2*. [1] The four vectors in the new space explain 53.73%, 35.90%, 5.49% and 3.40%, respectively, of the total variance. The total represented variance is 98.52%, which indicates a good representation.

A linear regression is done between the 4 principal components z_1, z_2, z_3 and z_4 and the volume V, using the equation 3.7

$$V = \alpha_1 \cdot z_1 + \alpha_2 \cdot z_2 + \alpha_3 \cdot z_3 + \alpha_4 \cdot z_4 + \beta \tag{3.7}$$

The fitted coefficients are $\alpha_1 = -10.45974072$, $\alpha_2 = 10.60254801$, $\alpha_3 = -3.95525137$, $\alpha_4 = -2.44711143$ and $\beta = 440.94789474$. The mean square error of the fitting is 2.39 $(\mathring{A}^3)^2$ and the maximum mismatch between the predicted and the actual value is 1.62%. Figure 3.6 shows the linear regression results between the four new vectors and the unit cell volume. Good agreement is achieved between the fitting results and the actual values.

Elements in the transform matrix T_{ij} show the projection of the normalized vector in the old space ($\mathbf{X_i}$) on the vector in the new space ($\mathbf{Z_j}$). By analyzing $\mathbf{T}$, we can have a better idea of the principal components in this fitting. The first intersting observation in $\mathbf{T}$ is that the last two rows (the 14^{th} and the 15^{th} row) always have opposite values. The value on the 14^{th} row is the projection of Si (in T site) to the new space and the value on the 15^{th} row is the projection of Al (in T site) to the new space. Si (in T site) and Al (in T site) add up to a constant value and therefore have strong negative correlation. PCA correctly recognized the negative correlation between the two vectors and opposite numbers on the 14^{th} and the 15^{th} row can maximize the variance. Therefore, the variance contribution of Si (in T site) and Al (in T site) can be combined and analyzed together.

[1] New vectors $\mathbf{Z_i}$ even though formed through linear combination of compositional vectors, are abstract mathematical constructs without a direct chemical interpretation, because coefficents of $\mathbf{T_{ij}}$ are not restricted to be positive only.

The elements in matrix $\mathbf{T}$ range from 10^{-01} to 10^{-04}. So the most important components in the old vectors are those with coeffients T_{ij} in the order of 10^{-01}. The first new vector, $\mathbf{Z_1}$, is the most important principal component which explains 53.73% of the total variance. Among the coefficients T_{i1} (1<= i <=15), $T_{9,1}$ and $T_{15,1}$ are in the order of 10^{-01} and have a positive sign. This means that the new vector $\mathbf{Z_1}$ contribution increases as Al^{3+} (in M1 site) and Al (in T site) increase. Figure 3.6 shows the trend between $\mathbf{Z_1}$ and volume, there are roughly two branches, the branch where volume decreases as $\mathbf{Z_1}$ component increases, is mainly caused by the increase in Al^{3+} in M1 site and Al in T site. $T_{6,1}$, which is the projection of normalized Mg^{2+} concentration in M1 site on $\mathbf{Z_1}$, is the element in T_{i1} which has the largest negative value. Therefore, the $\mathbf{Z_1}$ component decreases as Mg^{2+} in M1 site increases. The other branch in figure 3.6 shows negative correlation between volume and the concentration of Mg^{2+} in M1 site. Among the coefficnets T_{i2} (1<=i<=15), $T_{7,2}$, which is the projection of Fe^{2+} in M1 site on $\mathbf{Z_2}$, has the largest positive value. In figure 3.6, unit cell volume and the the $\mathbf{Z_2}$ component are in general positively correlated. Therefore, unit cell volume and Fe^{2+} in M1 site have positive correlation. The two branches in figure 3.6 differ by Al concentration.

3.4.4 Implication to the subducting slab

Diopside is the Mg-end member of omphacite - an important clinopyroxene in eclogite, which is a rock formed by high-pressure metamorphism of basalt or gabbro in the subducted slab. It provides the pulling force for the subduction and is therefore relevant for the slab dynamic studies. The densities of different diopside and pyrope samples [31] along the cold basalt geotherm ([127]) are shown in figure 3.7. The mineral assembladges with different diopside and pyrope proportions along with two seismic density profiles are also shown in figure 3.7. Along the cold basalt geotherm, at the base of the upper mantle, Di_Mg_{75} and pyrope are ~3.5% and ~6.9% denser than Di_Mg_{97}. A mineral assemblage of 30% Di_Mg_{75} + 70% pyrope is ~2.4% denser than a mineral assemblage of 30% Di_Mg_{97} + 70% pyrope and is ~4.2% denser than the density profile determined from seismic model AK135-f and PREM. A mineral assemblage of 50% Di_Mg_{75} + 50% pyrope is ~1.7% denser than a mineral assemblage of 50% Di_Mg_{97} + 50% pyrope and is ~4.9% denser than AK135-f and PREM model. Therefore, the cold basalt provide a pulling force to the slab in the upper mantle. Di_Mg_{75}, which has more Fe and Al, provides ~2% more pulling force than the end-member diopside. Therefore, with more Fe^{2+} and Al^{3+} the slab tends to have more pulling force. At the base of the mantle transition zone, the diopside and pyrope mixtures are less dense than the density profile determined from seismology. The mineral assemblage of 30% Di_Mg_{75} + 70% pyrope is 2.6% denser than the mineral assemblage with 30% Di_Mg_{97} + 70% pyrope. This assemblage is 3.35% lighter than the seismic models. The mineral assemblage of 50% Di_Mg_{75} + 50% pyrope is 1.9% denser than the mineral assemblage with 50% Di_Mg_{97} + 50% pyrope. This assemblage is 3.0% lighter than the seismic models. At the top of the lower mantle, the 30% Di_Mg_{75} + 70%

pyrope assemblage and the 50% Di_Mg_{75} + 50% pyrope assemblage are 10.5% and 10.3% lighter than the seismic models. Therefore, even with Di_Mg_{75}, which has more Fe and Al, the cold basalt is less dense than the surrounding mantle transition zone materials. This mineral assemblage still provides a buoyancy force to the slab, and could contribute to the slab stagnation observed at the bottom of the transition zone or the top of the lower mantle.

3.5 Conclusions

Diopside ($CaMgSi_2O_6$) is an important mineral in the subuducted lithospheric plate. It is believed to dissolve into garnet at high pressure and high temperature conditions equivalent to the Earth's upper mantle. However, recent studies show that this reaction is kinetically inhibited at the conditions of cold subducting slab, and therefore clinopyroxene can be preserved down to the transition zone or even the top of the lower mantle [98, 99, 33]. We reported the results of high-pressure single-crystal X-ray diffraction experiments conducted on aluminous iron-bearing diopside and a nearly end-member diopside up to 50 GPa in diamond anvil cell. The density functional theory calculations of end-member diopside are also reported. The bulk modulus and its pressure derivative are determined to be 123(3) GPa and 4.5(3) for the nearly end-member diopside and 113(1) GPa and 4.46(9) for the aluminous iron-bearing diopside. These results are compared with hedenbergite ($CaFeSi_2O_6$) and Ca-tshermak ($CaAlAlSiO_6$), and indicate Fe in clinopyroxene structure increases bulk modulus and Al decreases bulk modulus. The structure of diopside is compared with hedenbergite and $Di_{80}En_{20}$, diopside has smaller a axis than hedenbergite and this is caused by the smaller cation size of Mg^{2+}, compared to Fe^{2+}. The β angle of Mg-rich clinopyroxene such as diopside and $Di_{80}En_{20}$ show a flattening at ~30 GPa. The effect of Fe^{2+} and Al^{3+} in the unit cell volume of Mg-, Fe- and Al-rich clinopyroxenes are analyzed using principal component analysis. Positive correlation is observed between Al and unit cell volume and negative correlation is shown between Fe and unit cell volume. The density of the two diopside samples are modeled along the cold subducting slab geotherm [127] and are compared with the seismic models. Aluminous iron-bearing diopside shows density higher than the end-member diopside. Therefore, in the upper mantle, aluminous iron-bearing diopside provides larger pulling force to the subducted slab. At the bottom of the transition zone and top of the lower mantle, eclogite with aluminous iron-bearing diopside has higher density than that with end-member diopside. However, it is still less dense than the surrounding mantle and therefore could contribute to the buoyancy force, which explains the slab stagnation phenomena observed at that depth.

3.6 Acknowledgements

The project was supported by the National Science Foundation Division of Earth Sciences Geophysics grant 1722969 to P.D. Development of the ATREX software, used for experimental data

analysis was supported by NSF EAR GeoInformatics grant 1440005. The experimental part of this work were performed at GeoSoilEnviroCARS (Sector 13), Advanced Photon Source (APS), Argonne National Laboratory. GeoSoilEnviroCARS is supported by the National Science Foundation-Earth Sciences (EAR-1128799) and Department of Energy-Geosciences (DE-FG02-94ER14466). Use of the COMPRES-GSECARS gas loading system was supported by COMPRES under NSF Cooperative Agreement EAR-1661511. Use of the Advanced Photon Source was supported by the US Department of Energy, Office of Science, Office of Basic Energy Sciences, under Contract No. DE-AC02-06CH11357. We would also like to thank Carnegie-DOE Alliance Center for support through Academic Partner subcontract to P.D. and Prof. T.S.Duffy at Princeton University for kindly providing the single crystal samples from the Harry Hess collection. B.K. would like to acknowledge computational resources that were made available by the National Science Foundation through XSEDE under grant number DMR TG-110093.

Table 3.1: Refinement results of Di_Mg_{75}

Exp. No	P0	P1	P2	P3	P4
Pressure (GPa)	0.00001	0.7(1)	2.8(1)	12.0(4)	19.9(4)
SOF of Fe, Mg	0.394(2), 0.106(2)				
Theta range (°)	1.482—18.542	1.486—18.596	1.494—18.430	1.527—18.418	1.549—18.567
No. of Reflections Collected	1391	1053	1087	1068	1037
No. of Independent Reflections	823	493	514	506	490
No. of Parameters Refined	47				
	-15≤h≤18	-14≤h≤15	-14≤h≤14	-14≤h≤13	-14≤h≤14
Limiting Indices	-13≤k≤16	-14≤k≤15	-15≤k≤15	-14≤k≤14	-13≤k≤14
	-7≤l≤7	-7≤l≤7	-7≤l≤7	-7≤l≤7	-7≤l≤7
$\mathbf{R}_{int}$	0.1078	0.1304	0.1247	0.1167	0.1046
Final R_1 and wR_2 (I>2sigma(I))	0.0589, 0.1790	0.0592,0.1340	0.0577, 0.1392	0.0566, 0.1517	0.0567, 0.1370
Final R_1 and wR_2 (all reflections)	0.0589, 0.1790	0.0592,0.1340	0.0577, 0.1392	0.0566, 0.1517	0.0571, 0.1375
Goodness of Fit	1.505	1.179	1.220	1.353	1.247
$\Delta\rho_{max}$, $\Delta\rho_{min}$ (eÅ^{-3})	3.031, -1.128	2.016, -1.187	1.699, -1.387	1.267, -1.011	1.660, -1.062
Exp. No	P5	P6	P7	P8	P9
Pressure (GPa)	25.0(4)	31.7(4)	37.7(4)	42.7(4)	48.4(4)
SOF of Fe, Mg	0.394(2), 0.106(2)				
Theta range (°)	1.564—18.409	1.582—18.547	1.595—18.598	2.367—18.548	1.620—18.442
No. of Reflections Collected	995	950	916	861	792
No. of Independent Reflections	471	445	422	403	374
No. of Parameters Refined	47				
	-13≤h≤14	-13≤h≤14	-13≤h≤14	-14≤h≤13	-14≤h≤14
Limiting Indices	-13≤k≤14	-13≤k≤13	-13≤k≤13	-13≤k≤13	-13≤k≤13
	-7≤l≤7	-7≤l≤7	-7≤l≤7	-7≤l≤7	-7≤l≤7
$\mathbf{R}_{int}$	0.091	0.0868	0.0755	0.0829	0.0866
Final R_1 and wR_2 (I>2sigma(I))	0.0549, 0.1371	0.0499, 0.1354	0.0534, 0.1930	0.0587, 0.1538	0.0621, 0.1483
Final R_1 and wR_2 (all reflections)	0.0549, 0.1371	0.0505, 0.1358	0.0544, 0.1933	0.0588, 0.1539	0.0620, 0.1483
Goodness of Fit	1.292	1.316	1.242	1.215	1.163
$\Delta\rho_{max}$, $\Delta\rho_{min}$ (eÅ^{-3})	1.136, -0.866	1.055, -0.950	1.266, -1.156	1.059, -1.123	1.017, -1.096

Table 3.2: Refinement results of Di_Mg_{97}

Exp. No	P1	P2	P3	
Pressure (GPa)	2.28(3)	9.9(4)	15.7(6)	
Theta range (°)	1.489—17.449	1.517—17.786	2.685—17.432	
No. of Reflections Collected	143	198	196	
No. of Independent Reflections	90	105	96	
No. of Parameters Refined	21			
Limiting Indices	-9≤h≤8 -8≤k≤6 -8≤l≤5	-9≤h≤10 -10≤k≤9 -8≤l≤8	-9≤h≤9 -7≤k≤8 -8≤l≤8	
$\mathbf{R}_{int}$	0.0897	0.0805	0.1002	
Final R_1 and wR_2 (I>2sigma(I))	0.0628, 0.1592	0.0601, 0.1463	0.0594, 0.1593	
Final R_1 and wR_2 (all reflections)	0.0628, 0.1592	0.0601, 0.1463	0.0594, 0.1593	
Goodness of Fit	1.239	1.167	1.209	
$\Delta\rho_{max}$, $\Delta\rho_{min}$ (eÅ^{-3})	0.604, -0.561	0.461, -0.345	0.465, -0.566	
Exp. No	P4	P5	P6	P7
Pressure (GPa)	20.9(6)	25.9(7)	34.5(3)	37.7(3)
Theta range (°)	1.547—18.085	1.558—18.192	2.744—17.320	2.753—17.380
No. of Reflections Collected	229	217	153	176
No. of Independent Reflections	109	105	78	85
No. of Parameters Refined	21			
Limiting Indices	-9≤h≤9 -8≤k≤8 -8≤l≤8	-9≤h≤9 -7≤k≤8 -8≤l≤8	-9≤h≤8 -8≤k≤8 -8≤l≤7	-8≤h≤9 -7≤k≤8 -7≤l≤8
$\mathbf{R}_{int}$	0.0975	0.0797	0.1146	0.0871
Final R_1 and wR_2 (I>2sigma(I))	0.0647, 0.1684	0.0673, 0,1635	0.0703, 0.1853	0.0781, 0.1964
Final R_1 and wR_2 (all reflections)	0.0647, 0.1684	0.0673, 0.1635	0.0703, 0.1852	0.0781, 0.1964
Goodness of Fit	1.162	1.184	1.208	1.140
$\Delta\rho_{max}$, $\Delta\rho_{min}$ (eÅ^{-3})	0.500, -0.568	0.578, -0.614	0.576, -0.556	0.620, -0.554

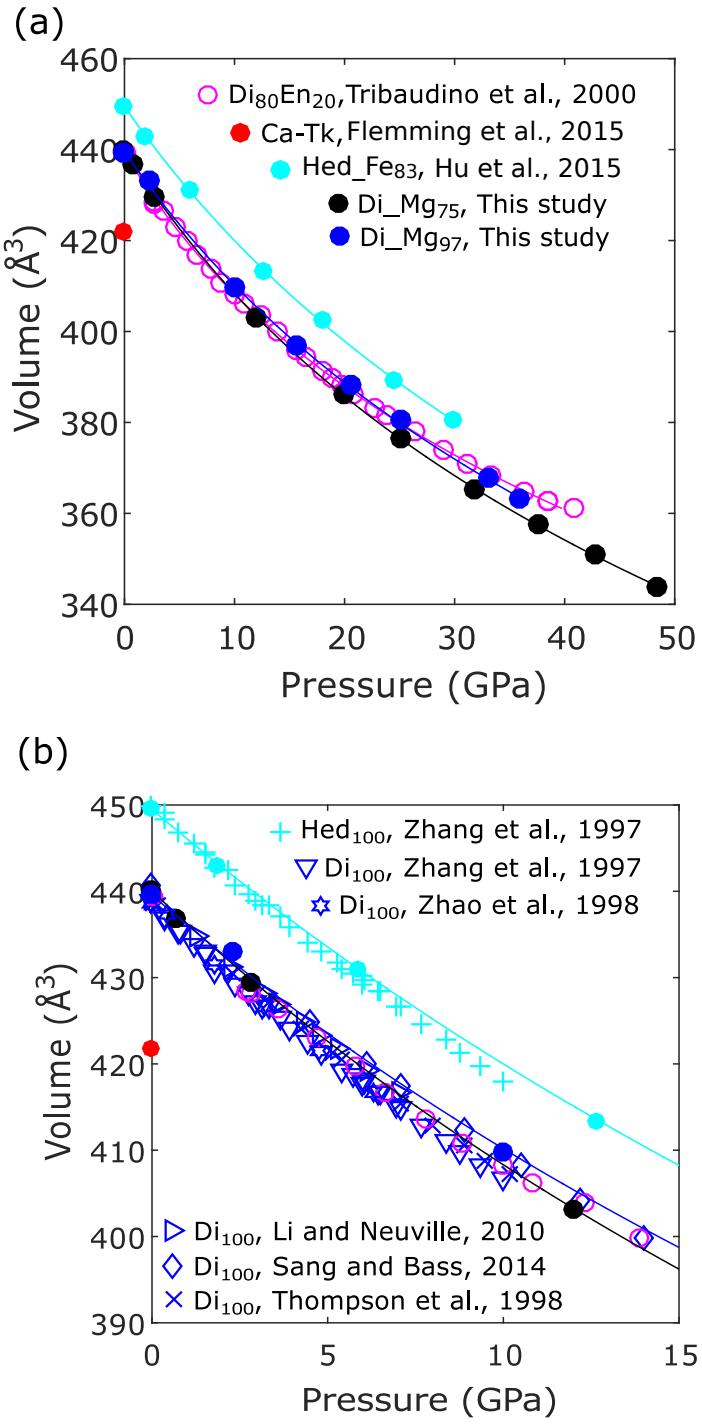

Figure 3.1: (a) The pressure—volume relationship and the equation of state fit of different clinopyroxenes up to $\sim$ 50 GPa. (b) The pressure—volume relationship and the equation of state fit of different clinopyroxenes up to 15 GPa.

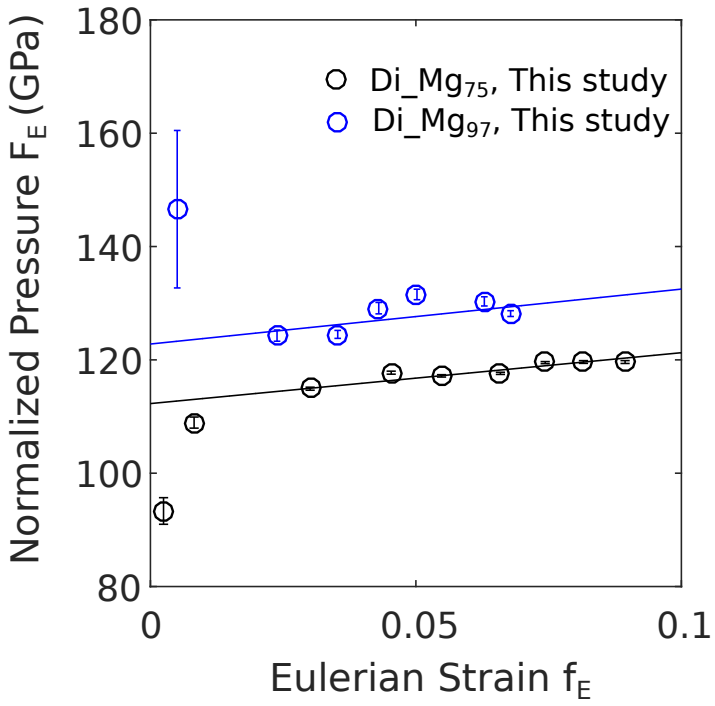

Figure 3.2: f_E—F_E plot of diopside#1 and diopside#2.

Table 3.3: Lattice parameters of Di_Mg_{75}

Exp. No.	Pressure(GPa)	a(Å)	b(Å)	c(Å)	$\beta(^\circ)$	Volume($Å^3$)
P0	0.00001	9.7578(9)	8.9168(9)	5.2584(5)	105.885(9)	440.05(8)
P1	0.7(1)	9.733(1)	8.8930(9)	5.2450(5)	105.809(9)	436.81(8)
P2	2.8(1)	9.676(1)	8.830(1)	5.2164(6)	105.52(1)	429.41(9)
P3	12.0(4)	9.500(1)	8.5954(7)	5.1066(4)	104.815(9)	403.13(7)
P4	19.9(4)	9.394(2)	8.4345(9)	5.0336(5)	104.40(1)	386.32(9)
P5	25.0(4)	9.331(1)	8.3333(9)	4.9960(5)	104.28(1)	376.46(8)
P6	31.7(4)	9.268(1)	8.2008(9)	4.9584(5)	104.14(1)	365.45(8)
P7	37.7(4)	9.238(1)	8.096(1)	4.9242(5)	103.92(1)	357.43(8)
P8	42.7(4)	9.193(2)	8.01(1)	4.9061(7)	103.70(2)	350.8(1)
P9	48.4(4)	9.181(2)	7.897(2)	4.8764(8)	103.48(2)	343.8(1)

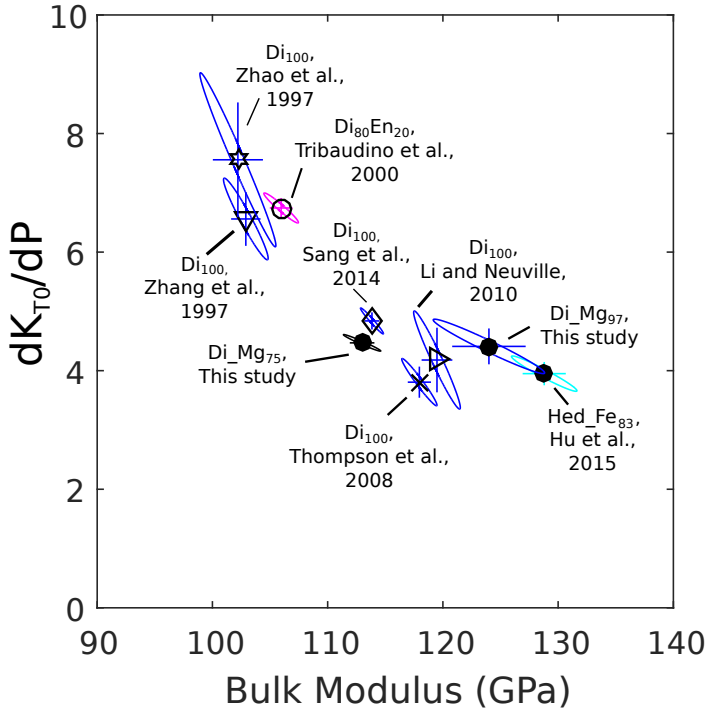

Figure 3.3: Trade-off ellipses of K_{T0} and K_{T0}' of different diopside and hedenbergite samples.

Table 3.4: Lattice parameters of Di_Mg_{97}

Exp. No.	Pressure(GPa)	a(Å)	b(Å)	c(Å)	$\beta(^\circ)$	Volume($Å^3$)
P1	2.28(3)	9.696(9)	8.882(9)	5.220(2)	105.58(3)	433.0(6)
P2	9.99(2)	9.522(4)	8.685(3)	5.1324(6)	105.03(1)	409.9(2)
P3	15.62(3)	9.463(3)	8.533(3)	5.0846(5)	104.85(1)	396.8(2)
P4	20.5(1)	9.406(6)	8.459(5)	5.050(1)	104.83(2)	388.4(3)
P5	25.2(2)	9.340(6)	8.400(5)	5.019(1)	104.73(2)	380.8(3)
P6	33.1(2)	9.273(6)	8.245(5)	4.9738(9)	104.60(2)	368.0(3)
P7	35.9(2)	9.230(3)	8.205(3)	4.9522(6)	104.45(3)	363.2(2)

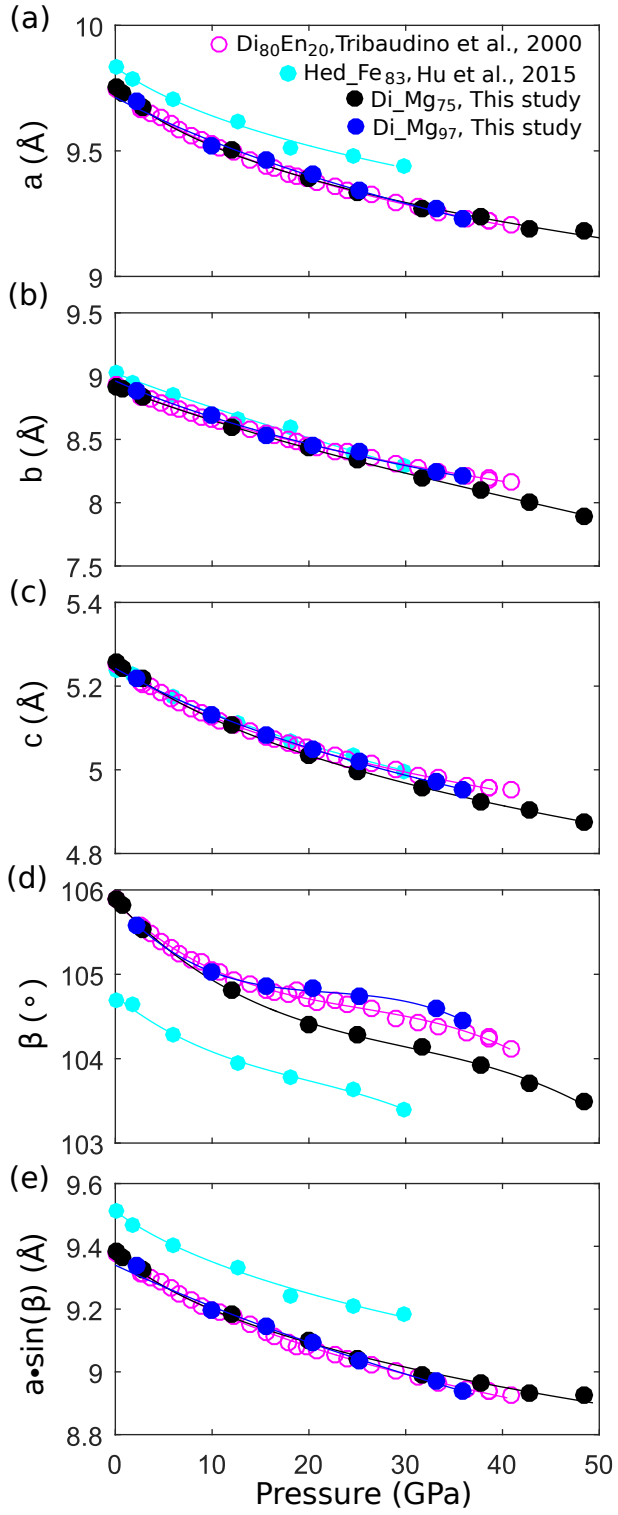

Figure 3.4: The unit cell parameters of clinopyroxenes at high pressure.

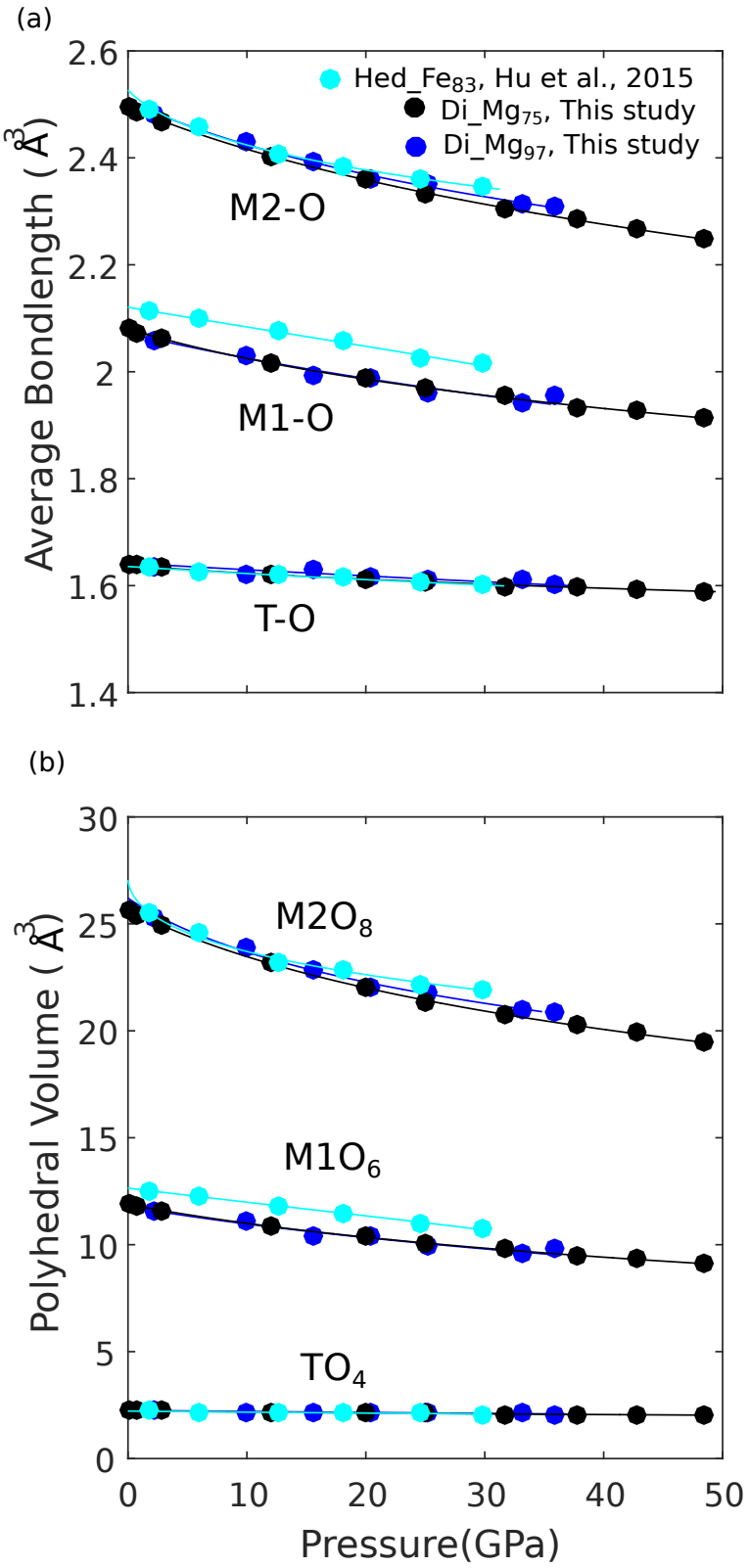

Figure 3.5: The polyhedral volumes of clinopyroxenes to high pressure.

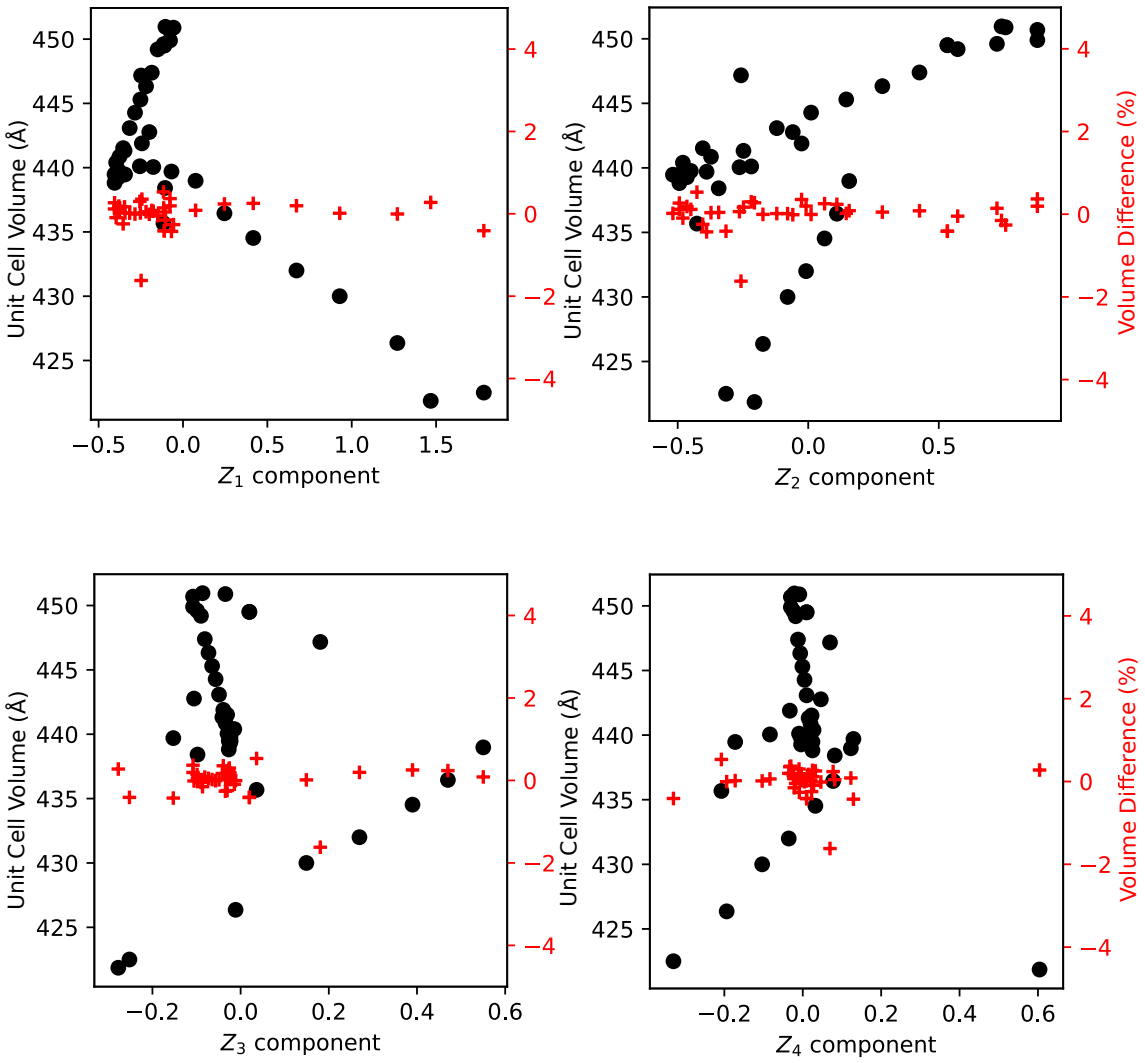

Figure 3.6: The linear regresssion between the four new principal vectors Z_i (i = 1, 2, 3, 4) and the unit cell volume.

Table 3.5: The volume of different clinopyroxenes. a: rruff.info; b: this study; c: [2]; d: [3]; e: [4]; f: [5]; g: [3]; h: [6]; i: [7].

Site	M2 site					M1 site								T site		Volume
Sample	Ca^{2+}	Fe^{2+}	Na^{+}	Mn^{2+}	Mg^{2+}	Mg^{2+}	Fe^{2+}	Fe^{3+}	Al^{3+}	$Ca^{2}+$	Ti^{4+}	Mn^{2+}	Cr^{3+}	Si	Al	
R040009.2[a]	97	2	1	0	0	97	2	0	1	0	0	0	0	200	0	439.28
R040097.2[a]	100	0	0	0	0	83	9	0	10	2	2	0	0	176	24	439.7
R050406.2[a]	95	0	5	0	0	75	18	5	1	0	1	1	0	196	4	440.11
R050496.2[a]	100	0	0	0	0	66	33	0	0	0	0	1	0	190	10	442.77
R050666.2[a]	100	0	0	0	0	66	1	0	0	0	0	33	0	200	0	447.17
R060061.2[a]	99	0	0	1	0	92	6	0	0	0	0	2	0	198	2	441.52
R060085.2[a]	97	0	3	0	0	79	10	4	4	0	2	0	1	180	20	438.42
R060171.2[a]	100	0	0	0	0	98	0	0	0	0	0	2	0	200	0	440.4
R060276.2[a]	97	0	3	0	0	96	3	0	0	0	0	0	1	200	0	439.76
R060861.2[a]	72	23	5	0	0	80	0	2	15	0	3	0	0	196	4	435.68
R070123.2[a]	95	0	4	1	0	63	33	0	4	0	0	0	0	200	0	441.89
R050030.2[a]	99.3	0	0.7	0	0	2.9	86	0	0	0	0	11.1	0	198.6	1.4	450.89
R060040[a]	100	0	0	0	0	9	89	0	0	0	0	2	0	200	0	450.96
R070236.2[a]	100	0	0	0	0	17	67	0	0	0	0	16	0	200	0	449.51
Di_Mg$_{75}$[b]	86	10	3	1	0	75	15	2	7	0	1	0	0	194	6	440.05
Ca-Tk[c]	100	0	0	0	0	0	0	0	100	0	0	0	0	100	100	421.86
Di$_{100}$[d]	100	0	0	0	0	100	0	0	0	0	0	0	0	200	0	438.82
Di$_{80}$En$_{20}$[e]	80	0	0	0	20	100	0	0	0	0	0	0	0	200	0	439.47
Hed_Fe$_{67}$[f]	100	0	0	0	0	17	67	0	0	0	0	16	0	200	0	449.5
Hed$_{100}$[g]	100	0	0	0	0	0	100	0	0	0	0	0	0	200	0	449.9
Di$_{100}$Hd$_{0}$[h]	100	0	0	0	0	100	0	0	0	0	0	0	0	200	0	439.48
Di$_{91}$Hd$_{9}$[h]	100	0	0	0	0	91.16	8.84	0	0	0	0	0	0	200	0	440.86
Di$_{82}$Hd$_{18}$[h]	100	0	0	0	0	82.09	17.91	0	0	0	0	0	0	200	0	441.32
Di$_{72}$Hd$_{28}$[h]	100	0	0	0	0	72.78	27.22	0	0	0	0	0	0	200	0	443.08
Di$_{63}$Hd$_{37}$[h]	100	0	0	0	0	63.21	36.79	0	0	0	0	0	0	200	0	444.28
Di$_{53}$Hd$_{47}$[h]	100	0	0	0	0	53.39	46.61	0	0	0	0	0	0	200	0	445.3
Di$_{43}$Hd$_{57}$[h]	100	0	0	0	0	43.30	56.70	0	0	0	0	0	0	200	0	446.33
Di$_{32}$Hd$_{68}$[h]	100	0	0	0	0	32.93	67.07	0	0	0	0	0	0	200	0	447.39
Di$_{22}$Hd$_{78}$[h]	100	0	0	0	0	22.26	77.74	0	0	0	0	0	0	200	0	449.2
Di$_{11}$Hd$_{89}$[h]	100	0	0	0	0	11.29	88.71	0	0	0	0	0	0	200	0	449.61
Di$_{0}$Hd$_{100}$[h]	100	0	0	0	0	0	100	0	0	0	0	0	0	200	0	450.69
Di$_{100}$Ca-Tk$_{0}$[i]	100	0	0	0	0	0	0	0	0	0	0	0	0	200	0	438.98
Di$_{90}$Ca-Tk$_{10}$[i]	90	0	0	0	0	0	0	0	10	0	0	0	0	190	10	436.45
Di$_{80}$Ca-Tk$_{20}$[i]	80	0	0	0	0	0	0	0	20	0	0	0	0	180	20	434.53
Di$_{65}$Ca-Tk$_{35}$[i]	65	0	0	0	0	0	0	0	35	0	0	0	0	165	35	432
Di$_{50}$Ca-Tk$_{50}$[i]	50	0	0	0	0	0	0	0	50	0	0	0	0	150	50	430
Di$_{30}$Ca-Tk$_{70}$[i]	30	0	0	0	0	0	0	0	70	0	0	0	0	130	70	426.36
Di$_{0}$Ca-Tk$_{100}$[i]	0	0	0	0	0	0	0	0	100	0	0	0	0	100	100	422.5

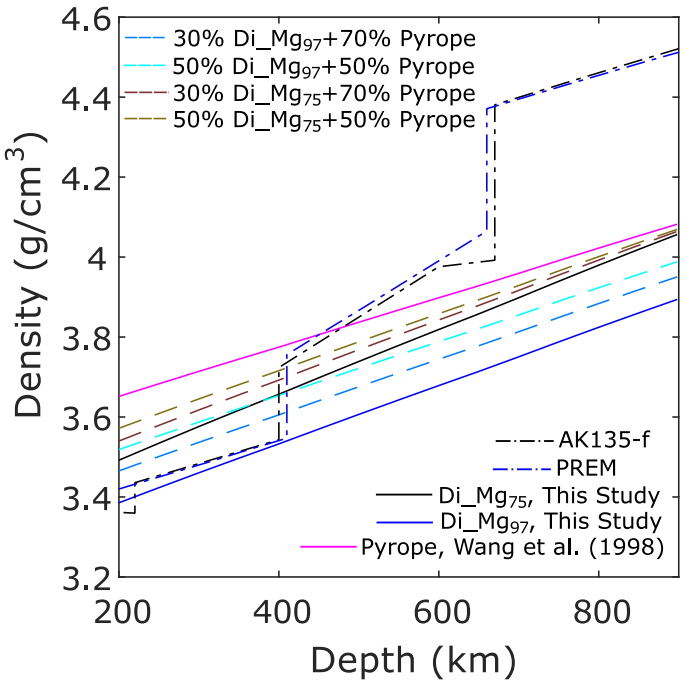

Figure 3.7: The density of different mineral assemblages in the cold subducting slab

CHAPTER 4
HIGH-PRESSURE GAMMA-DIOPSIDE: DOES PENTA-COORDINATED SILICON EXIST IN THE EARTH'S MANTLE?

This chapter has been published as Hu, Y., Kiefer, B., Bina, C. R., Zhang, D., and Dera, P. K. (2017). HighPressure γ-$CaMgSi_2O_6$: Does PentaCoordinated Silicon Exist in the Earth's Mantle?. Geophysical Research Letters, 44(22).

4.1 Abstract

In situ X-ray diffraction experiments with natural Fe- and Al- bearing diopside single crystals and density functional theory (DFT) calculations on diopside end-member composition indicate the existence of a new high-pressure γ-diopside polymorph with rare penta-coordinated silicon. On compression α-diopside transforms to the γ-phase at $\sim$ 50 GPa, which in turn, on decompression is observed to convert to the known β-phase below 47 GPa. The new γ-diopside polymorph constitutes another recent example of penta-coordinated silicon (^{V}Si) in over-compressed metastable crystalline silicates, suggesting that ^{V}Si may exist in the transition zone and the uppermost lower mantle in appreciable quantities, not only in silicate glass and melts, but also in crystalline phases contained in the coldest parts of subducted stagnant slabs. ^{V}Si may have significant influences on buoyancy, wave velocity anomalies, deformation mechanisms, chemical reactivity of silicate rocks and seismicity within the slab.

4.2 Introduction

The Earth's mantle is primarily composed of silicates. The pressure-induced transformations of the silicate minerals strongly affect the physical properties of the Earth's mantle and therefore controls geological processes such as tectonics and deep-focus earthquakes. Si strongly prefers four-coordinated crystallographic sites due to sp^3 hybridization. As a consequence, in silicate minerals characteristic of the crust and the upper mantle, silicon resides predominantly in tetrahedral sites coordinated by four oxygen atoms (^{IV}Si). This low coordination number and mesodesmic bonds, found e.g. in quartz, pyroxene and olivine, result in significant structural flexibility for forming extended silicate chains, sheets, and framework polyhedral motifs, and accounts for the majority of the mineral diversity observed in terrestrial rocks of shallow origin. Silicon is also capable of forming hypervalent, 5- and 6- coordinated states (^{V}Si and ^{VI}Si). These hypervalent states are favored at high pressures and with increased ligand electronegativity. As a result, at greater depths of the Earth's interior, silicon strongly prefers sites with six nearest neighbor ligands arranged

in octahedral geometry, leading to more compact, higher density phases such as SiO_2 stishovite, (Mg,Fe)SiO_3 bridgmanite or $MgSiO_3$ akimotoite. Densification of silicates, involving a coordination number increase from four (^{IV}Si) to six (^{VI}Si) accounts for the density stratification of the Earth's mantle, and is responsible for the 660-km seismic discontinuity.

There has been great interest in understanding the occurrence and function of the penta-coordinated Si phases (^{V}Si) both in solid state chemistry and Earth science. Stereochemical analysis of crystal structures reported to contain [SiL_5] groups (where L represents ligand such as C, N, F or Cl) in crystals with hexagonal close-packed arrays of ligands indicates that there is an almost continuous change from an [SiL_4] tetrahedron to an [SiL_5] trigonal bipyramid, and that the penta-coordinated state indeed plays a critical role as intermediate in condensation and decondensation reactions of silicates in aqueous solutions and in melts [128]. Amorphous solids and melts can sustain exotic coordination environments such as SiO_5 more easily than crystalline silicates due to the lack of symmetry and long-range order. Indeed, several studies of glass and melts clearly indicate existence of penta-coordinated silicon at elevated pressures, which can sometimes persist in quenched samples. It is also believed that penta-coordinated silicon plays an important role in dissolution of silica and change of deformation mechanism [129]. Crystalline silicate minerals with ^{V}Si are rare, but have been reported previously in the literature based on both experiments and calculations and are suggested as important intermediate phases in phase transformation and chemical reaction processes. For example, a quenchable phase with five-coordinated Si was observed in $CaSi_2O_5$ silicate, which can be synthesized at 1500 °C and 10 GPa [18]. A non-quenchable high-pressure polymorph of enstatite [12] and a high-pressure phase of danburite [130] observed in single crystal X-ray diffraction experiments also featured ^{V}Si. Molecular dynamics calculations predicted that ^{V}Si coordination should form in SiO_2 α-quartz under uniaxial stress at high pressure [13]. High-pressure states involving ^{V}Si are also reported to act as intermediates during the ^{IV}Si to ^{VI}Si transition in molecular dynamics simulations on α-quartz [131] and orthoenstatite [132].

Pyroxenes are the second most abundant mineral group in the Earth's upper mantle and represent a major mineral component in subducted slabs, which are composed of upper mantle rocks (residual harzburgite and lherzolite), containing up to 30% pyroxene [71], and basaltic crust layer, where the pyroxene content may be as high as 70% [133]. Diopside ($CaMgSi_2O_6$), the Mg,Ca-endmember clinopyroxene (cpx), is abundant in both the upper mantle and the subducted lithosphere [133]. At ambient conditions, diopside crystallizes in C2/c space group and is thermodynamically stable up to $\sim$ 18 GPa. Above this pressure and 1400 °C diopside decomposes into a mixture of product phases including $CaSiO_3$-rich perovskite and Mg-rich (Mg,Ca)SiO_3 tetragonal garnet. Below 1400 °C, diopside dissociates to Ca-perovskite + wadsleyite+stishovite [108, 109, 110, 111]. At pressures above 20 GPa, between 1000 °C and 1900 °C, diopside is observed to break down to Mg-perovskite and Ca-perovskite [112, 113]. Subsequently, a metastable cubic CM-perovskite Ca(Mg,Fe,Al)Si_2O_6 phase was observed to form at $\sim$ 1300 °C and 32 GPa and was also observed in diopside glass at $\sim$

1000 °C and 13 GPa as a metastable phase. At 1800 °C, CM-perovskite was observed to decompose into cubic Ca-perovskite and orthorhombic Mg-perovskite and stishovite [114, 110].

In the more chemically and petrologically complex upper mantle and transition zone where temperature is high (> 1400 °C), pyroxene is believed to gradually dissolve into garnet and form majorite around depths corresponding to the transition zone [71]. However, the mantle transition zone is not homogeneous in temperature and chemical composition. Seismic tomography observations show that some cold subducted slabs in the west Pacific regions stagnate at the bottom of transition zone or the uppermost lower mantle [19, 97]. Geodynamic models estimate the temperature in the stagnant slabs are lower than 900 °C and can be as low as 500 °C in regions such as Tonga [127, 37]. It has been reported that, in cold environment (< 1400 °C), the diffusion between pyrope and majorite garnet is slow, making the preservation of the light metastable pyroxene possible, which changes the density of the slab and therefore affects its morphology and buoyancy [36, 134, 99, 34, 33, 135, 37, 98]. As a consequence, the metastability of pyroxene and the kinetics of post-pyroxene transformations below 1000 °C have been suggested to play an important role in the slab dynamics [99, 33, 98].

High-pressure ambient-temperature experiments not only pave the road to high-pressure moderate-temperature (500 °C < T < 1000 °C) experiments, but also create conditions to trap the metastable intermediate phases which can provide important transition path information for future kinetic studies. On compression at ambient temperature, diopside can be metastably preserved to pressures as high as 50 GPa [136, 107], above which it transforms to β-phase with mixed 4 and 6 coordinated silicon [76]. A similar structure was also observed in clinoferrosillite $FeSiO_3$ at high pressure [137]. Other clinopyroxenes were also observed to be preserved to at least 30 GPa at ambient temperature [5, 138, 139]. Natural diopside typically contains appreciable amounts of iron, and the objective of this study is to examine the effect of iron on the post-pyroxene transformation in natural samples along the diopside-hedenbergite join. In this study, we combined in situ single crystal synchrotron X-ray diffraction experiments on a natural iron-bearing diopside sample with density-functional-theory (DFT) calculations, to better understand the formation of exotic hypervalent silicon states in pyroxenes.

4.3 Methods

The sample used for synchrotron experiments was a natural Fe- and Al-bearing diopside from the Harry Hess collection at Princeton University. The chemical composition of this sample (designated as sample C' in [116]) is $(Ca_{0.86}Fe^{2+}_{0.10}Na_{0.03}Mn_{0.01})$ $(Mg_{0.75}Fe^{2+}_{0.15}Al_{0.07}Fe^{3+}_{0.02}Ti_{0.01})(Si_{1.94}Al_{0.06})O_6$. The site occupancies are assigned according to [140]. Single crystal X-ray diffraction (SXD) experiments were conducted at ambient pressure using Bruker D8 Venture diffractometer with AgKα microfocus source and PHOTON-II detector at the University of Hawaii and 13-BM-C of the Advanced Photon Source at Argonne National Laboratory. The high pressure experiments were done

at the synchrotron beamline 13-ID-D of the Advanced Photon Source at Argonne National Laboratory. High quality ambient pressure single crystal refinement results with anisotropic displacement parameters for all atoms were is reasonable agreement with the microprobe results reported in [116]. Refined cation disorder model included substitution of Mg^{2+} and Fe^{2+} on the M1 site, and yielded a refined approximate composition of $CaFe^{2+}_{0.212}Mg_{0.788}Si_{2.00}O_6$, which was used as starting composition in high pressure refinements.

One natural Fe- and Al-bearing diopside crystal was loaded in helium pressure medium into a diamond anvil cell equipped with conical diamond anvils, featuring 70° total X-ray opening. Pressure was determined using ruby fluorescence method [58]. Diffraction data were collected with a MAR165 Charge Coupled Device (CCD) detector at incident energy of 37.7 keV, following the same procedure as described in [5]. Diffraction images were processed using ATREX software package [64], and the structure refinements were conducted using SHELXL [86]. Despite the fact that the quality of the single crystal specimen became significantly worse after the transition due to defects arising from coexistence of the two phases over a range of pressure of ∼5 GPa, the crystallographic analysis of the high-pressure phase was still possible, revealing details of unit cell changes, symmetry, atomic arrangement and bonding. Anisotropic displacement factors are used for all atoms in α-diopside and isotropic displacement factors are used for all atoms in high-pressure β- and γ-diopside. The refinement details and atomic coordination of the different phases are listed in tables 4.1, 4.2, 4.3 and 4.4. VESTA program was used for calculation of polyhedral geometry parameters [117]. The samples were compressed from ambient pressure to 57.1(1) GPa in approximately 5 GPa steps, and then decompressed to 47.0(1) GPa. SXD data were collected at each pressure point. Diffraction patterns of α-diopside and γ-diopside are shown in supplementary figures S1a and S1b, respectively.

3-dimensional periodic density functional theory (DFT) calculations were performed using VASP (Vienna Ab-initio Simulation Package) [119, 120]. The electronic exchange and correlation effects were described in the LDA approximation [121]. The interactions between atoms were described within the PAW method [122, 119]. The results of this approach have been shown to be of comparable accuracy to all electron calculations [141, 120]. The core region cut-off radii (1 a_B = 0.529 Å) of the PAW potentials were 3.0 a_B (core configuration $3p^6 4s^2$), 2.0 a_B (core configuration $2p^6 3s^2$), 1.6 a_B (core configuration $3s^2 3p^2$), and 1.52 a_B ($2s^2 2p^2$) for Ca, Mg, Si, and O, respectively. The Brillouin zone was sampled on a 2×2×4 Monkhorst-Pack grid and a plane-wave cutoff energy E_{cut}=700 eV was applied. These computational settings are similar to previous work on pyroxenes [123, 124]. The DFT calculations were performed in the known space groups of diopside C2/c (low pressure) and $P2_1/c$ (high pressure). All athermal structural optimizations were performed at constant volume. All crystallographic degrees of freedom consistent with the crystal symmetry (unit cell shape and atomic positions) were relaxed simultaneously until deviatoric stresses were less than 0.05 GPa).

4.4 Results

At ambient conditions, in the α-phase, diopside has a C2/c space group and retains this symmetry to at least 48.4(1) GPa, when compressed at ambient temperature (table 4.1). The α-phase is characterized by a monoclinic angle of $\sim 105^\circ$ and all Si in tetrahedral coordination. Upon further compression, the Fe- and Al-bearing diopside undergoes a phase change to a $P2_1/c$ γ-phase with a decrease in volume and a change in monoclinic angle to $\sim 98^\circ$ at $\sim$ 55.1(1) GPa (figure 4.1, table 4.1). Our refinements reveal a structure with a mixture of ^{V}Si and ^{VI}Si polyhedral layers. Unlike the case of experiments with end-member diopside, which transformed from α- to β- phase, converting a single tetrahedral ^{IV}Si site into a 1:1 mixture of ^{IV}Si and ^{VI}Si [76], compression of the natural diopside sample results in a change to the coordination number of both Si sites in the $P2_1/c$ structure, producing hypervalent 5- and 6- coordinated polyhedra. Whereas this discrepancy could be attributed to the different chemical composition, it is also possible that the previous experiments simply did not reach high enough pressure to reveal the γ-phase in the end-member. Upon decreasing pressure, the γ-phase is preserved to $\sim$ 51 GPa. At $\sim$ 47 GPa, γ-diopside undergoes an isosymmetric phase transition to the $P2_1/c$ β-phase with monoclinic angle changing to $\sim 96^\circ$ (Table S1). The transition pressure from C2/c phase to $P2_1/c$ phase is very close to what was observed in previous shock experiments, which reported a thermomechanical phase transformation at $\sim$ 50 GPa [142]. Our experiments were complemented by a series of first-principles computations, to explore the origin of the exotic ^{V}Si coordination further. The unit cell parameters of the three phases obtained from both experiments and calculations are shown in figure 4.1 and figure 4.6. The enthalpy calculated by density functional theory indicates that the $P2_1/c$ structure becomes energetically favorable over C2/c structure from $\sim$ 30 GPa and the 5-, 6- coordinated $P2_1/c$ transition takes place above $\sim$ 38 GPa, which corresponds to the pressure of the uppermost lower mantle (figure 4.7). Once locked in the 5-coordinated configuration, diopside can remain in this structure without transforming to six-coordinated structure to $\sim$ 150 GPa. The discrepancy between experimentally-observed and computationally-determined transition pressures can be attributed to kinetic effects, as well as absence of thermal contributions in the computations. In the DFT calculations we also found two other structural variants - one with $^{IV,VI}Si^{4+}$ in $P2_1/c$ space group and one with $^{V,V}Si^{4+}$ in C2/c space group, which do not manifest themselves in nature.

Based on experimental observations, we propose a model explaining how α-diopside transforms to the β- and γ-phases. C2/c α-diopside is described by corner-sharing SiO_4 tetrahedral chains that extend along the c-axis. Between these Si-O chains, Ca^{2+} and Mg^{2+}/Fe^{2+} cations are placed for charge neutrality. The I-beam representation of building blocks of the pyroxene structure conveniently shows that each octahedral layer is intimately connected to two silicate chain layers on either side by sharing oxygen atoms (figure 4.8(a)). In the C2/c α-diopside phase, there is only one unique Si site (table **??**). The Si atoms in different layers are related by a (1/2, 1/2, 0) translation symmetry (C-centering). After the C2/c to $P2_1/c$ phase transformation, the C-centering is lost,

producing two symmetry-independent Si-O layers (table 4.3 and 4.4). As a consequence, there are two unique sites for Si cations (Si1 and Si2) in the $P2_1/c$ phase, residing in two different layers. We denote Si-O layer with Si1 as layer 1, while the layer containing Si2 is denoted as layer 2 (figure 4.8(b)). The same transformation also applies to the O anions - the three different O sites in C2/c phase split into six unique O sites in the $P2_1/c$ phase. In the $P2_1/c$ structure the oxygen atoms occupy general positions and therefore possess a degree of translational freedom to respond to changes in applied pressure, which is absent in C2/c symmetry.

At low temperatures, the kinetic energy available for atomic rearrangements accompanying structural transitions is limited, and as a result, displacive phase transformations are favored. As pressure increases, the Si-O layers become more condensed and the Si-O chains start to interconnect, as shown in figure 4.2. In layer1, the conversion involves two steps: a shift of the Si-O chains and rotation of the Si-O tetrahedra, which result in the formation of six- coordinated silicon (figure 4.2). Si#0-O2#2 and Si#0-O1#1 distance in C2/c phase are denoted by blue and black dash lines in figure 4.2(a) and markers with the same color in figure 4.9. Both distances decrease gradually as pressure increases and new bonds form after the phase transformation. In the $P2_1/c$ phases, Si#0 becomes Sia#1 while O2#2 and O1#0 become O2a#0 and O1a#0, respectively. Sia#1 connects with O2a#0 (the blue bond) and O1a#0 (the black bond), forming edge-sharing Si-O octahedral layers with ^{VI}Si (figure 4.2(c) and 4.2(e)). These new bonds cause the oxygen layers shift, and the O-O-O (θ) angle change from $\sim 150^\circ$ to 200° (table 4.9) (θ is labeled in figure 4.2). As can be seen from figures 4.2(c) and (e), one chain of O atoms shifts by approximately c/2, along the c axis and the SiO_4 polyhedra rotate by $\sim 50^\circ$ (θ angle). In layer 2, Si#3-O2#5 and Si#3-O1#6 in C2/c phase are denoted by blue and black dash lines in figure 4.2(b). Both distances first decrease, and then increase as pressure increases within C2/c phase. This behavior makes it difficult for Si and O to approach close enough to form a bond. After the C2/c-$P2_1/c$ phase transformation, Si#3 turns into Sib#3 while O2#5 and O1#6 turn into O2b#5 and O1b#6. Both distances decrease dramatically, but only Sib#3-O1b#5 becomes a bond (figures 4.9(b), 4.2(d) and 4.2(f)). The fifth Si-O interatomic distance in γ-diopside phase has a length of $\sim$ 1.9 Å. At 55.1(1) GPa, electron density map is calculated by DFT and a bond path can be seen (figure 4.10), confirming the attractive character of this interatomic interaction. A similar structure with 4+1 coordinated Si is also observed in post-enstatite [12]. The fact that pyroxenes go through penta-coordinated structures suggests such structure could be a common intermediate between the 4- to 6-coordinated transformations in pyroxenes. The bond-forming characteristics of the phase transformation between α- and γ-diopside suggest exothermic reaction which is one of the criteria for phase transformations that could be responsible for deep-focus earthquakes [143].

The dominating coordination state of Si in the Earth's upper mantle and transition zone is ^{IV}Si, whereas in the lower mantle it changes to ^{VI}Si [27]. This change in coordination number and geometry of SiO_N (N = 4, 5, 6) units is determined by different electron orbital hybridization types. The

tetrahedral geometry of SiO_4 group (figure 4.11(a)) is caused by sp^3 hybridization of the Si orbitals, while the octahedral geometry of SiO_6 group (figure 4.11(c)) is a result of sp^3d^2 hybridization [144]. Most of the penta-coordinated silicate structures reported to date have approximately square pyramid configuration with bond lengths ranging from ~ 1.6 to ~ 1.9 Å, averaging ~ 1.7 Å, as shown in figures 4.11(d)-(f) [18, 13, 12]. Geometrically, these structures suggest the sp^3d^2 hybridization with a lone electron pair. However, the SiO_5 group in this study shows a trigonal bipyramid structure with four bond lengths ranging from 1.60(2) to 1.67(2) Å and the fifth bond length of 1.95(2) Å which suggests a sp^3d hybridization (figure 4.11(b)) [144]. Theoretical studies also suggest that hypervalent Si compounds feature three-center-four-electron (3c-4e) electron-deficient bond. This predicts elongated Si-O bond length along the axial direction, as observed in the current study. Previous reports demonstrate that the Si-O bond could be as long as 1.954 Å and 1.918 Å in organic compounds due to the weak bonding character of the 3c-4e bonds [145]. Hypervalent compounds exhibit high Lewis acidity because the electron density on the central atom decreases with increasing coordination. For example, methanium (CH^{5+}), which can be explained by the electron-deficient 3c-2e chemical bond, is a superacid [146, 147]. The occurrence of ^{V}Si in chemical compounds has been reported to result in greatly increased chemical activity [145], therefore, the presence of ^{V}Si in γ-diopside and other metastable hypervalent mantle silicate phases could be expected to alter chemical reactions taking place during melting and mantle convection.

The coordination number of Si in both amorphous/liquid and crystalline silica/silicates increases with increasing pressure (figure 4.3). In basalt and diopside melt, this increase is continuous and the ^{IV}Si - ^{VI}Si jump takes place between 20 and 50 GPa, which roughly corresponds to the transition zone and top of the lower mantle [27]. Si coordination changes in enstatite [12] and silica [13] indicate very similar behavior, with densification starting at lower mantle pressures. In this study, the average coordination number of crystalline diopside reaches 5 (4+6) in the β-phase around 40 GPa, and increases to 5.5 (5+6) in the γ-phase around 50 GPa; however, this pressure is likely to decrease at elevated temperature. The Si coordination number in melts and glasses is known to affect the rheological behavior because of the formation and breakdown of bonds [129]. It can also be expected to affect the properties of crystalline material in similar ways. Diopside is brittle and exhibits good natural cleavage on {110}, with intersects at 87° and 93° due to the weak bonding between Si-O tetrahedral chains, as shown in figure 4.8(a). Both the β and γ hypervalent-Si diopside phases show structures in between pyroxene and ilmenite, and the fact that the Si-O tetrahedral chains become connected will modify fracture toughness, because ilmenite structure does not have natural cleavage. Slip systems, which control the lattice preferred orientation of clinopyroxenes have been reported to be {110}1/2<110>, {110}[001] and (100)[001] [148]. The new bonds in $P2_1/c$ phases which form in {110} planes will most likely reduce the mobility on the original {110} planes, and therefore may change lattice preferred orientation. The presence of SiO_5 defects was also recently suggested to play a critical role in the brittle to ductile transition in densified silica

glass by facilitating shear deformation and in dissipating energy by converting back to the 4-fold coordination state during deformation [129]. If ^{V}Si is also present in crystalline silicates, the condensed silicate layers may have a similar effect on the rheology of the mantle rocks.

Slabs have been detected to be stagnant at the mantle transition zone depth, especially in cold and old subducted slabs in the west Pacific regions where the estimated temperatures at 660 km are below 1000 °C [19, 97, 37]. The preservation of light metastable phases such as olivine to compensate the effect of low temperature thus providing buoyancy force is one of the proposed mechanisms [149, 150, 151, 152, 153, 154]. It has been suggested that the pyroxene-garnet transformation can be kinetically sluggish in cold environments, and thus pyroxene may be preserved in subduction zones at least to the top of the lower mantle [34, 33]. Recent geodynamic modeling has demonstrated that metastable pyroxene has a stronger potential for affecting slab buoyancy at the transition zone than metastable olivine, though has not yet accounted for the post-pyroxene transformation involving Si coordination changes [135, 37].

The preservation of pyroxene and post-pyroxene phases changes the density and elastic properties of the slab, and therefore affects morphology and seismic wave velocity profile. In the present study, structural data for the high-pressure polymorphs were obtained for only a few pressure points, thus we could not properly constrain changes in the equation of state from experiments alone. Instead, we analyzed the DFT results on the end-member composition to estimate the changes in compressibility and volume discontinuities, and compared our results with the calculated results of several important minerals in the transition zone and lower mantle (figure 4.4(a)). The volumes calculated by DFT are usually $\sim$ 3% smaller than experimental results because of neglecting vibrational contributions [155, 31]; however, the relative values give good approximations. The calculated bulk modulus from third order Birch-Murnaghan equation of state for the α-phase was 128(4) GPa, with K_0'=4.0(2) and V_0=422.1(6) Å^3. The transformation to β-diopside increases the bulk modulus to K_0=159(6) GPa, K_0'=3.6(3) and V_0=396.5(7) Å^3, and results in a 4.3% density increase. The γ-phase, is characterized by K_0=170(5) GPa, K_0'=3.87(8) and V_0=386(1) Å^3, and is accompanied by 1.5 % density increases. The densities of both β- and γ-phases lie in the bracket determined by shock experiments (3.6-3.9 g/cm^3) [142, 156], it is therefore possible that the phase transformation reported in the shock experiment corresponds to formation of one of the metastable high-pressure phases observed in our study. The temperature in previous shock experiments was estimated to reach $\sim$ 1200 °C, which indicates that this phase could exist at $\sim$ 1200 °C and $\sim$ 90 GPa. The bulk moduli and bulk velocity ($v = \sqrt{K_T/\rho}$) of different phases are also calculated as a function of pressure (figures 4.4(b) and (c)). The new β- and γ- diopside are stiffer than α-diopside and have higher bulk sound velocity. However, in comparison, bridgmanite (Mg-Pv), Ca-perovskite (Ca-Pv) and akimotoite (Akm) have much higher bulk modulus and bulk sound velocity than the α-, β- and γ-diopside. The γ-diopside is $\sim$ 6% and $\sim$ 11% lighter than $MgSiO_3$ akimotoite [16] and $CaSiO_3$+$MgSiO_3$ perovskite mixture [15, 14], which would promote stagnation of the cold slab in

the transition zone or the uppermost part of the lower mantle [97]. In terms of elastic anisotropy, we expect both the β- and γ- phases to resemble diopside and akimotoite, which are highly anisotropic [106], consistent with seismic observation in the cold stagnant slab [157, 158].

4.5 Conclusions

The fate of clinopyroxenes like diopside in the Earth's mantle is to break down into dense oxides or densify into perovskite phases, with separation of Ca-rich and Ca-poor components. Petrologists previously assumed that this process requires complete breakdown of the crystal structure and involves a fully reconstructive transformation mechanism, with extensive bond breaking and reformation, and thus requires high temperature to overcome kinetic barriers. The results reported above demonstrate that there exists an alternative path to accomplish the silica densification, which involves a displacive, reversible mechanism and a phase with exotic, penta-coordinated silicon. This general mechanism seems to be accessible to most pyroxenes belonging to the En-Fs-Hd-Di quadrilateral, for both clinopyroxene and orthopyroxene compositions, and it sems to always involve phases with penta-coordinated Si. The presence of ^{V}Si has consequences for chemical reactivity, elastic and plastic deformation, density of the subducted slab and its buoyancy relative to the surrounding mantle. In old and cold subducted slabs in the west Pacific region, high pressure and moderate temperature conditions along the slab may support such a transformation mechanism and promote metastable existence of β- and γ-diopside far outside of their thermodynamic stability fields in the lower mantle.

4.6 Acknowledgments

The project was supported by the National Science Foundation Division of Earth Sciences Geophysics grant 1344942 to P.D. Development of the ATREX software, used for experimental data analysis was supported by NSF EAR GeoInformatics grant 1440005. Portions of the X-ray diffraction work were conducted using X-ray Atlas instrument at the University of Hawaii, funded by NSF EAR Instrumentation and Facilities grant 1541516. Portions of this work were performed at GeoSoilEnviroCARS (Sector 13), Partnership for Extreme Crystallography program (PX^2), Advanced Photon Source (APS), Argonne National Laboratory. GeoSoilEnviroCARS is supported by the National Science Foundation-Earth Sciences (EAR-1128799) and Department of Energy-Geosciences (DE-FG02-94ER14466). PX^2 program is supported by COMPRES under NSF Cooperative Agreement EAR-1661511. Use of the COMPRES-GSECARS gas loading system was supported by COMPRES under NSF Cooperative Agreement EAR-1661511. Use of the Advanced Photon Source was supported by the US Department of Energy, Office of Science, Office of Basic Energy Sciences, under Contract No. DE-AC02-06CH11357. We would also like to thank Carnegie-DOE Alliance Center for support through Academic Partner subcontract to P.D. and Prof. T.S.

Duffy at Princeton University for kindly providing the single crystal samples from the Harry Hess collection. B.K. would like to acknowledge computational resources that were made available by the National Science Foundation through XSEDE under grant number DMR TG-110093. We would also like to thank the two anonymous reviewers for their insightful advice and Dr. Jeroen Ritsema for handling this paper. Additional data are included in supporting information.

Table 4.1: Experimental and refinement details of three different diopside phases

	$\alpha-$diopside	**γ-diopside**	**β-diopside**
Pressure (GPa)	P9 = 48.4(1)	P11 = 55.1(1)	P14 = 47.0(1)
Space Group	C2/c	$P2_1/c$	$P2_1/c$
	9.181(2)	9.279(4)	9.138(3)
Lattice Parameters (Å)	7.897(2)	7.566(2)	7.648(2)
	4.8764(8)	4.628(1)	4.6998(9)
β angel (°)	103.48(2)	98.35(3)	96.42(2)
Volume (Å^3)	343.8(1)	321.5(2)	326.3(1)
Si Coordination	4	5 and 6	4 and 6
θ range for data collection	1.620-18.442	2.442-17.914	1.638-18.121
No. of Reflections Collected	792	795	655
No. of Independent Reflections	374	397	365
No. of Parameters Refined	47	41	41
	-14≤h≤14	-12≤h≤13	-12≤h≤11
Limiting Indices	-13≤k≤13	-12≤k≤10	-11≤k≤11
	-7≤l≤7	-6≤l≤6	-6≤l≤6
R_{int}	0.886	0.2239	0.1511
Final R_1 and wR_2 (I>2sigma(I))	0.0621, 0.1483	0.1449, 0.3499	0.1634, 0.3969
Final R_1 and wR_2 (all reflections)	0.0620, 0.1483	0.1496, 0.3527	0.1661, 0.3990
Goodness of Fit	1.163	1.072	1.090
$\Delta\rho_{max}$, $\Delta\rho_{min}$ (eÅ^{-3})	1.017, -1.096	2.616, -1.983	3.862, -3.177

Table 4.2: Atomic position in α-diopside

Pressure (GPa)	P9 = 48.1(1)					
	x	**y**	**z**	**SOF**	**U(eq)×10^3 (Å^2)**	**Wyckoff**
Ca	0	0.3155(2)	0.25	0.5	10(1)	4e
Mg, Fe	0	0.9109(2)	0.25	0.394(2), 0.106(2)	8(1)	4e
Si	0.7842(2)	0.6010(2)	0.2413(4)	1	8(1)	8f
O1	0.6114(5)	0.5961(4)	0.136(1)	1	11(1)	8f
O2	0.8516(5)	0.7755(5)	0.350(1)	1	12(1)	8f
O3	0.8588(5)	0.5326(5)	-0.0075(9)	1	10(1)	8f

Table 4.3: Atomic position in γ-diopside

Pressure (GPa)	P11 = 55.1(1)					
	x	**y**	**z**	**SOF**	**U(eq)×10^3 (Å^2)**	**Wyckoff**
Ca	0.7433(5)	0.0798(6)	0.118(1)	1	10(1)	4e
Mg, Fe	0.2454(8)	0.1628(8)	0.389(1)	0.788(5), 0.212(5)	12(1)	4e
Sia	0.5088(8)	0.1676(8)	0.459(2)	1	10(1)	4e
Sib	0.0138(8)	0.8565(7)	0.193(1)	1	8(1)	4e
O1a	0.391(2)	0.165(2)	0.116(4)	1	8(3)	4e
O1b	0.144(2)	0.354(2)	0.207(4)	1	11(3)	4e
O2a	0.394(2)	0.483(2)	0.080(4)	1	12(3)	4e
O2b	0.093(2)	0.042(2)	0.163(4)	1	17(3)	4e
O3a	0.611(2)	0.296(2)	0.277(4)	1	12(3)	4e
O3b	0.103(2)	0.713(2)	0.013(4)	1	18(4)	4e

Table 4.4: Atomic position in β-diopside

Pressure (GPa)	P14 = 47.0(1)					
	x	**y**	**z**	**SOF**	**U(eq)×10^3 (Å^2)**	**Wyckoff**
Ca	0.7388(5)	0.0711(6)	0.0961(9)	1	8(1)	4e
Mg, Fe	0.2433(9)	0.1646(9)	0.401(2)	0.788(5), 0.212(5)	12(2)	4e
Sia	0.5086(8)	0.1668(8)	0.462(1)	1	7(1)	4e
Sib	0.0253(9)	0.8566(9)	0.251(2)	1	10(1)	4e
O1a	0.388(2)	0.163(2)	0.118(3)	1	4(3)	4e
O1b	0.145(2)	0.351(2)	0.223(3)	1	9(3)	4e
O2a	0.390(2)	0.484(3)	0.101(4)	1	15(4)	4e
O2b	0.102(2)	0.034(2)	0.189(3)	1	7(3)	4e
O3a	0.611(2)	0.295(2)	0.275(4)	1	11(3)	4e
O3b	0.106(2)	0.709(2)	0.065(3)	1	8(3)	4e

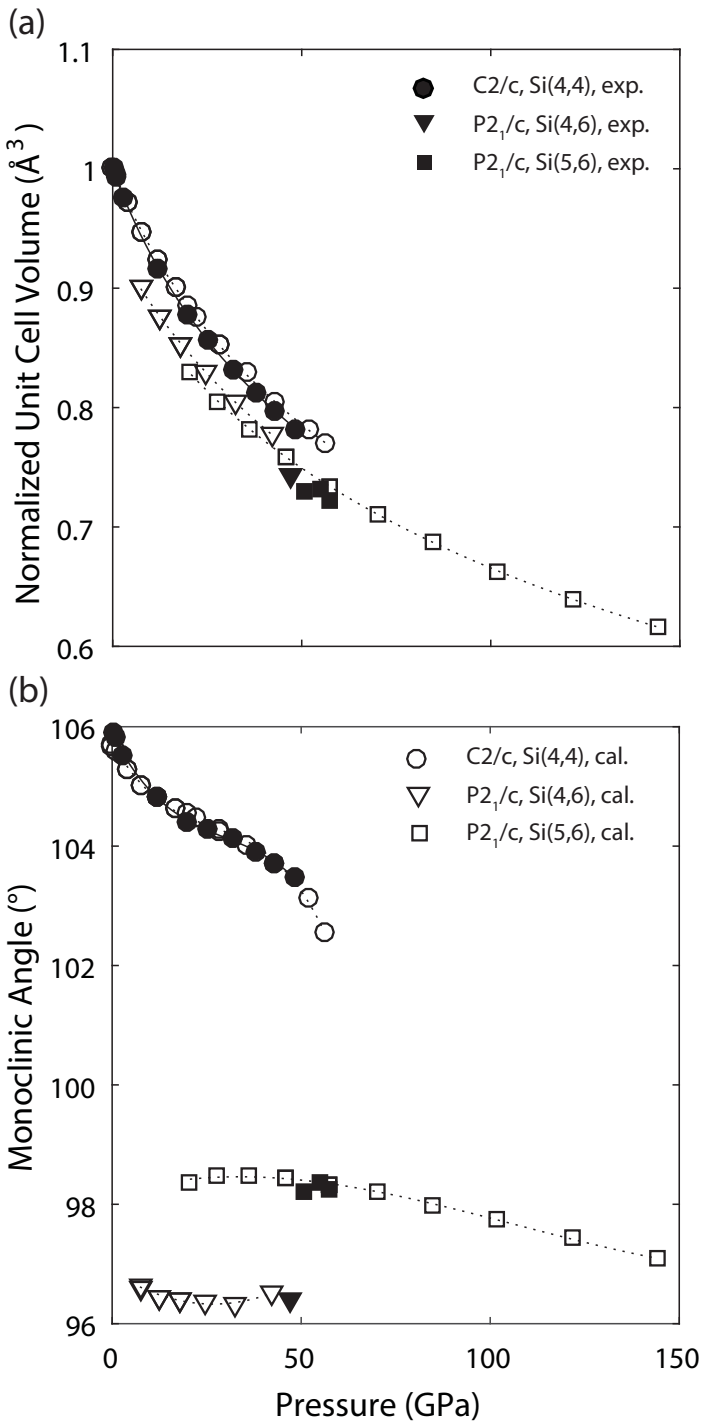

Figure 4.1: (a) Normalized unit cell volume of different diopside phases with respective to V_0 of α-diopside. Solid line is the third-order Birch-Murnagham equation of state fit of the XRD experimental data and dotted lines are the third-order Birch-Murnagham equation of state fit of the DFT calculation results. (b) Monoclinic angles of different diopside phases. C2/c Si(4, 4) α-diopside (circles), P2$_1$/c Si(4, 6) β-diopside (down-pointing triangles) and P2$_1$/c Si(5, 6) γ-diopside phases (squares) at high pressure. Filled symbols are from XRD experiments on Fe- and Al-bearing diopside (errors are smaller than the markers) and open symbols are from DFT calculations on Di_{100}.

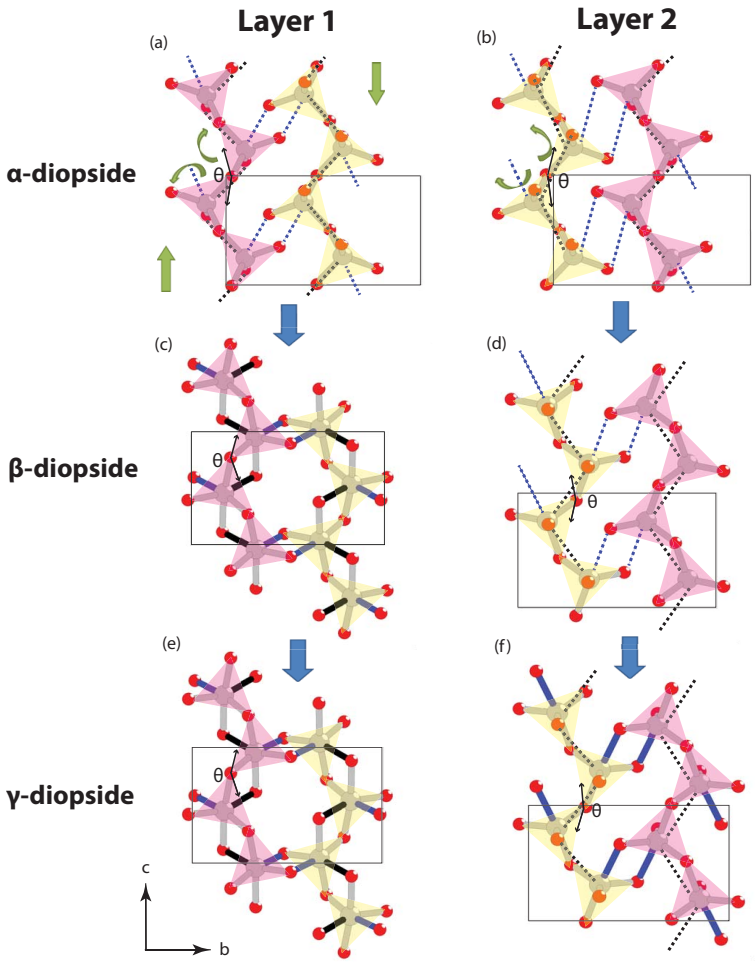

Figure 4.2: (a) Layer 1 of C2/c α-diopside phase with $^{IV}Si^{4+}$. θ is the O3-O3-O3 angle. Green arrows show the Si-O chain rotation and translation. (b) Layer 2 of C2/c α-diopside phase with $^{IV}Si^{4+}$. θ is the O3-O3-O3 angle. (c) Layer 1 of $P2_1/c$ β-diopside phase with $^{VI}Si^{4+}$. θ is the O3a-O3a-O3a angle. (d) Layer 2 of $P2_1/c$ β-diopside phase with $^{IV}Si^{4+}$. θ is the O3b-O3b-O3b angle. (e) Layer 1 of $P2_1/c$ γ-diopside phase with $^{VI}Si^{4+}$. θ is the O3a-O3a-O3a angle. (f) Layer 2 of $P2_1/c$ γ-diopside phase with $^{V}Si^{4+}$. θ is the O3b-O3b-O3b angle. Si and O atoms are represented by grey and red respectively. Solid black rectangular box is the unit cell. Same color denotes the same Si-O distance in different figures. Magenta solid triangle facets represent O-O-O planes above Si atoms and green solid triangles facets represent O-O-O planes above Si atoms. Si-O distances and polyhedral parameters are listed in table **??**.

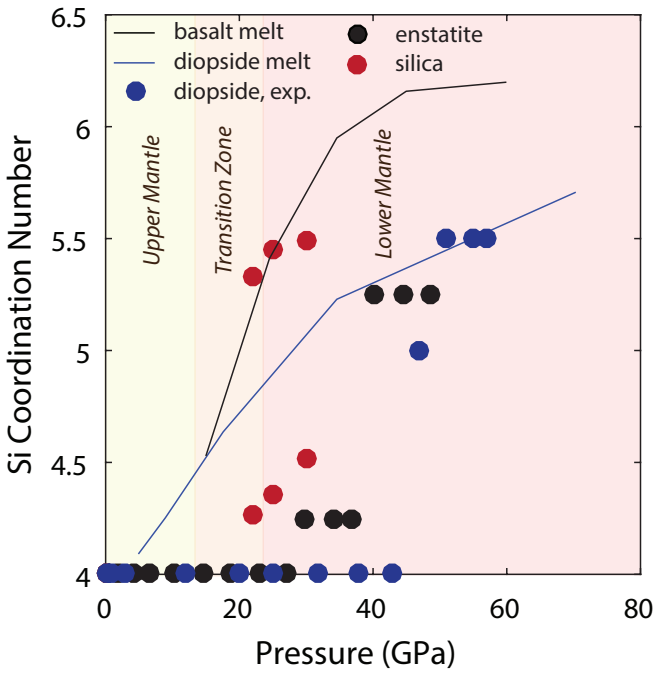

Figure 4.3: Si coordination number of basalt melt (black line) [10], diopside melt (blue line) [11], enstatite (black circle) [12], silica (magenta circle) [13] and diopside (this study) (blue circle). The different colors of background indicate the upper mantle (yellow), the transition zone (orange) and the lower mantle (red) regions.

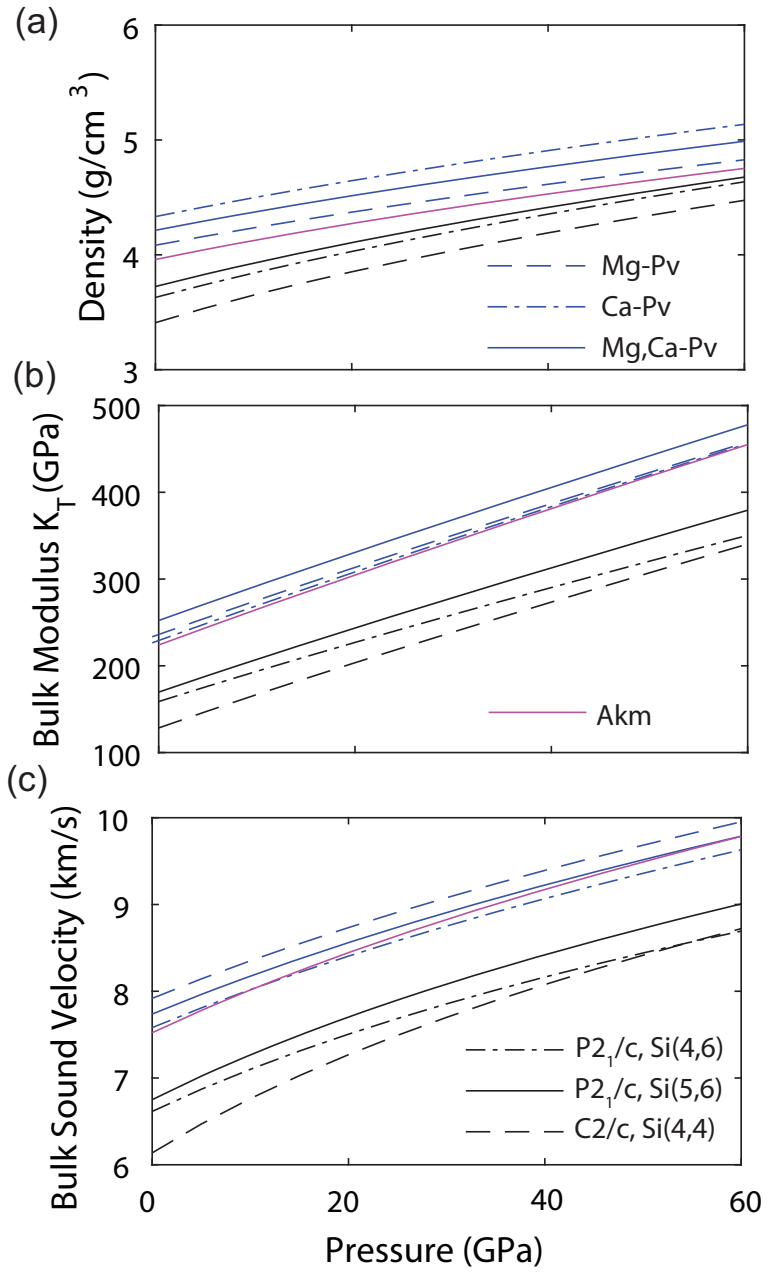

Figure 4.4: Density (a), bulk modulus (b) and bulk sound velocities (c) of different mineral phases calculated by DFT. Mg-perovskite data is from [14]. Ca-perovskite data is from [15]. Mg, Ca perovskite data is from simple linear interpolation of Mg perovskite and Ca perovskite. Mg ilmenite data is from [16]. $P2_1/c$ Si(4,6), $P2_1/c$ Si(5,6) and C2/c Si(4,4) are from our DFT calculation results.

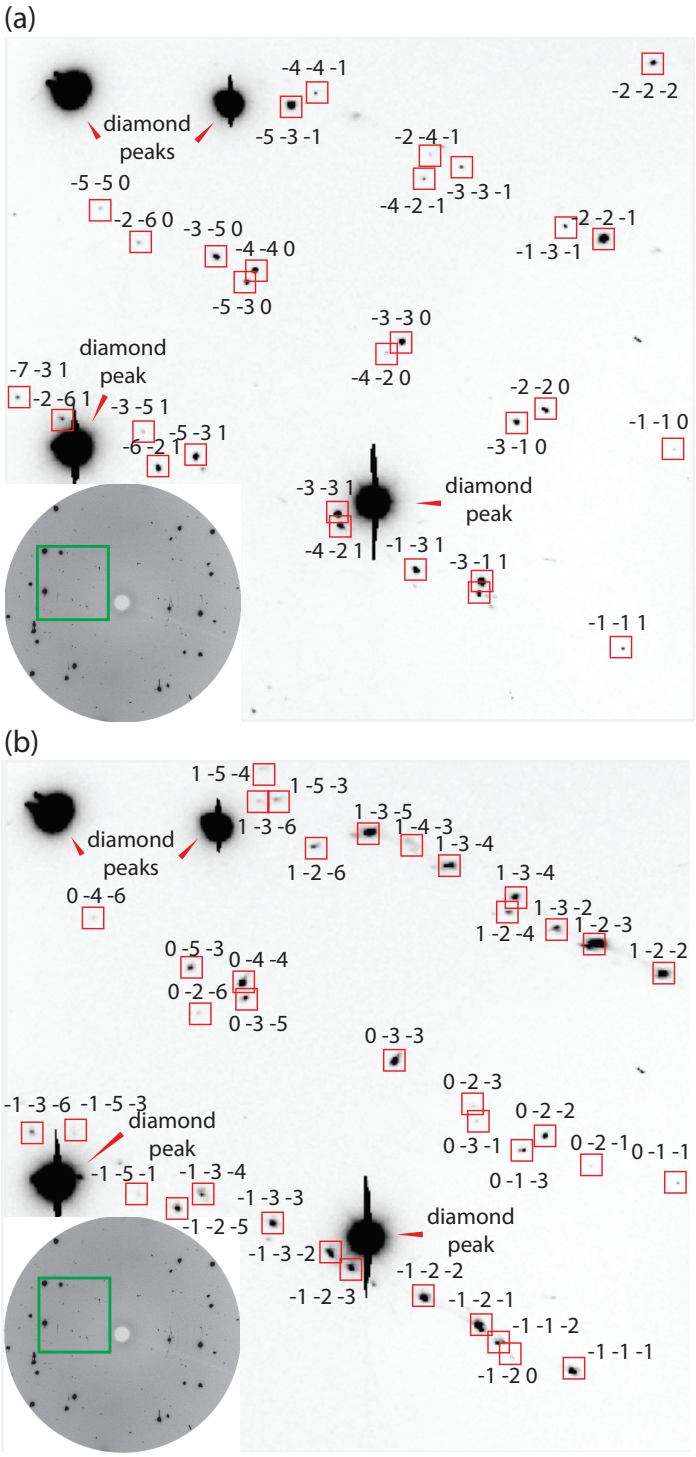

Figure 4.5: Single crystal X-ray diffraction patterns of α-diopside at (a) P9=48.4(1) GPa and (b) γ-diopside at P11=55.1(1) GPa.

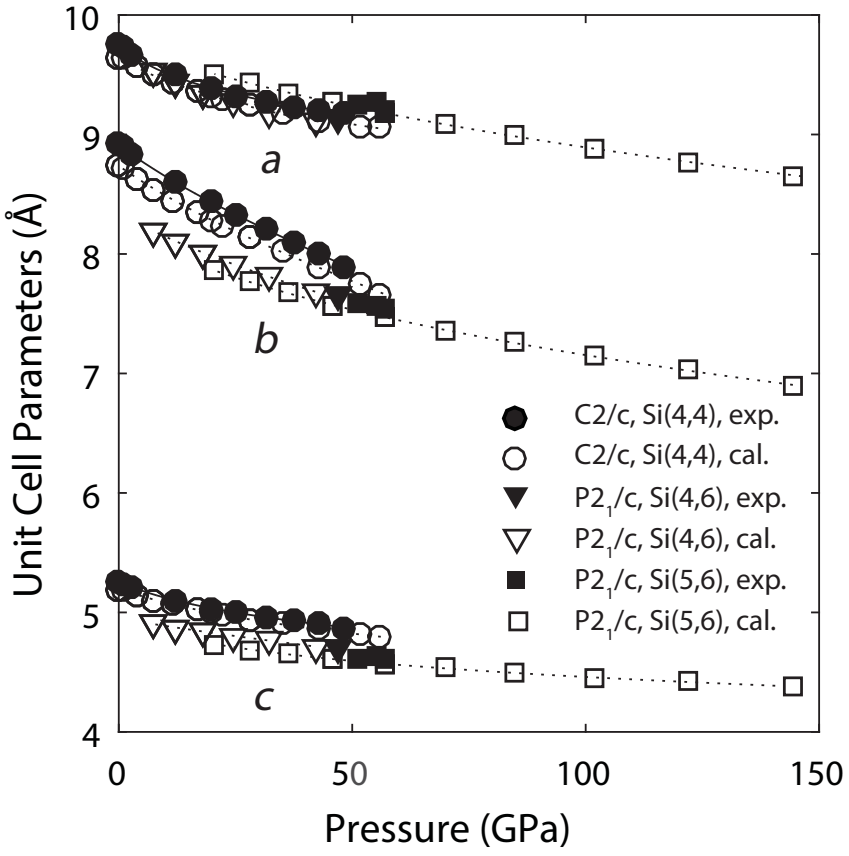

Figure 4.6: Unit cell parameters of C2/c Si(4, 4) α-diopside (*circles*), P2$_1$/c Si(4, 6) β-diopside (*down−pointing triangles*) and P2$_1$/c Si(5, 6) γ-diopside phases (*squares*) at high pressure. Filled symbols are from XRD experiments (errors are smaller than the markers) and unfilled symbols are from DFT calculations.

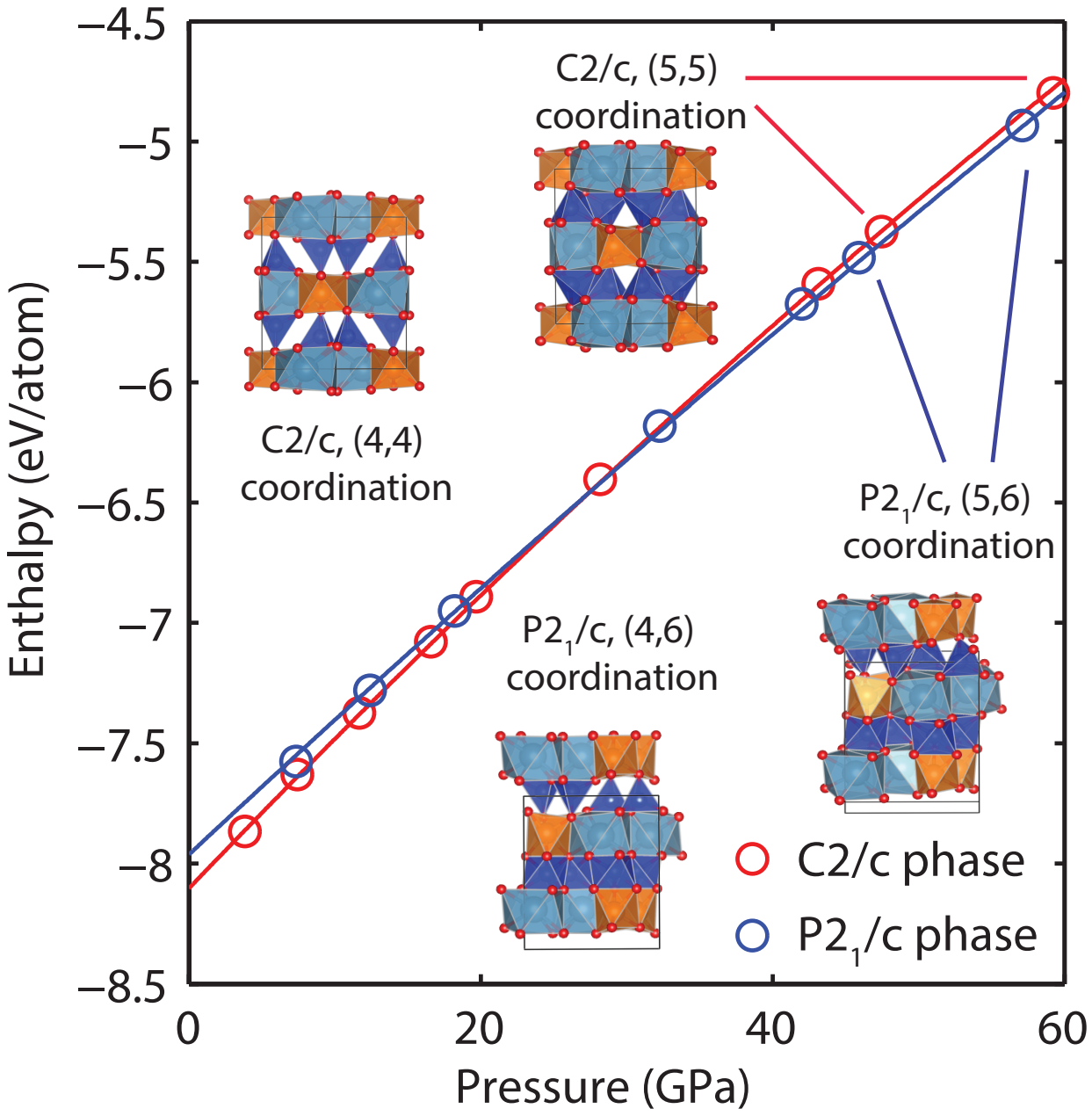

Figure 4.7: Enthalpy of different phases calculated by density functional theory. Structures in the figure are viewed along c axis.

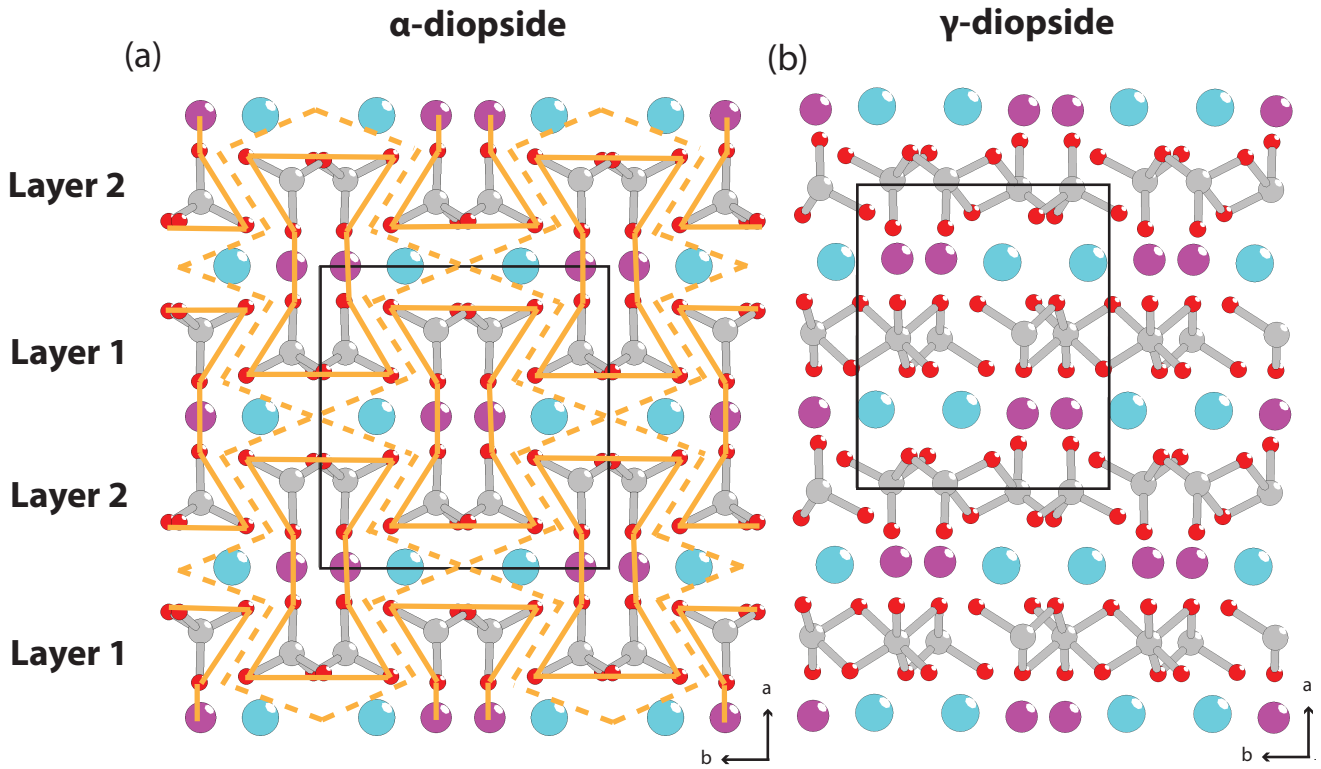

Figure 4.8: Diopside viewed along c axis. Si, O, Ca and Mg/Fe atoms are denoted by grey, red, cyan and magenta respectively. Only Si-O bonds are shown. Solid black rectangular box is the unit cell. (a) C2/c α-diopside. The I-shape beams formed by two Si-O tetrahedral chains are denoted by orange outlines. Dash orange lines denote the cleavage plane. (b) $P2_1/c$ γ-diopside.

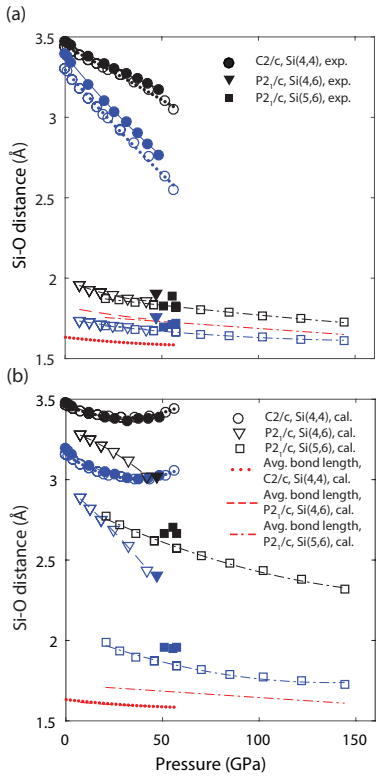

Figure 4.9: (a) Si-O distance in layer 1 of C2/c Si(4, 4) α-diopside (circles and dotted lines), P2$_1$/c Si(4, 6) β-diopside (down-pointing triangles and dashed lines) and P2$_1$/c Si(5, 6) γ-diopside phases (squares and dash-dot lines) at high pressure. Blue color refers to Si#0-O2#2 in C2/c phase (Sia#1-O2a#0 in P2$_1$/c phase) and black color refers to Si#0-O1#1 in C2/c phase (Sia#1-O1a#0 in P2$_1$/c phase). Red color refers to the average bond length in layer 1. Filled symbols are from XRD experiments (errors are smaller than the markers) and unfilled symbols are from DFT calculations. (b) Si-O distance in layer 2 of C2/c Si(4, 4) α-diopside (circles and dotted lines), P2$_1$/c Si(4, 6) β-diopside (down-pointing triangles and dash lines) and P2$_1$/c Si(5, 6) γ-diopside phases (squares and dash-dot lines) at high pressure. Blue refers to Si#3-O2#5 in C2/c (Sib#3-O2b#5 in P2$_1$/c phase) and black refers to Si#3-O1#6 in C2/c phase (Sib#3-O1b#5 in P2$_1$/c phase). Red refers to the average bond length in layer 1. Filled symbols are from XRD experiments on Fe- and Al-bearing diopside (errors are smaller than the markers) and unfilled symbols are from DFT calculations on Di$_{100}$.

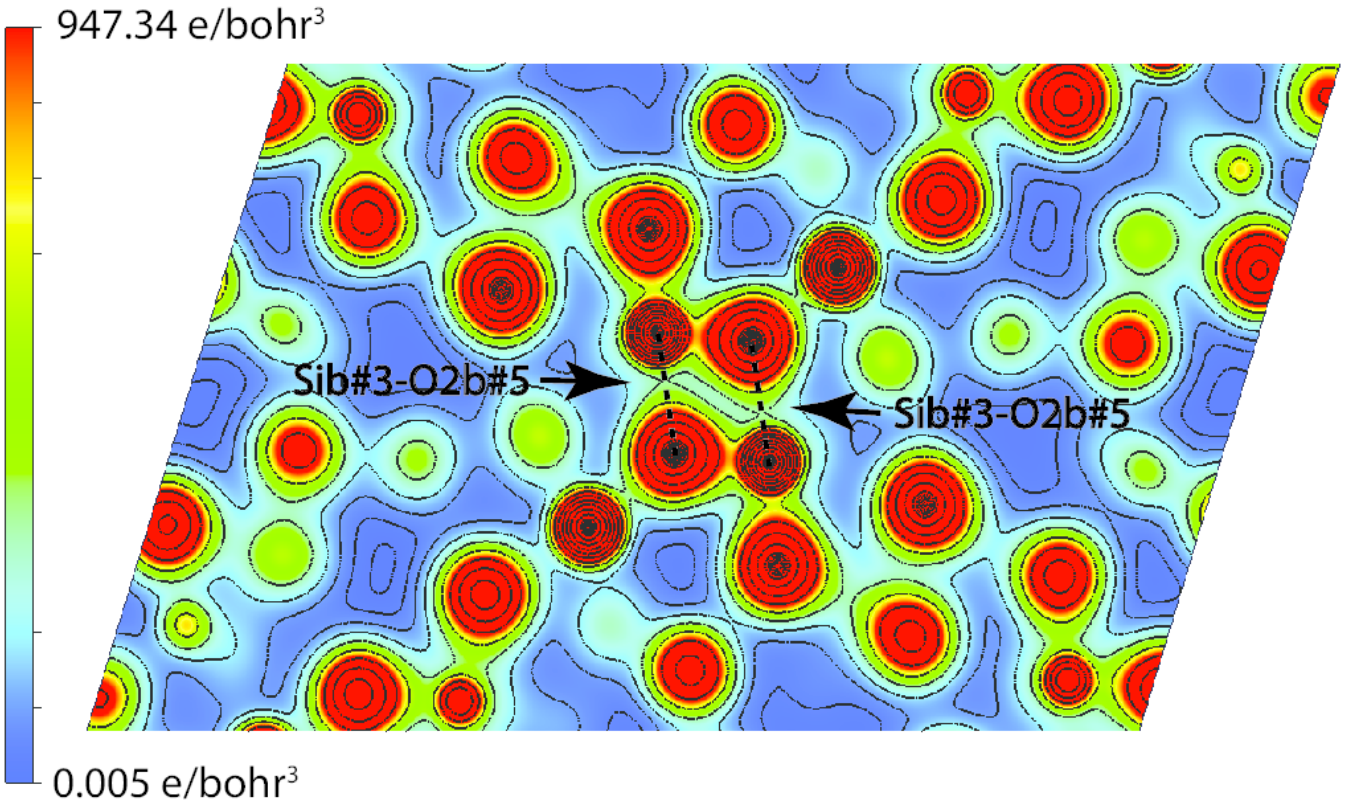

Figure 4.10: Calculated electron density map of along (2 -1 -1) direction in γ-diopside at P11=55.1 GPa. Contour lines: F(N)=A×BN/step. A=5, B=50, N=-5, N=20, step=10. Sib#3-O2b#5=1.98 Å.

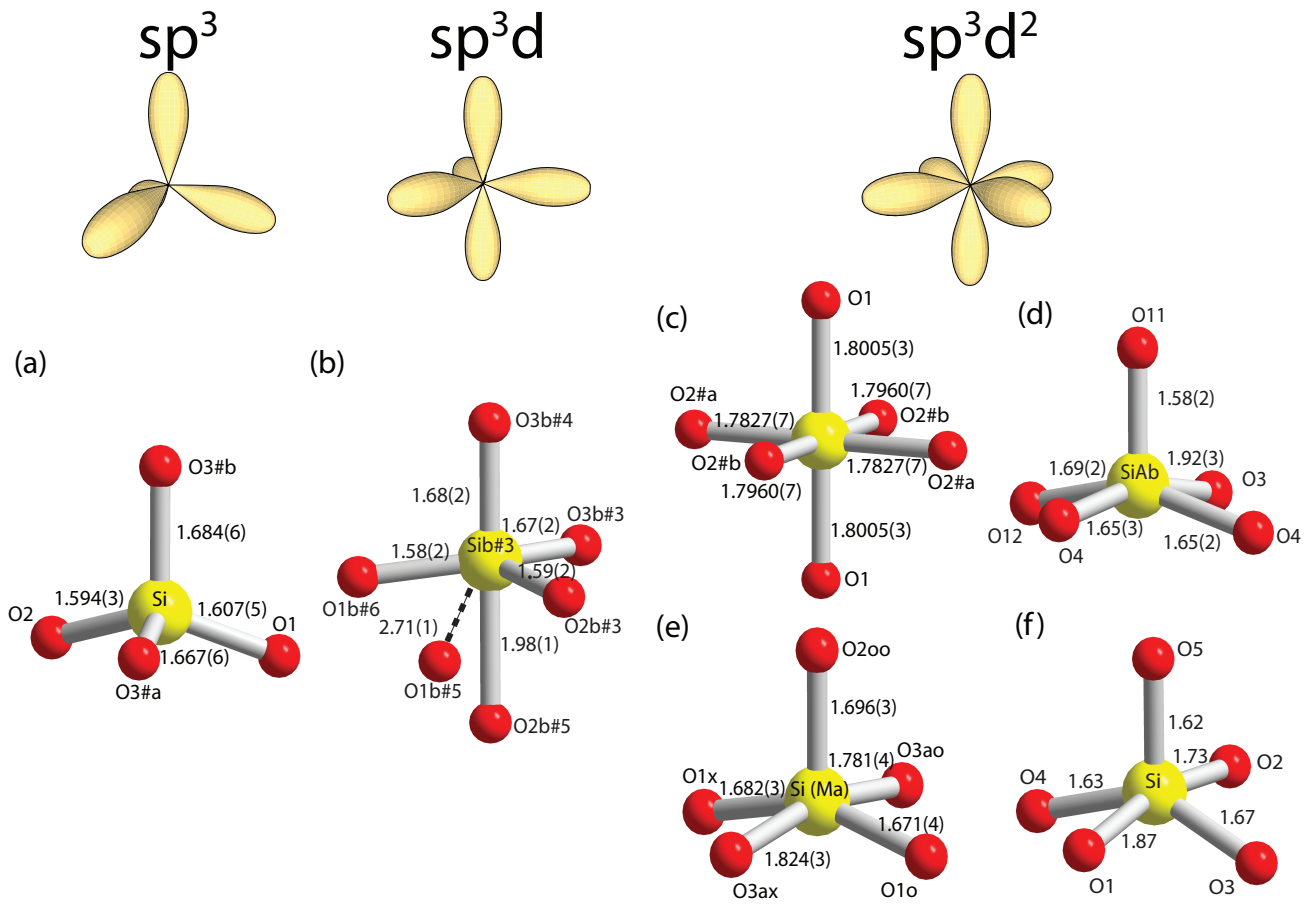

Figure 4.11: Local structure of SiO_4, SiO_5 and SiO_6. (a) SiO_4 in diopside at ambient conditions. (b) SiO_5 in γ-diopside at P11=55.1(1) GPa. Non-bond is denoted by a dash line. (c) SiO_6 in bridgmanite [17]. (d) SiO_5 in high-pressure β-popx enstatite [12]. (e) SiO_5 in $CaSi_2O_5$ [18]. (f) SiO_5 in high-pressure silica by DFT calculations [13].

Table 4.5: Si-O distances and polyhedral parameters in layer 1 and layer 2. C2/c: #0, x, y, z; #1, x, -y+1, z+1/2; #2, x+3/2, -y+3/2, -z+1. #3, x-1/2, y-1/2, z; #4, x-1/2, -y+1/2, z+1/2; #5, -x+1, -y+1, -z; #6, x-1/2, -y+1/2, z-1/2. $P2_1/c$: #0, x, y, z; #1, x,-y+1/2, z-1/2; #2, -x+1, -y+1, -z. #3, x, y-1, z; #4, x, -y+1/2, z+1/2; #5, -x, -y, -z; #6, -x, y-1/2, -z+1/2. Blue and black indicate the color of distances used in figure 4.8.

Phase		**α-diopside**		**γ-diopside**	**β-diopside**
Pressure (GPa)		P9=48.4(1)		P11=55.1(1)	P14=47.0(1)
Space Group		C2/c		$P2_1/c$	
		Layer 1			
Si Coordination		4		6	6
Si-O Distances (Å)	Si#0-O1#0	1.550(5)	Sia#1-O1a#1	1.79(2)	1.86(2)
	Si#0-O2#0	1.553(5)	Sia#1-O2a#2	1.68(2)	1.72(3)
	Si#0-O3#0	1.619(6)	Sia#1-O3a#1	1.67(2)	1.67(2)
	Si#0-O3#1	1.640(5)	Sia#1-O3a#0	1.66(2)	1.68(2)
	Si#0-O2#2(blue)	2.764(6)	Sia#1-O2a#0(blue)	1.71(2)	1.76(3)
	Si#0-O1#1(black)	3.174(6)	Sia#1-O1a#0(black)	1.89(2)	1.90(2)
Average Bondlength (Å)		1.590(6)		1.73(2)	1.76(2)
Polyhedral Volume ($Å^3$)		2.0351		6.7934	7.1962
Quadratic Elongation		1.0101		1.0178	1.0143
Bond Angle Variance ($deg.^2$)		41.2691		52.2535	39.8586
θ (°)	O3-O3-O3	156.2(4)	O3a-O3a-O3a	213(1)	239(1)
		Layer 2			
Si Coordination		4		5	4
Si-O Distances (Å)	Si#3-O1#3	1.550(5)	Sib#3-O1b#6	1.60(3)	1.58(3)
	Si#3-O2#3	1.553(5)	Sib#3-O2b#3	1.60(2)	1.57(2)
	Si#3-O3#3	1.619(6)	Sib#3-O3b#3	1.66(2)	1.65(2)
	Si#3-O3#4	1.640(5)	Sib#3-O3b#4	1.67(2)	1.65(2)
	Si#3-O2#5(blue)	3.024(5)	Sib#3-O2b#5(blue)	1.95(2)	2.41(2)
	Si#3-O1#6(black)	3.385(5)	Sib#3-O1b#5(black)	2.71(2)	3.02(2)
Average Bonglength (Å)		1.590(6)		1.70(2)	1.61(2)
Polyhedral Volume ($Å^3$)		2.0351		3.9513	2.068
Quadratic Elongation		1.0101		1.3783	1.0267
Bond Angle Variance ($deg.^2$)		41.2691		86.5511	107.0202
θ (°)	O3-O3-O3	156.2(4)	O3b-O3b-O3b	207(2)	210(1)

CHAPTER 5
CONCLUSIONS AND FUTURE WORK

The subduction zone is an important place where phenomena such as earthquakes and volcanic eruptions take place. Subducted slabs also play a crucial role in the global mantle convection — the most important process in the deep Earth. However, there are many unsolved problems related to this process, such as slab stagnation at the mantle transition zone and deep-focus earthquakes [19, 149]. These phenomena are believed to be related to mineral phases and phase transitions in the subducted slab[37, 149].

Pyroxene is an important group of minerals in the subducted slab and the upper mantle. In the normal upper mantle, where the temperature is high, pyroxene gradually dissolves into garnet and form majoritic garnet at the depth of the transition zone [28]. However, recent studies show that the transition from pyroxene to garnet is slow, especially in cold environment such as the the cold subducted slab. Therefore, it is possible that pyroxene can be preserved to the bottom of the transition zone and the top of the lower mantle and explain the slab stagnation phenomena [33].

This thesis reported the results of high pressure studies of two clinopyroxenes — diopside ($CaMgSi_2O_6$) and hedenbergite ($CaFeSi_2O_6$), and studied the role of metastable pyroxene in the subducted slab by modeling. At ambient temperature, diopside and hedenbergite can be preserved to $\sim$ 50 GPa and 33 GPa without phase transitions. The density of diopside and hedenbergite is determined by single-crystal X-ray diffraction and is modeled along the cold subducting slab geotherm. Aluminous iron-bearing diopside shows higher density than the end-member diopside and therefore provides larger pulling force to the subducted slab. At the bottom of the transition zone and top of the lower mantle, eclogite with aluminous iron-bearing diopside has higher density than that with end-member diopside. However, it is still less dense than the surrounding mantle and therefore could contribute to the buoyancy force, associated with the slab stagnation.

A new phase (γ-diopside) with Si in five-coordinated sites is observed in diopside above 50 GPa, which suggests a new low-energy phase transition path that involves a displacive and reversible mechanism. γ-diopside, though denser than α-diopside, is lighter than the stable lower mantle minerals ($CaSiO_3$ + $MgSiO_3$ perovskite mixture). This results supported the idea that metastable phases contribute to the slab stagnancy, even after going through phase transitions to a denser phase.

Much work on experiments and modeling have been left for the future due to lack of time. Future work should concern the high-temperature measurements, kinetic studies of phase transitions and geodynamic modeling.

High-temperature high-pressure experiments to 1000 °C should be done for clinopyroxenes. Although the temperature in the cold subducted slabs is lower than the surrounding mantle, it

can still be as high as 1000 °C [37]. Temperature affects the stability regions, density and bulk modulus of clinopyroxenes, which are important in the geodynamic modeling. High-pressure high-temperature experiments can be non-trivial. There are two ways of heating samples in diamond anvil cell experiments: (1) laser heating and (2) resistive heating. Laser heating device is not usually designed for generating temperature < 1000 °C due to its limitation in power control and temperature measurement. Resistive heating is used routinely for generating high temperature in the range of 25 — 1000 °C. In resistive heating high-pressure experiments, heaters are usually made of metal alloy [159] or graphite [160]. Thermocouples are used for temperature measurements. Temperature can be controlled by proportional-integral-derivative feedback system. Water-cooling systems are usually used to protect the sample stage from over-heating.

The kinetics of phase transitions in the clinopyroxene system, which plays an important role in the mineral phase determination, should also be studied. This kind of measurements can be done with time-resolved X-ray diffraction [161, 162] or modeling (e.g. molecular dynamics) [163, 164]. However, kinetic measurements of phase transitions can be hard by experiments or calculations. It is hard in experiment because of the timescale can be either too long or too short compared to the experimental time. Kinetic properties are also hard to model because of its multi-scale nature.

The physical properties (density, bulk modulus etc.) of clinopyroxene at high pressure measured in this thesis can be useful for geodynamic modeling and seismic signal interpretation. Density, which controls the buoyancy force of the slab, is important in geodynamics modeling [21], Density together with bulk modulus and shear modulus can also be used for calculating seismic wave velocities, which are necessary for interpreting seismic wave signals. Geodynamics modeling should be done in the future to test the ideas in the thesis.

APPENDIX A
APPENDIX

A.1 Appendix A

A.2 Appendix B

$$\mathbf{T} = \begin{bmatrix} -3.14733766 \times 10^{-01} & 1.09086550 \times 10^{-01} & -2.52920903 \times 10^{-02} & 9.33980234 \times 10^{-01} \\ -4.94377728 \times 10^{-03} & -1.90909650 \times 10^{-02} & 4.54070972 \times 10^{-03} & -8.46801689 \times 10^{-02} \\ -5.00126169 \times 10^{-03} & -9.17993656 \times 10^{-03} & -5.63661029 \times 10^{-03} & -1.88011572 \times 10^{-02} \\ -7.38983052 \times 10^{-04} & -9.89425134 \times 10^{-04} & -9.29419357 \times 10^{-04} & -1.41990016 \times 10^{-03} \\ -6.55715355 \times 10^{-03} & -1.48063535 \times 10^{-02} & -4.23579702 \times 10^{-03} & -5.19453756 \times 10^{-02} \\ -4.80085459 \times 10^{-01} & -6.50564121 \times 10^{-01} & -5.77211547 \times 10^{-01} & -9.79231231 \times 10^{-02} \\ -1.51823572 \times 10^{-01} & 7.20878458 \times 10^{-01} & -6.58209460 \times 10^{-01} & -1.53049700 \times 10^{-01} \\ -2.18287107 \times 10^{-03} & -5.48809988 \times 10^{-03} & -4.72190648 \times 10^{-03} & -4.58170847 \times 10^{-03} \\ 4.66607675 \times 10^{-01} & -1.14826634 \times 10^{-01} & -2.43972955 \times 10^{-01} & 9.93617189 \times 10^{-02} \\ -1.30319664 \times 10^{-04} & -1.11181765 \times 10^{-03} & -2.84884381 \times 10^{-03} & 3.89458174 \times 10^{-03} \\ -1.07641687 \times 10^{-03} & -4.60579225 \times 10^{-03} & -4.17526782 \times 10^{-03} & -4.43584506 \times 10^{-03} \\ -1.38527295 \times 10^{-02} & 2.34002984 \times 10^{-02} & 5.43279494 \times 10^{-02} & 3.92036679 \times 10^{-02} \\ -4.65404190 \times 10^{-04} & -1.13179698 \times 10^{-03} & -1.12625678 \times 10^{-03} & 1.16152162 \times 10^{-03} \\ -4.63355392 \times 10^{-01} & 1.23986240 \times 10^{-01} & 2.91849969 \times 10^{-01} & -1.91018791 \times 10^{-01} \\ 4.63355392 \times 10^{-01} & -1.23986240 \times 10^{-01} & -2.91849969 \times 10^{-01} & 1.91018791 \times 10^{-01} \end{bmatrix} \tag{A.1}$$

$$\mathbf{Z} = \begin{bmatrix}
-3.79973470 \times 10^{-01} & -4.64632360 \times 10^{-01} & -2.44017646 \times 10^{-02} & -4.25461476 \times 10^{-03} \\
-6.83011369 \times 10^{-02} & -3.89307820 \times 10^{-01} & -1.52646054 \times 10^{-01} & 1.29262915 \times 10^{-01} \\
-2.55642944 \times 10^{-01} & -2.18340168 \times 10^{-01} & -2.56217407 \times 10^{-02} & -9.53743114 \times 10^{-03} \\
-1.99638936 \times 10^{-01} & -5.91539240 \times 10^{-02} & -1.05691313 \times 10^{-01} & 4.61593461 \times 10^{-02} \\
-2.48159345 \times 10^{-01} & -2.57549687 \times 10^{-01} & 1.80690652 \times 10^{-01} & 6.94766656 \times 10^{-02} \\
-3.54604233 \times 10^{-01} & -4.03966737 \times 10^{-01} & -3.05668599 \times 10^{-02} & 2.24977818 \times 10^{-02} \\
-1.06478233 \times 10^{-01} & -3.43024574 \times 10^{-01} & -9.77068098 \times 10^{-02} & 8.15731496 \times 10^{-02} \\
-3.95974110 \times 10^{-01} & -4.80193083 \times 10^{-01} & -1.42766131 \times 10^{-02} & 2.75186261 \times 10^{-02} \\
-3.81362732 \times 10^{-01} & -4.49582765 \times 10^{-01} & -2.29868231 \times 10^{-02} & -4.47030226 \times 10^{-03} \\
-1.15559717 \times 10^{-01} & -4.26344530 \times 10^{-01} & 3.62155875 \times 10^{-02} & -2.07609196 \times 10^{-01} \\
-2.43575368 \times 10^{-01} & -2.54982399 \times 10^{-02} & -3.92773248 \times 10^{-02} & -3.29895433 \times 10^{-02} \\
-5.60996294 \times 10^{-02} & 7.56278817 \times 10^{-01} & -3.44989350 \times 10^{-02} & -8.73263542 \times 10^{-03} \\
-1.03821030 \times 10^{-01} & 7.40390812 \times 10^{-01} & -8.63647558 \times 10^{-02} & -2.15440271 \times 10^{-02} \\
-1.10766063 \times 10^{-01} & 5.33028464 \times 10^{-01} & 1.98703146 \times 10^{-02} & 9.78157050 \times 10^{-03} \\
-1.76429251 \times 10^{-01} & -2.63438111 \times 10^{-01} & -2.97556581 \times 10^{-02} & -8.37624846 \times 10^{-02} \\
1.46810515 \times 10^{+00} & -2.05907365 \times 10^{-01} & -2.77368749 \times 10^{-01} & 6.04098514 \times 10^{-01} \\
-4.05298764 \times 10^{-01} & -4.93672371 \times 10^{-01} & -2.69074030 \times 10^{-02} & 2.47760903 \times 10^{-02} \\
-3.43663442 \times 10^{-01} & -5.18450952 \times 10^{-01} & -2.26961444 \times 10^{-02} & -1.72409032 \times 10^{-01} \\
-1.10766063 \times 10^{-01} & 5.33028464 \times 10^{-01} & 1.98703146 \times 10^{-02} & 9.78157050 \times 10^{-03} \\
-7.70368766 \times 10^{-02} & 8.77770208 \times 10^{-01} & -1.07905316 \times 10^{-01} & -3.03504864 \times 10^{-02} \\
-4.05298764 \times 10^{-01} & -4.93672371 \times 10^{-01} & -2.69074030 \times 10^{-02} & 2.47760903 \times 10^{-02} \\
-3.76280413 \times 10^{-01} & -3.72436847 \times 10^{-01} & -3.40676185 \times 10^{-02} & 1.99029009 \times 10^{-02} \\
-3.46507060 \times 10^{-01} & -2.48047005 \times 10^{-01} & -4.14141293 \times 10^{-02} & 1.49029204 \times 10^{-02} \\
-3.15945878 \times 10^{-01} & -1.20365701 \times 10^{-01} & -4.89550350 \times 10^{-02} & 9.77063614 \times 10^{-03} \\
-2.84531216 \times 10^{-01} & 1.08813536 \times 10^{-02} & -5.67065353 \times 10^{-02} & 4.49502275 \times 10^{-03} \\
-2.52295898 \times 10^{-01} & 1.45557015 \times 10^{-01} & -6.46605304 \times 10^{-02} & -9.18407077 \times 10^{-04} \\
-2.19174274 \times 10^{-01} & 2.83935571 \times 10^{-01} & -7.28332198 \times 10^{-02} & -6.48067867 \times 10^{-03} \\
-1.85133516 \times 10^{-01} & 4.26154166 \times 10^{-01} & -8.12327034 \times 10^{-02} & -1.21973047 \times 10^{-02} \\
-1.50107973 \times 10^{-01} & 5.72487090 \times 10^{-01} & -8.98751807 \times 10^{-02} & -1.80793104 \times 10^{-02} \\
-1.14097644 \times 10^{-01} & 7.22934340 \times 10^{-01} & -9.87606518 \times 10^{-02} & -2.41266959 \times 10^{-02} \\
-7.70368766 \times 10^{-02} & 8.77770208 \times 10^{-01} & -1.07905316 \times 10^{-01} & -3.03504864 \times 10^{-02} \\
7.47866949 \times 10^{-02} & 1.56891750 \times 10^{-01} & 5.50304144 \times 10^{-01} & 1.22699213 \times 10^{-01} \\
2.45591917 \times 10^{-01} & 1.09703183 \times 10^{-01} & 4.70066064 \times 10^{-01} & 7.74411201 \times 10^{-02} \\
4.16397140 \times 10^{-01} & 6.25146170 \times 10^{-02} & 3.89827983 \times 10^{-01} & 3.21830268 \times 10^{-02} \\
6.72604973 \times 10^{-01} & -8.26823277 \times 10^{-03} & 2.69470863 \times 10^{-01} & -3.57041131 \times 10^{-02} \\
9.28812807 \times 10^{-01} & -7.90510825 \times 10^{-02} & 1.49113743 \times 10^{-01} & -1.03591253 \times 10^{-01} \\
1.27042325 \times 10^{+00} & -1.73428216 \times 10^{-01} & -1.13624179 \times 10^{-02} & -1.94107440 \times 10^{-01} \\
1.78283892 \times 10^{+00} & -3.14993915 \times 10^{-01} & -2.52076659 \times 10^{-01} & -3.29881720 \times 10^{-01}
\end{bmatrix} \tag{A.2}$$

BIBLIOGRAPHY

[1] Alfred Edward Ringwood. Phase transformations and differentiation in subducted lithosphere: implications for mantle dynamics, basalt petrogenesis, and crustal evolution. *The Journal of Geology*, 90(6):611–643, 1982.

[2] Roberta L Flemming, Victor Terskikh, and Eric Ye. Aluminum environments in synthetic catschermak clinopyroxene (caalalsio6) from rietveld refinement, 27al nmr, and first-principles calculations. *American Mineralogist*, 100(10):2219–2230, 2015.

[3] Li Zhang, Hans Ahsbahs, Stefan S Hafner, and Ali Kutoglu. Single-crystal compression and crystal structure of clinopyroxene up to 10 gpa. *American Mineralogist*, 82(3-4):245–258, 1997.

[4] M. Tribaudino, M. Prencipe, M. Bruno, and D. Levy. High-pressure behaviour of Ca-rich C2/c clinopyroxenes along the join diopside-enstatite ($CaMgSiO_6$-$Mg_2Si_2O_6$). *Physics and Chemistry of Minerals*, 27:656–664, 2000.

[5] Y. Hu, P. Dera, and K. Zhuravlev. Single-crystal diffraction and Raman spectroscopy of hedenbergite up to 33 GPa. *Physics and Chemistry of Minerals*, 42(7):595–608, 2015.

[6] J Nolan. Physical properties of synthetic and natural pyroxenes in the system diopside-hedenbergite-acmite. *Mineralogical Magazine*, 37(286):216, 1969.

[7] RC Newton, TV Charlu, and OJ Kleppa. Thermochemistry of high pressure garnets and clinopyroxenes in the system cao-mgo-al2o3-sio2. *Geochimica et Cosmochimica Acta*, 41(3):369–377, 1977.

[8] L Stixrude. Properties of rocks and minerals-seismic properties of rocks and minerals, and the structure of the earth. Elsevier, 2007.

[9] Craig R Bina. Mineralogy: Garnet goes hungry. *Nature Geoscience*, 6(5):335–336, 2013.

[10] C. Sanloup, J.W.E. Drewitt, Z. Konopkova, P. Dalladay-Simpson, D.M. Morton, N. Rai, W. van Westrenen, and W. Morgenroth. Structural change in molten basalt at deep mantle conditions. *Nature*, 503(7474):104–107, 2013.

[11] N. Sun, L. Stixrude, N. de Koker, and B.B. Karki. First principles molecular dynamics simulations of diopside ($CaMgSi_2O_6$) liquid to high pressure. *Geochimica et Cosmochimica Acta*, 75(13):3792–3802, 2011.

[12] G J Finkelstein, P K Dera, and T S Duffy. Phase transitions in orthopyroxene (En_{90}) to 49 GPa from single-crystal X-ray diffraction. *Physics of the Earth and Planetary Interiors*, 244(0):78–86, 2015.

[13] J. Badro, D.M. Teter, R.T. Downs, P. Gillet, R.J. Hemley, and J.-L. Barrat. Theoretical study of a five-coordinated silica polymorph. *Physical Review B*, 56(10):5797–5806, 1997.

[14] RM Wentzcovitch, BB Karki, M Cococcioni, and S De Gironcoli. Thermoelastic properties of $MgSiO_3$-Perovskite: insights on the nature of the earth's lower mantle. *Physical Review Letters*, 92(1):018501, 2004.

[15] R Caracas, R Wentzcovitch, G David Price, and J Brodholt. $CaSiO_3$ perovskite at lower mantle pressures. *Geophysical Research Letters*, 32(6), 2005.

[16] BB Karki, W Duan, CRS Da Silva, and RM Wentzcovitch. Ab initio structure of $MgSiO_3$ ilmenite at high pressure. *American Mineralogist*, 85(2):317–320, 2000.

[17] Hiroyuki Horiuchi. Perovskite-type $MgSiO_3$-single-crystal X-ray-diffraction study. *American Mineralogist*, 3:357–360, 1987.

[18] R. J. Angel, N. L. Ross, F. Seifert, and T. F. Fliervoet. Structural characterization of pentacoordinate silicon in a calcium silicate. *Nature*, 384(6608):441–444, 1996.

[19] Yoshio Fukao, Masayuki Obayashi, Tomoeki Nakakuki, and Deep Slab Project Group. Stagnant slab: A review. *Annual Review of Earth and Planetary Sciences*, 37:19–46, 2009.

[20] Harry W Green and Heidi Houston. The mechanics of deep earthquakes. *Annual Review of Earth and Planetary Sciences*, 23(1):169–213, 1995.

[21] CR Bina and G Helffrich. Geophysical constraints on mantle composition. *Treatise on geochemistry*, 2014.

[22] WG Melson, TL Vallier, TL Wright, Gary Byerly, and J Nelen. Chemical diversity of abyssal volcanic glass erupted along pacific, atlantic, and indian ocean sea-floor spreading centers. *The geophysics of the Pacific ocean basin and its margin*, pages 351–367, 1976.

[23] DH Green. Petrogenesis of mid ocean ridge basalts. *The Earth: its origin, structure and evolution*, pages 200–299, 1979.

[24] Stefano Poli and Max W Schmidt. Petrology of subducted slabs. *Annual Review of Earth and Planetary Sciences*, 30(1):207–235, 2002.

[25] Alfred E Ringwood. Composition and petrology of the earth's mantle. *MacGraw-Hill*, 618, 1975.

[26] Tomoo Katsura, Akira Yoneda, Daisuke Yamazaki, Takashi Yoshino, and Eiji Ito. Adiabatic temperature profile in the mantle. *Physics of the Earth and Planetary Interiors*, 183(1-2):212–218, 2010.

[27] Daniel J Frost. The upper mantle and transition zone. *Elements*, 4(3):171–176, 2008.

[28] T Irifune and T Tsuchiya. Mineral of the earth - phase transitions and mineralogy of the lower mantle. *Treatise on Geophysics, 2, Mineral Physics*, 2007.

[29] R Kind. Deep earth structure-transition zone and mantle discontinuities. *Treatise on Geophysics, 1, Seismology and Structure of the Earth*, pages 591–618, 2007.

[30] Stefano Poli. The amphibolite-eclogite transformation; an experimental study on basalt. *American Journal of Science*, 293(10):1061–1107, 1993.

[31] Yi Hu, Zhongqing Wu, Przemyslaw K Dera, and Craig R Bina. Thermodynamic and elastic properties of pyrope at high pressure and high temperature by first-principles calculations. *Journal of Geophysical Research: Solid Earth*, 121(9):6462–6476, 2016.

[32] T Irifune and AE Ringwood. Phase transformations in subducted oceanic crust and buoyancy relationships at depths of 600–800 km in the mantle. *Earth and Planetary Science Letters*, 117(1-2):101–110, 1993.

[33] WL Van Mierlo, F Langenhorst, DJ Frost, and DC Rubie. Stagnation of subducting slabs in the transition zone due to slow diffusion in majoritic garnet. *Nature Geoscience*, 6(5):400, 2013.

[34] Masayuki Nishi, Tomoaki Kubo, Hiroaki Ohfuji, Takumi Kato, Yu Nishihara, and Tetsuo Irifune. Slow si–al interdiffusion in garnet and stagnation of subducting slabs. *Earth and Planetary Science Letters*, 361:44–49, 2013.

[35] Yu Nishihara, Toru Shinmei, and Shun-ichiro Karato. Grain-growth kinetics in wadsleyite: effects of chemical environment. *Physics of the Earth and Planetary Interiors*, 154(1):30–43, 2006.

[36] Masayuki Nishi, Takumi Kato, Tomoaki Kubo, and Takumi Kikegawa. Survival of pyropic garnet in subducting plates. *Physics of the Earth and Planetary Interiors*, 170(3-4):274–280, 2008.

[37] S.D. King, D.J. Frost, and D.C. Rubie. Why cold slabs stagnate in the transition zone. *Geology*, 43(3):231–234, 2015.

[38] Daisuke Yamazaki, Toru Inoue, Mana Okamoto, and Tetsuo Irifune. Grain growth kinetics of ringwoodite and its implication for rheology of the subducting slab. *Earth and Planetary Science Letters*, 236(3-4):871–881, 2005.

[39] Ulrich R Christensen and David A Yuen. The interaction of a subducting lithospheric slab with a chemical or phase boundary. *Journal of Geophysical Research: Solid Earth*, 89(B6):4389–4402, 1984.

[40] Maryellen Cameron and JJ Papike. Structural and chemical variations in pyroxenes. *American Mineralogist*, 66(1-2):1–50, 1981.

[41] Francis Nimmo. Energetics of the core. *Treatise on Geophysics, 8, Core Dynamics*, 8:31–65, 2007.

[42] J Michael Brown and Robert G McQueen. Phase transitions, grüneisen parameter, and elasticity for shocked iron between 77 gpa and 400 gpa. *Journal of Geophysical Research: Solid Earth*, 91(B7):7485–7494, 1986.

[43] Frederica Coppari, RF Smith, JH Eggert, J Wang, JR Rygg, A Lazicki, JA Hawreliak, GW Collins, and TS Duffy. Experimental evidence for a phase transition in magnesium oxide at exoplanet pressures. *Nature Geoscience*, 6(11):926, 2013.

[44] M Millot, N a Dubrovinskaia, A Černok, S Blaha, L Dubrovinsky, DG Braun, PM Celliers, GW Collins, JH Eggert, and R Jeanloz. Shock compression of stishovite and melting of silica at planetary interior conditions. *Science*, 347(6220):418–420, 2015.

[45] Jue Wang, Federica Coppari, Raymond F Smith, Jon H Eggert, Amy E Lazicki, Dayne E Fratanduono, J Ryan Rygg, Thomas R Boehly, Gilbert W Collins, and Thomas S Duffy. X-ray diffraction of molybdenum under ramp compression to 1 tpa. *Physical Review B*, 94(10):104102, 2016.

[46] RF Smith, JH Eggert, R Jeanloz, TS Duffy, DG Braun, JR Patterson, RE Rudd, J Biener, AE Lazicki, AV Hamza, et al. Ramp compression of diamond to five terapascals. *Nature*, 511(7509):330, 2014.

[47] E Ito. Theory and practice — multi-anvil cells and high pressure experimental methods. *Treatise on geophysics, 2, Mineral Physics*, pages 197–230, 2007.

[48] Takayuki Ishii, Daisuke Yamazaki, Noriyoshi Tsujino, Fang Xu, Zhaodong Liu, Takaaki Kawazoe, Takafumi Yamamoto, Dmitry Druzhbin, Lin Wang, Yuji Higo, et al. Pressure generation to 65 gpa in a kawai-type multi-anvil apparatus with tungsten carbide anvils. *High Pressure Research*, 37(4):507–515, 2017.

[49] HK Mao, WL Mao, and S Gerald. Theory and practice — diamond-anvil cells and probes for high pt mineral physics studies. *Treatise on geophysics, 2, Mineral Physics*, pages 231–267, 2007.

[50] Mark Rivers, Vitali B Prakapenka, Atsushi Kubo, Clayton Pullins, Christopher M Holl, and Steven D Jacobsen. The compres/gsecars gas-loading system for diamond anvil cells at the advanced photon source. *High Pressure Research*, 28(3):273–292, 2008.

[51] Ranga P Dias and Isaac F Silvera. Observation of the wigner-huntington transition to metallic hydrogen. *Science*, page eaal1579, 2017.

[52] I Kantor, V Prakapenka, A Kantor, P Dera, A Kurnosov, S Sinogeikin, N Dubrovinskaia, and L Dubrovinsky. Bx90: A new diamond anvil cell design for x-ray diffraction and optical measurements. *Review of Scientific Instruments*, 83(12):125102, 2012.

[53] Reinhard Boehler and Koen De Hantsetters. New anvil designs in diamond-cells. *High Pressure Research*, 24(3):391–396, 2004.

[54] Alexander Kurnosov, Innokenty Kantor, Tiziana Boffa-Ballaran, Sven Lindhardt, Leonid Dubrovinsky, Alexei Kuznetsov, and Beat H Zehnder. A novel gas-loading system for mechanically closing of various types of diamond anvil cells. *Review of Scientific Instruments*, 79(4):045110, 2008.

[55] S Klotz, JC Chervin, P Munsch, and G Le Marchand. Hydrostatic limits of 11 pressure transmitting media. *Journal of Physics D: Applied Physics*, 42(7):075413, 2009.

[56] LUTZ Nasdala, JENS Götze, JOHN M Hanchar, MICHAEL Gaft, MATTHIAS R Krbetschek, A Beran, and E Libowitzky. Luminescenca technieues in earth sciences. *Spectroscopic methods in mineralogy*, 6:43–91, 2004.

[57] Jon H Eggert, Kenneth A Goettel, and Isaac F Silvera. Ruby at high pressure. i. optical line shifts to 156 gpa. *Physical Review B*, 40(8):5724, 1989.

[58] H.K. Mao, J. Xu, and P.M. Bell. Calibration of the ruby pressure gauge to 800 kbar under quasi-hydrostatic conditions. *Journal of Geophysical Research: Solid Earth*, 91(B5):4673–4676, 1986.

[59] JA Xu, HK Mao, and PM Bell. High-pressure ruby and diamond fluorescence: observations at 0.21 to 0.55 terapascal. *Science*, 232(4756):1404–1406, 1986.

[60] Agnes Dewaele, Frédéric Datchi, Paul Loubeyre, and Mohamed Mezouar. High pressure–high temperature equations of state of neon and diamond. *Physical Review B*, 77(9):094106, 2008.

[61] A. Guinier. *X-Ray Diffraction: In Crystals, Imperfect Crystals, and Amorphous Bodies*. Dover Books on Physics. Dover Publications, 2013.

[62] Maureen M Julian. *Foundations of crystallography with computer applications*. CRC Press, 2014.

[63] Li Zhang, Yue Meng, Wenge Yang, Lin Wang, Wendy L Mao, Qiao-Shi Zeng, Jong Seok Jeong, Andrew J Wagner, K Andre Mkhoyan, Wenjun Liu, et al. Disproportionation of (mg, fe) sio3 perovskite in earths deep lower mantle. *Science*, 344(6186):877–882, 2014.

[64] P. Dera, K. Zhuravlev, V. Prakapenka, M.L. Rivers, G.J. Finkelstein, O. Grubor-Urosevic, O. Tschauner, S.M. Clark, and R.T. Downs. High pressure single-crystal micro X-ray diffraction analysis with GSEADARSV software. *High Pressure Research*, 33(3):466–484, 2013.

[65] Jin S Zhang, Przemyslaw Dera, and Jay D Bass. A new high-pressure phase transition in natural fe-bearing orthoenstatite. *American Mineralogist*, 97(7):1070–1074, 2012.

[66] P. Dera, G.J. Finkelstein, T.S. Duffy, R.T. Downs, Y. Meng, V. Prakapenka, and S. Tkachev. Metastable high-pressure transformations of orthoferrosilite Fs_{82}. *Physics of the Earth and Planetary Interiors*, 221:15–21, 2013.

[67] George M Sheldrick. Cell now, program for unit cell determination. *University of Göttingen: Germany*, 2003.

[68] Thomas R Schneider and George M Sheldrick. Substructure solution with shelxd. *Acta Crystallographica Section D: Biological Crystallography*, 58(10):1772–1779, 2002.

[69] George M Sheldrick. Shelxt–integrated space-group and crystal-structure determination. *Acta Crystallographica Section A: Foundations and Advances*, 71(1):3–8, 2015.

[70] P Mueller, R Herbst-Irmer, A.L. Spek, T.R. Schneider, and M.R. Sawaya. *Crystal structure refinement — A crystallographer's guide to SHELXL*. Oxford science publications, 2009.

[71] Joel Ita and Lars Stixrude. Petrology, elasticity, and composition of the mantle transition zone. *Journal of Geophysical Research: Solid Earth*, 97(B5):6849–6866, 1992.

[72] AE Ringwood. The pyroxene-garnet transformation in the earth's mantle. *Earth and Planetary Science Letters*, 2(3):255–263, 1967.

[73] Satoshi Kaneshima, Taro Okamoto, and Hiroshi Takenaka. Evidence for a metastable olivine wedge inside the subducted mariana slab. *Earth and Planetary Science Letters*, 258(1-2):219–227, 2007.

[74] Guoming Jiang, Dapeng Zhao, and Guibin Zhang. Seismic evidence for a metastable olivine wedge in the subducting pacific slab under japan sea. *Earth and Planetary Science Letters*, 270(3-4):300–307, 2008.

[75] Guoming Jiang, Dapeng Zhao, and Guibin Zhang. Detection of metastable olivine wedge in the western pacific slab and its geodynamic implications. *Physics of the Earth and Planetary Interiors*, 238:1–7, 2015.

[76] A.M. Plonka, P. Dera, P. Irmen, M.L. Rivers, L. Ehm, and J.B. Parise. β-diopside, a new ultrahigh-pressure polymorph of $CaMgSi_2O_6$ with six-coordinated silicon. *Geophysical Research Letters*, 39(24), 2012.

[77] Alexander N Krot, Adrian J Brearley, Michael I Petaev, Gregory W Kallemeyn, Derek WG Sears, Paul H Benoit, Ian D Hutcheon, Michael E Zolensky, and Klaus Keil. Evidence for low-temperature growth of fayalite and hedenbergite in macalpine hills 88107, an ungrouped carbonaceous chondrite related to the cm-co clan. *Meteoritics & Planetary Science*, 35(6):1365–1386, 2000.

[78] Lawrence D Meinert. Skarns and skarn deposits. *Geoscience Canada*, 19(4), 1992.

[79] L Zhang, J Stanek, SS Hafner, H Ahsbahs, HF Grünsteudel, and J Metge. 57fe nuclear forward scattering of synchrotron radiation in hedenbergite cafesi2o6 at hydrostatic pressures up to 68 gpa. *American Mineralogist*, 84(3):447–453, 1999.

[80] Y-H Kim, LC Ming, MH Manghnani, and J Ko. Phase transformation studies on a synthetic hedenbergite up to 26 gpa at 1200 c. *Physics and Chemistry of Minerals*, 17(6):540–544, 1991.

[81] Young-Ho Kim, Li Chung Ming, and Murli H Manghnani. A study of phase transformation in hedenbergite to 40 gpa at 1200 c. *Physics and Chemistry of Minerals*, 16(8):757–762, 1989.

[82] Bernard J Wood and Jonathan D Blundy. A predictive model for rare earth element partitioning between clinopyroxene and anhydrous silicate melt. *Contributions to Mineralogy and Petrology*, 129(2-3):166–181, 1997.

[83] John A Chermak and J Donald Rimstidt. Estimating the thermodynamic properties (delta g of and delta h of) of silicate minerals at 298 k from the sum of polyhedral contributions. *American Mineralogist*, 74(9-10):1023–1031, 1989.

[84] VJ Van Hinsberg, SP Vriend, and JC Schumacher. A new method to calculate end-member thermodynamic properties of minerals from their constituent polyhedra i: enthalpy, entropy and molar volume. *Journal of Metamorphic Geology*, 23(3):165–179, 2005.

[85] VJ Hinsberg, SP Vriend, and JC Schumacher. A new method to calculate end-member thermodynamic properties of minerals from their constituent polyhedra ii: heat capacity, compressibility and thermal expansion. *Journal of Metamorphic Geology*, 23(8):681–693, 2005.

[86] G. Sheldrick. A short history of shelx. *Acta Crystallographica Section A*, 64(1):112–122, 2008.

[87] L. Zhang, H. Ahsbahs, S.S. Hafner, and A. Kutoglu. Single-crystal compression and crystal structure of clinopyroxene up to 10 gpa. *American Mineralogist*, 82:242–258, 1997.

[88] Robert M Hazen and Robert T Downs. *High-temperature and high-pressure crystal chemistry*, volume 41. Mineralogical Society of America Blacksburg, VA,, USA, 2000.

[89] E Huang, CH Chen, T Huang, EH Lin, and Ji-an Xu. Raman spectroscopic characteristics of mg-fe-ca pyroxenes. *American Mineralogist*, 85(3-4):473–479, 2000.

[90] MS Rutstein and WB White. Vibrational spectra of high-calcium pyroxenes and pyroxenoids. *American Mineralogist*, 56(5-6):877, 1971.

[91] G Diego Gatta, Tiziana Boffa Ballaran, and Gianluca Iezzi. High-pressure x-ray and raman study of a ferrian magnesian spodumene. *Physics and Chemistry of Minerals*, 32(2):132–139, 2005.

[92] John Kandelin and Donald J Weidner. Elastic properties of hedenbergite. *Journal of Geophysical Research: Solid Earth*, 93(B2):1063–1072, 1988.

[93] Keith Robinson, GV Gibbs, and PH Ribbe. Quadratic elongation: a quantitative measure of distortion in coordination polyhedra. *Science*, 172(3983):567–570, 1971.

[94] Zhang Li, H Ahsbahs, P-G Turk, and SS Hafner. A pressure induced phase transition in pyroxene. *High Pressure Science and Technology*, 5(1-6):732–734, 1990.

[95] Don L Anderson and Jay D Bass. Mineralogy and composition of the upper mantle. *Geophysical Research Letters*, 11(7):637–640, 1984.

[96] Jay D Bass and Don L Anderson. Composition of the upper mantle: Geophysical tests of two petrological models. *Geophysical Research Letters*, 11(3):229–232, 1984.

[97] Yoshio Fukao and Masayuki Obayashi. Subducted slabs stagnant above, penetrating through, and trapped below the 660 km discontinuity. *Journal of Geophysical Research: Solid Earth*, 118(11):5920–5938, 2013.

[98] Manuele Faccenda and Luca Dal Zilio. The role of solid–solid phase transitions in mantle convection. *Lithos*, 268:198–224, 2017.

[99] Masayuki Nishi, Tomoaki Kubo, Takumi Kato, Aiko Tominaga, Ken-ichi Funakoshi, and Yuji Higo. Exsolution kinetics of majoritic garnet from clinopyroxene in subducting oceanic crust. *Physics of the Earth and Planetary Interiors*, 189(1):47–55, 2011.

[100] Alan E Rubin. Mineralogy of meteorite groups. *Meteoritics & Planetary Science*, 32(2):231–247, 1997.

[101] Lawrence Grossman and John W Larimer. Early chemical history of the solar system. *Reviews of Geophysics*, 12(1):71–101, 1974.

[102] Aicheng Zhang, Weibiao Hsu, Rucheng Wang, and Mingwei Ding. Pyroxene polymorphs in melt veins of the heavily shocked Sixiangkou L6 chondrite. *European Journal of Mineralogy*, 18(6):719–726, 2006.

[103] Terry Plank and Charles H Langmuir. The chemical composition of subducting sediment and its consequences for the crust and mantle. *Chemical geology*, 145(3):325–394, 1998.

[104] Yusheng Zhao. Thermoelastic equation of state of monoclinic pyroxene: Camgsi2o6 diopside. *The Review of High Pressure Science and Technology*, 7:25–27, 1998.

[105] B. Li and D.R. Neuville. Elasticity of diopside to 8 gpa and 1073 k and implications for the upper mantle. *Physics of the Earth and Planetary Interiors*, 183(34):398–403, 2010.

[106] Liqin Sang and Jay D Bass. Single-crystal elasticity of diopside to 14 GPa by Brillouin scattering. *Physics of the Earth and Planetary Interiors*, 228:75–79, 2014.

[107] R.M. Thompson and R.T. Downs. The crystal structure of diopside at pressure to 10 GPa. *American Mineralogist*, 93:177–186, 2008.

[108] M. Akaogi, M. Yano, Y. Tejima, M. Iijima, and H. Kojitani. High-pressure transitions of diopside and wollastonite: phase equilibria and thermochemistry of $CaMgSi_2O_6$, $CaSiO_3$ and $CaSi_2O_5$-$CaTiSiO_5$ system. *Physics of the Earth and Planetary Interiors*, 143-144(0):145–156, 2004.

[109] Dante Canil. Stability of clinopyroxene at pressure-temperature conditions of the transition region. *Physics of the Earth and Planetary Interiors*, 86(1):25–34, 1994.

[110] Young-Ho Kim, Li Chung Ming, and Murli H Manghnani. High-pressure phase transformations in a natural crystalline diopside and a synthetic $camgsi_2o_6$ glass. *Physics of the Earth and Planetary Interiors*, 83(1):67–79, 1994.

[111] K. Oguri, N. Funamori, F. Sakai, T. Kondo, T. Uchida, and T. Yagi. High-pressure and high-temperature phase relations in diopside $CaMgSi_2O_6$. *Physics of the Earth and Planetary Interiors*, 104:363–370, 1997.

[112] T. Irifune, M. Miyashita, T. Inoue, J. Ando, K. Funakoshi, and W. Utsumi. High-pressure phase transformation in $CaMgSi_2O_6$ and implications for origin of ultra-deep diamond inclusions. *Geophysical Research Letters*, 27(21):3541–3544, 2000.

[113] Lin-Gun Liu. The system enstatite-wollastonite at high pressures and temperatures, with emphasis on diopside. *Physics of the Earth and Planetary Interiors*, 19(3):P15–P18, 1979.

[114] Yuki Asahara, Eiji Ohtani, Tadashi Kondo, Tomoaki Kubo, Nobuyoshi Miyajima, Toshiro Nagase, Kiyoshi Fujino, Takehiko Yagi, and Takumi Kikegawa. Formation of metastable cubic-perovskite in high-pressure phase transformation of ca (mg, fe, al) si_2o_6. *American Mineralogist*, 90(2-3):457–462, 2005.

[115] Yi Hu, Boris Kiefer, Craig R Bina, Dongzhou Zhang, and Przemeslaw K Dera. High-pressure γ-camgsi2o6: Does penta-coordinated silicon exist in the earth's mantle? *Geophysical Research Letters*, 44(22), 2017.

[116] A.P. Subramanian. Pyroxenes and garnets from charnockites and associated granulites. *Bulletin of the Geological Society of America*, pages 21–36, 1962.

[117] K. Momma and F. Izumi. Vesta 3 for three-dimensional visualization of crystal, volumetric and morphology data. *Journal of Applied Crystallography*, 44(6):1272–1276, 2011.

[118] F. Pedregosa, G. Varoquaux, A. Gramfort, V. Michel, B. Thirion, O. Grisel, M. Blondel, P. Prettenhofer, R. Weiss, V. Dubourg, J. Vanderplas, A. Passos, D. Cournapeau, M. Brucher, M. Perrot, and E. Duchesnay. Scikit-learn: Machine learning in Python. *Journal of Machine Learning Research*, 12:2825–2830, 2011.

[119] Georg Kresse and Jürgen Furthmüller. Efficiency of ab-initio total energy calculations for metals and semiconductors using a plane-wave basis set. *Computational Materials Science*, 6(1):15–50, 1996.

[120] Georg Kresse and Jürgen Furthmüller. Efficient iterative schemes for ab initio total-energy calculations using a plane-wave basis set. *Physical Review B*, 54(16):11169, 1996.

[121] John P Perdew and Alex Zunger. Self-interaction correction to density-functional approximations for many-electron systems. *Physical Review B*, 23(10):5048, 1981.

[122] Peter E Blöchl. Projector augmented-wave method. *Physical Review B*, 50(24):17953, 1994.

[123] Andrew M Walker, Richard P Tyer, Richard P Bruin, and Martin T Dove. The compressibility and high pressure structure of diopside from first principles simulation. *Physics and Chemistry of Minerals*, 35(7):359–366, 2008.

[124] Andrew M Walker. The effect of pressure on the elastic properties and seismic anisotropy of diopside and jadeite from atomic scale simulation. *Physics of the Earth and Planetary Interiors*, 192:81–89, 2012.

[125] Eleanor Green, Tim Holland, and Roger Powell. An order-disorder model for omphacitic pyroxenes in the system jadeite-diopside-hedenbergite-acmite, with applications to eclogitic rocks. *American Mineralogist*, 92(7):1181–1189, 2007.

[126] Gareth James, Daniela Witten, Trevor Hastie, and Robert Tibshirani. *An introduction to statistical learning*, volume 112. Springer, 2013.

[127] Jibamitra Ganguly, Andrew M Freed, and Surendra K Saxena. Density profiles of oceanic slabs and surrounding mantle: Integrated thermodynamic and thermal modeling, and implications for the fate of slabs at the 660 km discontinuity. *Physics of the Earth and Planetary Interiors*, 172(3):257–267, 2009.

[128] F. Liebau. Pentacoordinate silicon intermediate states during silicate condensation and decondensation. crystallographic support. *Inorganica Chimica Acta*, 89(1):1–7, 1984.

[129] F. Yuan and L. Huang. Brittle to ductile transition in densified silica glass. *Scientific Reports*, 4, 2014.

[130] Anna Pakhomova, Elena Bykova, Maxim Bykov, Konstantin Glazyrin, Biliana Gasharova, H-P Liermann, Mohamed Mezouar, Liudmila Gorelova, S Krivovichev, and L Dubrovinsky. A closer look into close packing: Pentacoordinated silicon in a high-pressure polymorph of danburite. *IUCrJ*, 4(5), 2017.

[131] Q.Y. Hu, J.F. Shu, A. Cadien, Y. Meng, W.G. Yang, H.W. Sheng, and H.K. Mao. Polymorphic phase transition mechanism of compressed coesite. *Nature Communication*, 6, 2015.

[132] S. L. Chaplot and N. Choudhury. Molecular dynamics simulations of seismic discontinuities and phase transitions of $MgSiO_3$ from 4 to 6-coordinated silicate via a novel 5-coordinated phase. *American Mineralogist*, 86(5-6):752–761, 2001.

[133] Alfred Edward Ringwood. Phase transformations and differentiation in subducted lithosphere: implications for mantle dynamics, basalt petrogenesis, and crustal evolution. *The Journal of Geology*, pages 611–643, 1982.

[134] Masayuki Nishi, Tomoaki Kubo, and Takumi Kato. Metastable transformations of eclogite to garnetite in subducting oceanic crust. *Journal of mineralogical and petrological sciences*, 104(3):192–198, 2009.

[135] R. Agrusta, J. van Hunen, and S. Goes. The effect of metastable pyroxene on the slab dynamics. *Geophysical Research Letters*, 41(24):8800–8808, 2014.

[136] A. Chopelas and G. Serghiou. Spectroscopic evidence for pressure-induced phase transitions in diopside. *Physics and Chemistry of Minerals*, 29(403-408), 2002.

[137] Anna Pakhomova, Leyla Ismailova, Elena Bykova, Maxim Bykov, Tiziana Boffa Ballaran, and Leonid Dubrovinsky. A new high-pressure phase transition in clinoferrosilite: In situ single-crystal X-ray diffraction study. *American Mineralogist*, 102(3):666–673, 2017.

[138] Dongzhou Zhang, Yi Hu, and Przemyslaw K Dera. Compressional behavior of omphacite to 47 GPa. *Physics and Chemistry of Minerals*, 43(10):707–715, 2016.

[139] Jingui Xu, Dongzhou Zhang, Dawei Fan, Robert T Downs, Yi Hu, and Przemyslaw K Dera. Isosymmetric pressure-induced bonding increase changes compression behavior of clinopyroxenes across jadeite-aegirine solid solution in subduction zones. *Journal of Geophysical Research: Solid Earth*, 122(1):142–157, 2017.

[140] N Morimoto. Nomenclature of pyroxenes. *Mineralogy and Petrology*, 39(1):55–76, 1988.

[141] NAW Holzwarth, GE Matthews, RB Dunning, AR Tackett, and Y Zeng. Comparison of the projector augmented-wave, pseudopotential, and linearized augmented-plane-wave formalisms for density-functional calculations of solids. *Physical Review B*, 55(4):2005, 1997.

[142] Bob Svendsen and Thomas J Ahrens. Dynamic compression of diopside and salite to 200 GPa. *Geophysical Research Letters*, 10(7):501–504, 1983.

[143] A Hogrefe, DC Rubie, TG Sharp, and F Seifert. Metastability of enstatite in deep subducting lithosphere. *Nature*, 372(6504):351–353, 1994.

[144] Stanislav N Tandura, Mikhail G Voronkov, and Nikolai V Alekseev. Molecular and electronic structure of penta-and hexacoordinate silicon compounds. In *Structural Chemistry of Boron and Silicon*, pages 99–189. Springer, 1986.

[145] Robert R Holmes. Comparison of phosphorus and silicon: Hypervalency, stereochemistry, and reactivity. *Chemical Reviews*, 96(3):927–950, 1996.

[146] Golam Rasul, GK Surya Prakash, and George A Olah. Comparative study of the hypercoordinate carbonium ions and their boron analogs: A challenge for spectroscopists. *Chemical Physics Letters*, 517(1):1–8, 2011.

[147] Edmund T White, Jian Tang, and Takeshi Oka. Ch^{5+}: The infrared spectrum observed. *Science*, 284(5411):135–137, 1999.

[148] J. Zhang, Harry W Green, and Krassimir N Bozhilov. Rheology of omphacite at high temperature and pressure and significance of its lattice preferred orientations. *Earth and Planetary Science Letters*, 246(3):432–443, 2006.

[149] Stephen H Kirby, Seth Stein, Emile A Okal, and David C Rubie. Metastable mantle phase transformations and deep earthquakes in subducting oceanic lithosphere. *Reviews of Geophysics*, 34(2):261–306, 1996.

[150] David C Rubie and Charles R Ross. Kinetics of the olivine-spinel transformation in subducting lithosphere: Experimental constraints and implications for deep slab processes. *Physics of the Earth and Planetary Interiors*, 86(1-3):223–243, 1994.

[151] Frederic C Marton, Craig R Bina, Seth Stein, and David C Rubie. Effects of slab mineralogy on subduction rates. *Geophysical Research Letters*, 26(1):119–122, 1999.

[152] Craig R Bina and Hitoshi Kawakatsu. Buoyancy, bending, and seismic visibility in deep slab stagnation. *Physics of the Earth and Planetary Interiors*, 183(1):330–340, 2010.

[153] Harro Schmeling, Ralf Monz, and David C Rubie. The influence of olivine metastability on the dynamics of subduction. *Earth and Planetary Science Letters*, 165(1):55–66, 1999.

[154] M Tetzlaff and H Schmeling. The influence of olivine metastability on deep subduction of oceanic lithosphere. *Physics of the Earth and Planetary Interiors*, 120(1):29–38, 2000.

[155] Tian Qin, Fei Wu, Zhongqing Wu, and Fang Huang. First-principles calculations of equilibrium fractionation of o and si isotopes in quartz, albite, anorthite, and zircon. *Contributions to Mineralogy and Petrology*, 171(11):91, 2016.

[156] Bob Svendsen and Thomas J Ahrens. Shock-induced temperatures of $CaMgSi_2O_6$. *Journal of Geophysical Research: Solid Earth*, 95(B5):6943–6953, 1990.

[157] WangPing Chen and Michael R Brudzinski. Seismic anisotropy in the mantle transition zone beneath Fiji-Tonga. *Geophysical Research Letters*, 30(13), 2003.

[158] Václav Vavryčuk. Spatially dependent seismic anisotropy in the Tonga subduction zone: A possible contributor to the complexity of deep earthquakes. *Physics of the Earth and Planetary Interiors*, 155(1):63–72, 2006.

[159] Chang Lu, Zhu Mao, Jung-Fu Lin, Kirill K Zhuravlev, Sergey N Tkachev, and Vitali B Prakapenka. Elasticity of single-crystal iron-bearing pyrope up to 20 gpa and 750 k. *Earth and Planetary Science Letters*, 361:134–142, 2013.

[160] Zhixue Du, Lowell Miyagi, George Amulele, and Kanani KM Lee. Efficient graphite ring heater suitable for diamond-anvil cells to 1300 k. *Review of Scientific Instruments*, 84(2):024502, 2013.

[161] Li Li and Donald J Weidner. Effect of phase transitions on compressional-wave velocities in the earths mantle. *Nature*, 454(7207):984, 2008.

[162] Jianzhong Zhang, Baosheng Li, Wataru Utsumi, and Robert C Liebermann. In situ x-ray observations of the coesite-stishovite transition: reversed phase boundary and kinetics. *Physics and Chemistry of Minerals*, 23(1):1–10, 1996.

[163] Guang-Rui Qian, Xiao Dong, Xiang-Feng Zhou, Yongjun Tian, Artem R Oganov, and Hui-Tian Wang. Variable cell nudged elastic band method for studying solid–solid structural phase transitions. *Computer Physics Communications*, 184(9):2111–2118, 2013.

[164] Vladan Stevanović, Ryan Trottier, Charles Musgrave, Félix Therrien, Aaron Holder, and Peter Graf. Predicting kinetics of polymorphic transformations from structure mapping and coordination analysis. *Phys. Rev. Materials*, 2:033802, Mar 2018.